Slip behaviour of faults in a subduction zone setting and their response to surface processes

- insights from finite-element modelling

Von der Naturwissenschaftlichen Fakultät

der Gottfried Wilhelm Leibniz Universität Hannover

zur Erlangung des Grades

DOKTOR DER NATURWISSENSCHAFTEN

Dr. rer. nat.

genehmigte Dissertation

von

Tao Li

geboren am 28.10.1983 in Guangdong, V.R. China

2013

Referentin: Prof. Dr. Andrea Hampel

Korreferentin: Prof. Dr. Jutta Winsemann

Tag der Promotion: 05.11.2013

Table of Contents

KURZZUSAMMENFASSUNG

An Subduktionszonen treten weltweit die größten Erdbeben auf, doch unser Verständnis über die Verformung der Oberplatte sowie den Einfluss von Oberflächenprozessen, die Heterogenitäten in der Geometrie der seismogenen Zone und der Reibung entlang des Plattenkontakts ist noch begrenzt. Diese Arbeit ermittelt mit Hilfe von zwei- und dreidimensionalen (2-D und 3-D) Finite-Elemente-Modellen die Auswirkungen von a) klimabedingten Änderungen in der Auflast (Meeresspiegelschwankungen, Erosion und Sedimentation) sowie b) Variationen in den physikalischen Eigenschaften des Plattenkontakts auf den seismischen Zyklus in Subduktionszonen. Im ersten Teil der Arbeit wird der Effekt von klimabedingten Änderungen auf Subduktionszonen untersucht. Die Modellergebnisse zeigen, dass ein Abfall des Meeresspiegels von 120 m in 100,000 Jahren eine Hebung von bis 0,7 m hervorruft, während ein nachfolgender Meeresspiegelanstieg von 120 m Absenkungen gleichen Betrags innerhalb 20,000 Jahren verursacht. Sowohl Hebungen als auch Absenkungen sind vor allem im submarinen Forearc-Bereich zu finden. Horizontale Verschiebungen bis zu 0,11 m sind beim Meeresspiegelabfall seewärts und beim Meeresspiegelanstieg landwärts gerichtet. Die berechneten Veränderungen der Coulomb-Spannungen entlang des Plattenkontakts betragen etwa 0,2 - 0,5 MPa. Diese Größenordnung der Spannungsänderungen impliziert, dass Erdbeben beim Meeresspiegelabfall gefördert und beim Meeresspiegelanstieg verzögert werden können. Die Wirkung der eustatischen Meeresspiegelschwankungen kann durch glazial-interglaziale Variationen in Erosions- und Sedimentationsraten im marinen Forearc-Bereich noch verstärkt werden, wie sedimentologische Daten vom chilenischen Plattenrand zeigen. Der zweite Teil der Arbeit umfasst Modelle, die den Effekt des Reibungskoeffizienten sowie der Geometrie der seismogenen Zone auf die Verformung der Oberplatte und ihren Spannungszustand untersuchen. Die Ergebnisse der 2-D und 3-D-Modelle zeigen, dass das berechnete Muster von vertikalen und horizontalen Verschiebungen mit den geodätisch beobachteten Mustern übereinstimmen. Eine umfassende Parameterstudie zeigt, dass die Größe der vertikalen Versätze stark vom Reibungskoeffizient der seismogenen Zone und der Übergangszone beeinflusst wird. Die landwärtige Erweiterung der Bereiche mit stärkster interseismischer Hebung sowie die koseismische Senkung in den Küstenregionen werden durch die Grenze der seismogenen Zone gesteuert. Die laterale Verbreitung der Bruchzone in den 3-D-Modellen beeinflusst die koseismische Oberflächenbewegung sowohl in ihrer Magnitude als auch in der Bewegungsrichtung. Zusätzliche Modellierungen wurden durchgeführt, um die Erdbeben-Sequenzen des 2010 Maule (Chile) Erdbebens und des 2011 Tohoku-Oki (Japan) Erdbebens zu untersuchen. Diese Modelle belegen eine Abhängigkeit zwischen der Magnitude der Beben und der Geschichte des Spannungsaufbaus in der seismogenen Zone. Insgesamt trägt diese Arbeit zu einem besseren Verständnis über die Auswirkungen von klimabedingten Faktoren auf den seismischen Zyklus an Subduktionzonen bei. Außerdem bietet die Arbeit einen Einblick in die Faktoren, die den Spannungszustand an der Plattengrenze sowie die Verformung der Oberplatte kontrollieren.

Schlagwörte: Subduktionszonen, Oberflächenprozessen, Finite-Elemente-Modellen

Abstract

Large interplate earthquakes have repeatedly occurred in the major subduction zones worldwide. However, our understanding of upper plate deformation as well as earthquake generation still needs to be improved with respect to the influence of surface processes and heterogeneities in the geometry and friction along the plate interface. This thesis evaluates the impact of climate-driven load changes and variations in the physical properties of the plate interface on the seismic cycle at subduction zones using by two- and three-dimensional (2-D and 3-D) finite element subduction zone models. Model results show that a sea-level fall by 120 m over 100 ka causes up to 0.72 m of uplift, whereas subsidence is induced by a subsequent sea-level rise by 120 m over 20 ka. Both uplift and subsidence are found most pronounced in the submarine part of the forearc. Horizontal displacements up to 0.11 m are directed seaward during sea-level fall and landward during sea-level rise. The resulting Coulomb stress changes on the plate interface are about 0.2-0.5 MPa and indicate that earthquakes are promoted during sea-level fall and delayed during sea-level rise. Additional to eustatic sea-level changes, the effect of glacial-interglacial transport and offshore deposition of sediment on the displacement and stress field of the forearc are also investigated. Based on the seismic and sedimentological data from the Chilean margin, erosion and deposition rates of 1 m/ka during the sea-level fall and rates of 0.1 m/ka during subsequent sea-level rise are implemented in the models. Owing to the strong glacial sediment erosion at the continental shelf and the resulting high sedimentation rates in the trench, forearc uplift is enhanced by ~0.3 m at the continental shelf and seismic slip is promoted at the plate interface beneath. In contrast, uplift is reduced at the toe of the forearc and the seismic slip of the plate interface between trench and continental shelf can be delayed. The second part of the thesis is dedicated to models that investigate the impacts of friction coefficient and the geometry of the seismogenic zone along the plate interface on upper-plate deformation and state of stress on the megathrust. The 2-D and 3-D model results show patterns of vertical and horizontal displacements that are in general agreement with geodetically observed patterns. Sensitivity analyses reveal that the magnitude of the vertical displacement is strongly influenced by the friction coefficients of the seismogenic zone and the transition zone. The landward extension of the areas with maximum interseismic uplift and coseismic subsidence in the coastal regions is controlled by the downdip limit of the seismogenic zone. The lateral extent of the rupture zone in the 3-D models affects the coseismic surface displacements both in magnitude and sense of movement. Additional modelling with two types of earthquake sequences occurring before the main shock were constructed to investigate the earthquake sequences of the 2010 Maule (Chile) and 2011 Tohoku-Oki (Japan) earthquakes, respectively. These models show that the magnitude of subduction earthquakes that occurred in repeatedly ruptured areas depends on the history of stress accumulation and release from previous earthquakes. Overall, this thesis contributes to a better understanding on the impacts of climate-driven load changes on deformation of subduction forearc and their potential role on seismic cycles of subduction megathrusts. Also, it provides an insight on influencing factors that may control the states of stress accumulation and release in the upper plate, which are closely related to the magnitude of the subduction earthquakes.

Keywords: subduction zones, surface processes, finite-element models

1. Introduction

1.1 Motivation

The largest earthquakes on Earth occur at subduction zones (Fig. 1.1). Such earthquakes are associated with the release of stress accumulated over tens to hundreds of years in the seismogenic zone of the interface between the subducting plate and the upper plate (Kanamori, 1986). The resulting coseismic slips at megathrusts can cause huge destruction, as evident from the devastating subduction zone earthquakes in Alaska ($M_w = 9.2$ 1964), in Sumatra ($M_w = 9.2$ 2004), in Chile ($M_w = 8.8$ Maule 2010) and in Japan ($M_w = 9$ Tohoku-Oki 2011). Against this background, understanding of the earthquake cycle, the associated deformation of the upper plate and the impact of surface processes on the stress state of the seismogenic zone is of crucial importance.
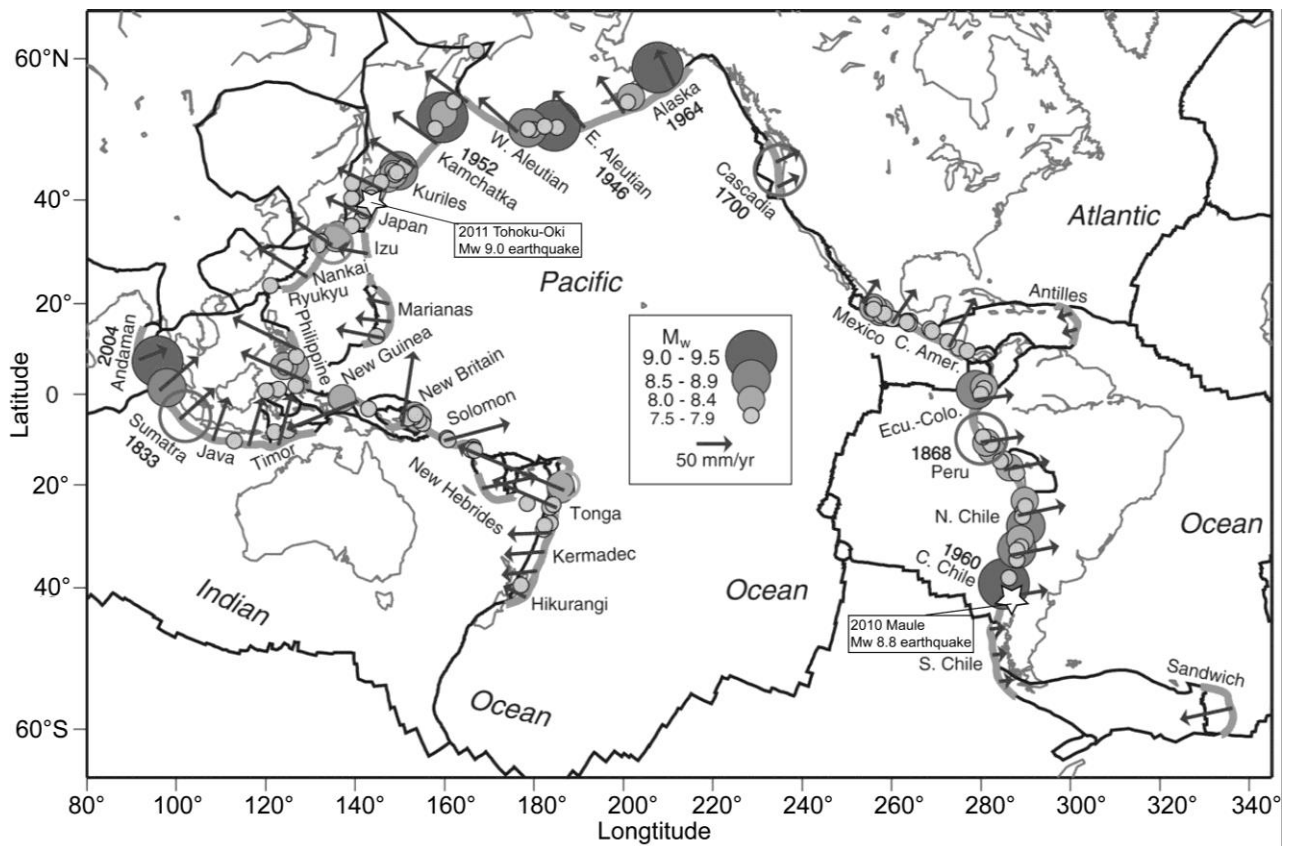
Figure 1.1 Worldwide distributions of large earthquakes (modified on McCaffrey, 2008). The world's major subduction zones and tectonic plate boundaries are indicated by grey thick lines and black lines, respectively. Filled circles show locations of known earthquakes of $M_w \geq 7.5$ or greater since 1900 till 2008 (circle radius and gray scaled by magnitude). Open circles are largest known earthquakes from A.D. 1700 to 1900. Arrows show horizontal velocity of subducting plate relative to overriding plate. Dates are given for all $M_w = 9$ earthquakes (till 2008). The 2010 Maule (Chile) and 2011 Tohoku-Oki (Japan) earthquakes are additionally indicated by white stars and the magnitudes are also given.

Previous studies have shown that tides and glacier fluctuations on timescales of $1-10^3$ a may modulate the seismicity at subduction zones by altering the stress field in the upper plate and

along the plate interface (Nasu et al., 1931; Shlien, 1972; Tsuruoka et al., 1995; Kasahara, 2002; Cochran et al., 2004). For example, in Alaska, space-geodetic measurements combined with numerical modelling revealed that glacier ice mass fluctuations induce significant vertical displacements and stress changes that may modulate the background seismicity of the subduction zone (Cohen, 1993; Sauber et al., 2000; Sauber and Ruppert, 2008). Similarly, stress perturbations from ocean loading were inferred to be capable of changing the stress states of transform faults at plate boundaries (Luttrell and Sandwell, 2010). Other mechanism of varying loading of the crust is the on- and offshore transport and deposition of large amounts of sediment during and after glacial periods (e.g. Church and Slaymaker, 1989). For example, at the Cascadia and Chilean convergent margins, variable sediment input was inferred to have affected the deformation of accretionary prisms (Bourgois et al., 2000; Adam et al., 2004; Contreras-Reyes et al., 2010).

Previous numerical models mainly focussed on the subduction processes on a 10^6-year timescale at convergent margins (e.g. Beaumont et al., 1994; Hyndman and Wang, 1995; Buiter et al., 2011; Gerya and Stöckhert 2005; Hampel and Pfiffner, 2006; Cailleau and Oncken, 2008; Gerya, 2011; Gerya and Melnick, 2011). Based on a 2-D coupled petrological-thermomechanical numerical model, Gerya and Meilick (2011) demonstrated that strong coupling at the plate boundaries can lead to increased compression and subduction erosion of the continental crust, which results in strong crustal shortening of the continental plate (Fig. 1.2). They also suggested that this geodynamic regime can be applicable to the evolution of the subduction zone in the region of the south-central Andes. Other modelling studies focusing on co- and postseismic deformation of an individual earthquake (e.g. Thatcher and Rundle, 1984b; Thatcher and Rundle, 1984; Dragert et al., 1994; Masterlark et al. 2001; Hu et al., 2004; Kato and Yoshida, 2011; Hu and Wang, 2012) have also revealed the links between crustal deformations and the mechanisms of subduction earthquakes, which reflect the cyclic build-up and release of tectonic stress in the seismogenic regions. Despite the aforementioned studies, increasing efforts have been deployed on investigating the deformation as well as the seismicity of the subduction zones on more specified resolutions, such as impacts from climate induced variations in ice and water volumes (e.g. Cohen, 1993; Sauber and Molnia, 2004; Sauber and Ruppert, 2008; Luttrell and Sandwell, 2010) and the mass redistribution associated with erosion and sediment deposition (e.g. Blumberg et al., 2008; Contardo et al., 2013). For example, Blumberg et al. (2008) observed that the increase in turbidite recurrence time may indicate the delay of earthquakes on the plate interface, which can be associated with the postglacial sea-level rise and decrease of sediment availability. However, for establishing the links between climate-induced surface load changes and state of stress along the plate interface of a subduction zone, investigations need to be further performed on smaller timescales, e.g. glacial-interglacial cycles of 10^4-10^5 years, so that the influences of climate-induced load changes can be distinguished from long-term tectonic loading (e.g. Shennan, 2009). For this purpose, more sophisticated numerical models also need to be developed, in which tectonic features of subduction zones as well as climate-induced load changes can be simulated together.

Application of Global Positioning System (GPS) since the early 1990s has enabled more detailed and larger-scale investigations on crustal deformation in subduction zones. Dense networks of GPS stations, e.g. in Japan and along the Chilean margin, provide information on relative motions

among different regions, as well as continuous monitoring of co-, post- and interseismic deformation at many subduction zones (Wang et al., 2012). The geodetic data do not only provide better insight into the deformation of subduction zones but also deliver systematic constraints for modelling studies. At the same time, rapid developments of numerical modelling technique have further enabled multi-discipline geoscientific investigations that strongly reinforced the conventional geodetic methods (e.g. tide gauges, levelling and GPS). Simplified models, e.g. elastic dislocation models, have been developed and broadly applied in the 1980s-90s for explaining the geodetically observed inter- and coseismic displacements at subduction zones (e.g. Savage, 1983; Thatcher, 1984b; Dragert et al., 1994; Hyndman and Wang, 1995). Nevertheless, due to the limitations on computation capacities, earlier subduction zone models had to make compromises by applying certain simplifications on the subduction zone geometry and on the material properties, such as applying pure elastic homogenous half-space model. Concerning the complexity of the subduction zones, the application of finite-element models represents a major step forward owing to their capability of implementing complex boundary conditions, structural heterogeneities, viscoelastic rheologies and variations in material properties (Cohen, 1999; Masterlark et al., 2001; Masterlark, 2003; Gerya, 2011; Wang et al., 2012; Trubienko et al., 2013).
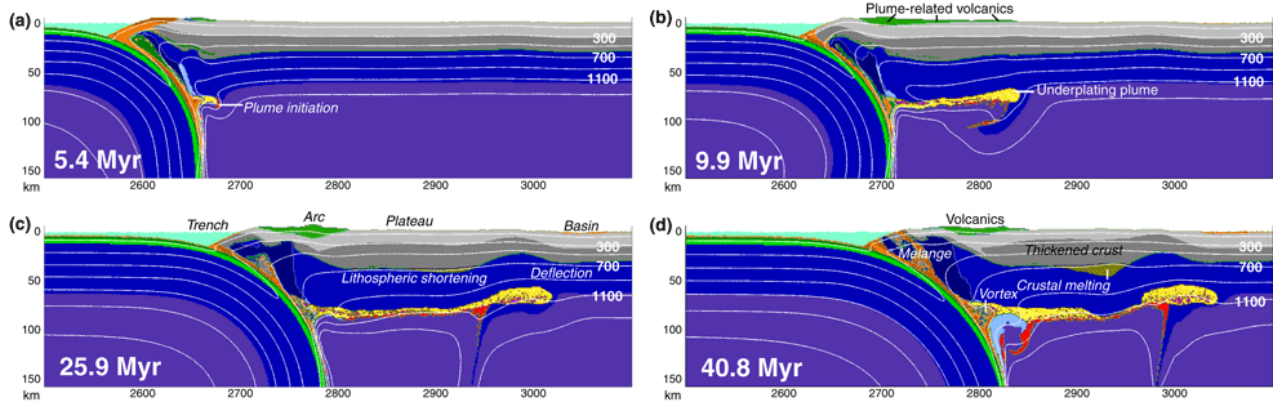

Figure 1.2 (a)–(d) Representative stages of model evolution with time (from Gerya and Melnick, 2011). Note time is given from the beginning of convergence. A velocity field of 50 mm/a is internally prescribed inside the subducting plate for convergence. Plate interface frictions are facilitated by prescribing a rheologically weak shear zone at the border of the two plates (see model configurations in Gerya and Melnick, 2011). The subducted sedimentary plume is initiated in stage a). The head of the plume follows the position of migrating lithospheric flexure formed by crustal shortening. At the initial stage (b), volcanic crust growth spreads landwards following the underplating plume. At the later stage (c)–(d), this activity focuses near the trench. Crustal thickening leads to the heating and melting of the lower crust. This scenario is considered to be applicable for explaining the evolution of the south-central Chilean subduction zone (see text for details).

With respect to our understanding of subduction seismicity, it has been generally recognized that convergence rate exerts a first-order control on subduction zone evolution. Stresses are accumulated in the upper plate by accommodating the convergence of the subducting plate, and are subsequently released throughout earthquake cycles. Previous modelling studies have also revealed parameters that may be decisive for the mechanisms of subduction earthquakes. They can be summarized to the following three categories: 1) material properties in upper plate (e.g. Masterlark et al., 2001; Hu and Wang, 2012; Wang et al., 2012; Trubienko et al., 2013); 2) properties of plate interface with respect to mechanical frictional properties, thermal regimes and

width of seismogenic zone (e.g. Hyndman and Wang, 1995; Cailleau and Oncken, 2008; Kato and Yoshida, 2011;); 3) lateral variations in the interseismic coupling rate (e.g. Hu et al., 2004; Trubienko et al., 2013). So far, studies focusing on the long-term deformations at the convergent margins, i.e. on timescales of 10^5-10^6, are relative abundant (Buiter et al., 2010; Gerya, 2011 and references therein). In comparison, only few modelling studies investigated forearc deformation over one and more earthquake cycles as well as their implications on seismic risks (e.g. Masterlark et al., 2001; Kato and Yoshida, 2011; Hu and Wang, 2012; Trubienko et al., 2013). Therefore, further modelling work is necessary to evaluate and quantify the influence of the parameters mentioned above on the behaviour of megathrust during one or more seismic cycles.

Moreover, deficits still exist on understanding the specific generating patterns that are characterized by different tectonic settings and distinct geological features. The recent M_w 8.8 Maule (Chile) 2010 and M_w 9.0 Tohoku-Oki (Japan) earthquakes have provided opportunities for investigating the generation of large megathrust earthquakes. The remarkably advancing measuring and modelling techniques, and the well-documented displacements caused by these great earthquakes, can contribute to a much better understanding of the mechanisms of earthquake cycles in subduction zones. This encourages further explorations of applying numerical models for this field.

1.2 Objectives of this thesis

Using finite-element modelling, this doctoral thesis is dedicated to improving our knowledge on factors that control the slip behaviour of the plate interface in a subduction zone setting and their response to surface processes. In this context, two main questions are addressed:

1) How do sea-level changes affect the stress state of the plate interface as well as the earthquake cycle of the subduction zone? (Chapter 2.1)

2) To what extent can glacial-interglacial changes in sedimentation flux to the continental margin modulate the stress and displacement fields of the forearc? (Chapter 2.2)

The other objective of this thesis (Chapter 3) is to investigate key parameters controlling the deformation during the seismic cycle of the megathrust. For this purpose, systematic variations in the frictional properties along plate interface and the downdip limit of the seismogenic zone are examined by using both 2-D and 3-D models. In addition, the 3-D models provide insights into the effect of lateral variations of the parameters on the displacement patterns. Finally, heterogeneous spatiotemporal distributions of foreshock earthquake sequences, which are identified as one of the characteristic features of the Tohoku-Oki 2011 earthquake, are considered in additional 3-D models (Chapter 3.4). The thesis closes with a general discussion about the model results and their implications for our understanding of subduction zone earthquakes (Chapter 4) and a section with conclusions and outlook (Chapter 5).

2. Effect of surface processes on the forearc and plate interface in subduction zones

2.1 Effect of glacial-interglacial sea-level changes on the displacement and stress field in the forearc and along the plate interface of subduction zones (modified from Li and Hampel (2012))

2.1.1 Introduction

Active faulting in subduction zones poses a serious seismic threat to the often densely populated coastal regions. As a consequence, much effort has been put into monitoring the seismicity beneath the forearc and the identification of parameters that may modulate the frequency and magnitude of earthquakes on different timescales. One of the first parameters that were recognized to affect the seismicity in subduction zones was the ocean tides. The hypothesis of ocean tides as a trigger of earthquakes was already put forward by Nasu et al. (1931) after an earthquake that hit central Japan in 1930. Since then, a positive correlation between ocean tides and earthquake occurrence has been documented by many studies (e.g. Shlien, 1972; Tsuruoka et al., 1995; Kasahara, 2002; Cochran et al., 2004). After statistically analysing 988 globally distributed high-magnitude seismic events, Tsuruoka et al. (1995) concluded that of all fault types normal faults are most susceptible to tidally triggered earthquakes because the periodic ocean loading affects the vertically oriented maximum principal stress. Based on the analysis of earthquake data from 1977-2000, Cochran et al. (2004) later showed that strong ocean tides can also trigger shallow thrust earthquakes, with the rate of earthquakes differing from the background rate by a factor of 3 with the tidal stress. They concluded that the tidal stress changes have more effect on thrust and normal faults than on strike-slip faults because the latter are oriented mostly subvertical and hence less susceptible to the variable ocean loading.

On the timescale of decades, the seismicity in subduction zones is influenced by fluctuations in the mass of glaciers situated in the upper plate (e.g. Cohen, 1993; Sauber et al., 2000; Ivins and James, 2004). A combination of glaciological and seismological records, modern space-geodetic measurements and numerical modelling revealed that glacier mass fluctuations over the last 10-100 years in south-central Alaska induced considerable vertical displacements and stress changes that have modulated the background seismicity of the subduction zone (Cohen, 1993; Sauber et al., 2000; Sauber and Molina, 2004). For example, in the eastern Chugach Mountains, southern Alaska, a large-scale redistribution of glacier ice between 1993 and 1995 was associated with a significant increase in the number and size of earthquakes (Sauber et al., 2000). This finding was later confirmed by a comprehensive compilation of seismological and glaciological data for southern Alaska, which showed that rapid ice fluctuations promoted small earthquakes on thrust faults (Sauber and Ruppert, 2008).

On the timescale of 10-100 ka, eustatic sea-level changes may affect the stress state of the crust at the borders of ocean basins. During the last glacial-interglacial cycle that culminated in the Last Glacial Maximum (LGM) ~20 ka ago, the sea-level fall and subsequent rise was ~125 m (Imbrie

et al., 1984; Zachos et al., 2001; Peltier and Fairbanks, 2006). Using a semi-analytical approach with an elastic plate overlying a viscoelastic half-space, Luttrell and Sandwell (2010) showed that the post-LGM sea-level rise and the resulting flexural loading caused considerable stress perturbations in coastal regions worldwide. To estimate the effect of these stress perturbations on major plate boundary faults, which were not included in their model, they calculated the resolved shear and normal stresses for selected faults of known orientation. The results show that the post-LGM sea-level rise should have caused an increase in the Coulomb stress by up to 1.5 MPa on the vertically oriented San Andreas, Alpine and North Anatolian faults (Luttrell and Smith, 2010). For the Cascadia subduction zone, which they approximated by a 15°-dipping plane, they calculated a change in the Coulomb stress of ~0.4 MPa, using a friction coefficient of 0.4.

The results of the previous studies summarized above provide strong evidence that faults in the upper part of a subduction zone - including the seismogenic part of the plate interface - are susceptible to changes in ice and water loads on different timescales. So far, however, the effect of eustatic sea-level changes on uplift and subsidence of the forearc as well as on the stress along the plate interface remains unresolved. In this study, we use a two-dimensional numerical model with a subduction-zone geometry to quantify how the forearc and the plate interface respond to the sea-level fall and rise during a glacial-interglacial period. In the following, we describe the model setup and present the results with a focus on the induced changes in the displacement and stress fields in the upper part of the subduction zone including the seismogenic part of the plate interface. Finally, we discuss implications for the seismic cycle of subduction thrusts.

2.1.2 Model setup

To quantify the effect of sea-level changes on a subduction zone, we use a two-dimensional finite-element model created with the commercial software Abaqus (version 6.11). The model consists of a 1500-km-long oceanic plate, which is subdivided into an 8-km-thick crust and a 72-km-thick lithospheric mantle, and a 1000-km-long continental plate consisting of a 15-km-thick upper crust, a 15-km-thick lower crust and a 70-km-thick lithospheric mantle. Our model does not include the sub-lithospheric mantle, i.e. we assume that glacial-interglacial sea-level changes do not induce significant viscous flow in the sub-lithospheric mantle. The model domain is meshed using triangular plane-strain elements with a maximum edge length of 1 km. The rheological parameters of the model are given in Fig. 2.1. To obtain the geometry of a subduction zone as depicted in Figure 1a, we perform the following steps: First, the initially horizontal oceanic plate is downflexed to take into account the bending stresses in the subducting plate (cf. Buiter et al., 2001; Hampel and Pfiffner, 2006). This model step is carried out using a viscosity of 1×10^{23} Pa s for the lithospheric mantle. Afterwards, the continental plate is added to the model domain with the contact between the two plates representing the plate interface. In the same model step, a water body and a pressure (Fig. 2.1a), which together represent an ocean with an average water depth of 5000 m, are added on top of the oceanic plate and the continental margin. At the trench, the water depth increases to 6580 m. In the third model step, isostatic equilibrium is established. This model step as well as the following steps is computed as a static analysis, i.e. viscous deformation is not considered. As the displacements and stress changes resulting from the sea-level variations occur in the uppermost part of the model and are small compared to the thickness

of the plates, the two vertical model sides and the bottom are fixed in the vertical and horizontal directions to facilitate the calculation of the model.

During the final model step, the falling and subsequently rising sea level during a glacial-interglacial cycle is simulated by changing the pressure applied on top of the water body. Based on the global sea-level curve derived from the oxygen-isotope record (Imbrie et al., 1984; Chappell and Shackleton, 1986; Zachos et al., 2001; Peltier and Fairbanks, 2006), we assume a sea-level fall by 125 m over 100 ka and a subsequent sea-level rise by the same amount over 20 ka (Fig. 2.1b). During these sea-level changes the plate interface is kept locked, i.e. no relative displacement occurs between the two plates. For comparison, we also calculated a reference model run, in which no sea-level changes occur.
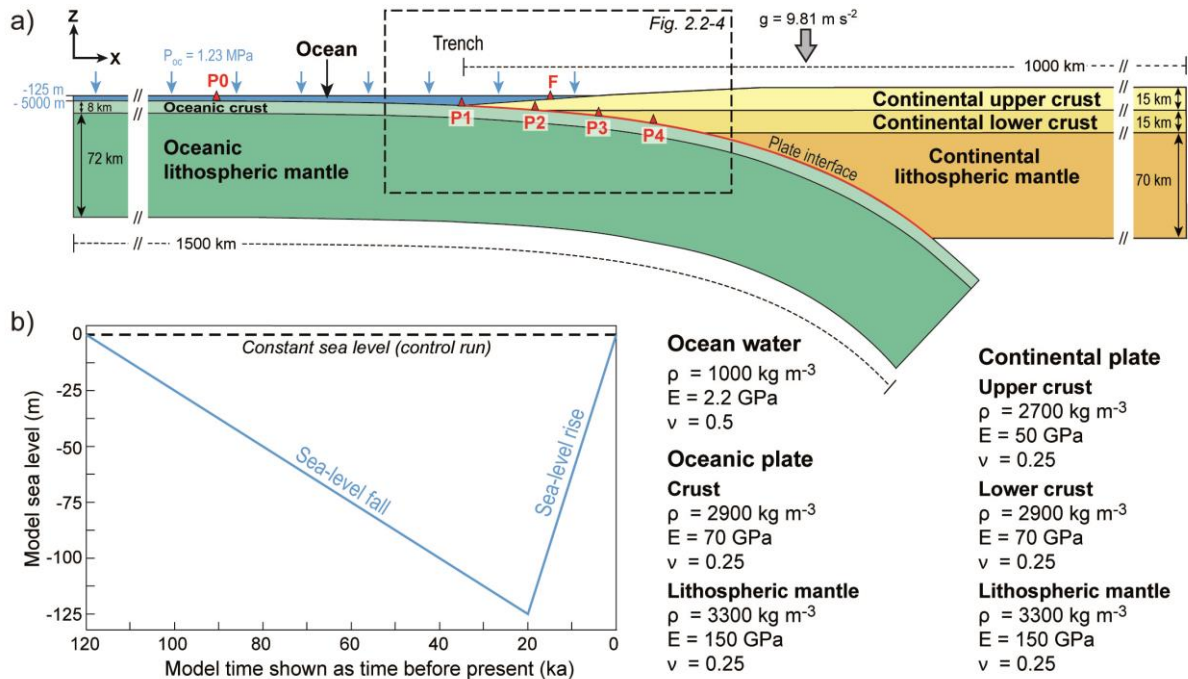

Figure 2.1 a) Setup of the finite-element model with an oceanic and a continental plate that are in contact along a locked plate interface (solid red line). Rheological parameters are ρ density, E Young's modulus, and υ Poisson's ratio. Gravity is included as a body force (*g* acceleration of gravity). An ocean on top of the oceanic plate and the continental margin with a average water depth of 5000 m is implemented as a combination of a water body (average water depth: 4875 m) and a pressure P_{oc} equivalent to 125 m of water (blue arrows). This pressure is decreased and subsequently increased to simulate the falling and subsequently rising sea level during a glacial-interglacial cycle, respectively (see Fig. 2.1b for the temporal evolution of the pressure). At the beginning of the model run, isostatic equilibrium is established by a lithostatic pressure and elastic foundation at the bottom of the model. Afterwards, the model sides and bottom are fixed in the horizontal and vertical directions (see text for details). Red triangles mark the locations of points F and P0-P4, at which displacements and stresses were extracted from the model (Figs. 2.2-4, 2.6). Box with dashed outline marks the part of the model for which the displacement and vertical stress fields are shown in Figs. 2.1-4. b) Temporal evolution of the sea level in the model, reflecting a fall and subsequent rise by 125 m over 120 ka (cf. Imbrie et al., 1984; Peltier and Fairbanks, 2006). For comparison, a control run was performed with a constant sea level (dashed line).

2.1.3 Model results

To analyse the effect of the sea-level fall and rise on the upper part of the subduction zone, we extracted the changes in the vertical and horizontal displacement as well as in the stress field from

the model. In addition to cross-sections of the model, the evolution of these parameters through time will also be shown at six selected points, with point F being located in the submarine part of the forearc, four points (P1-P4) located on the plate interface and one point positioned 360 km seaward of the trench (P0) (see Fig. 2.1a). Note that the model time is shown as time before present in all subsequent figures.

Vertical displacement

Figure 2.2 Vertical displacement induced by a) a falling sea level (120-20 ka) and b) a rising sea level (20-0 ka). c) Temporal evolution of the vertical displacements at point F in the forearc and at points P0-P4 located on the plate interface (Figs. 2.1a, 2.2a). For reference, the result from the control run (constant sea level) is shown for point P1.

During the sea-level fall between 120 ka and 20 ka, the upper part of the subduction zone rises by up to 0.7 m (Fig. 2.2a), with the uplift maximum occurring in the forearc region at point F. The displacement induced by the sea-level fall decreases both with depth and landward where it diminishes to zero ~20 km landward of the coast. During the subsequent sea-level rise between 20 ka and 0 ka, the forearc and the oceanic plate subside by up to 0.7 m owing to the increase in

14

the water load (Fig. 2.2b). The temporal evolution of the vertical displacement at points P0-P4 (Fig. 2.2c) shows that the points located closest to the ocean floor (P0-P2) experience the strongest uplift and subsidence, whereas points P3 and P4 located at a depth of 15 km and 20 km, respectively, are barely affected by the sea-level changes. In the control run without sea-level changes, no vertical displacement occurs.
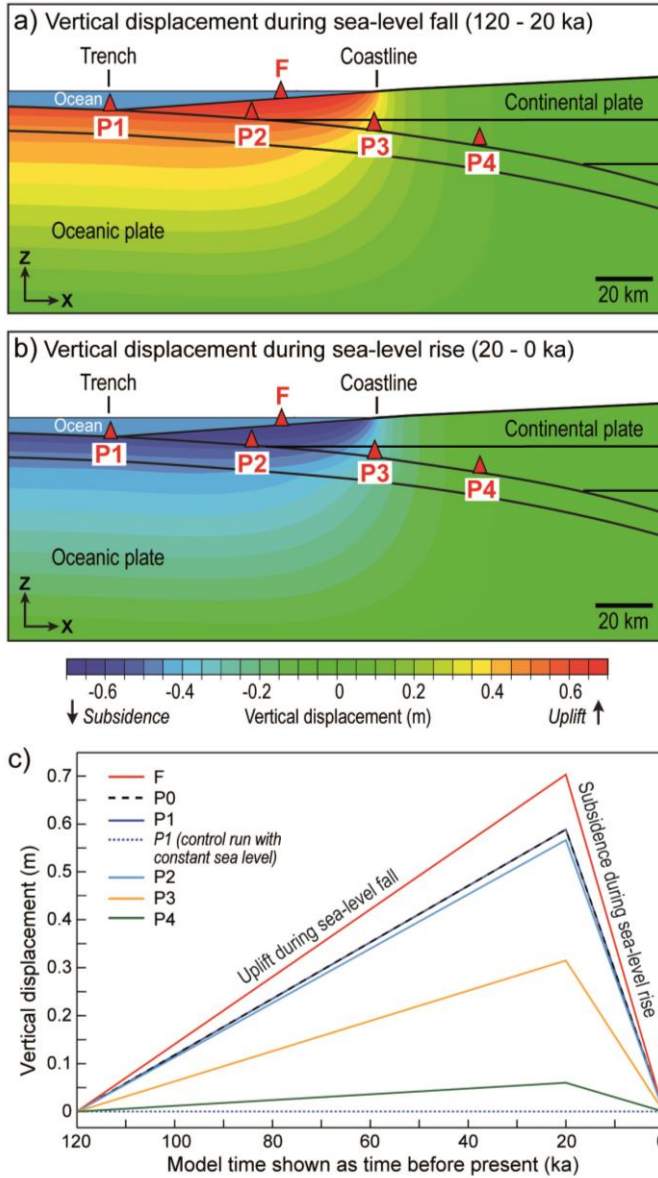
Horizontal displacement
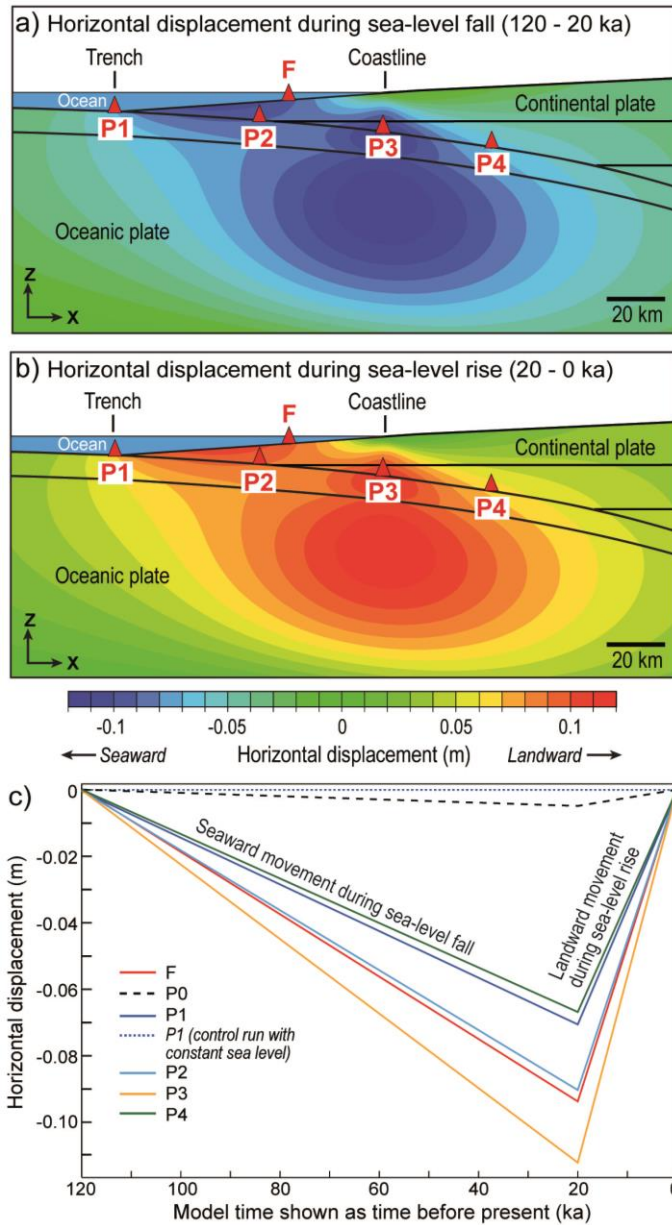
Figure 2.3 Horizontal displacement induced by a) a falling sea level (120-20 ka) and b) a rising sea level (20-0 ka). c) Temporal evolution of the horizontal displacements at point F in the forearc and at points P0-P4 located on the plate interface (Figs. 2.1a, 2.3a). For reference, the result from the control run (constant sea level) is shown for point P1.

The horizontal displacement (Fig. 2.3) induced by the sea-level changes reaches a maximum value of 0.12 m. The highest horizontal displacements occur in the submarine part of the forearc, beneath the coastline in the vicinity of the plate interface and in the oceanic lithospheric mantle. During the sea-level fall, the horizontal displacement is directed seaward (Fig. 2.3a), whereas

15

landward movements occur during the sea-level rise (Fig. 2.3b). Along the plate interface, the highest horizontal displacement occurs at point P3 (Fig. 2.3a, b). This implies that the distance between P3 and P1 decreases during the sea-level fall, whereas it increases during the sea-level rise. In contrast, the distance between P3 and P4 increases during the sea-level fall and decreases during the sea-level rise.

Stress changes

To illustrate the effect of the sea-level variations on the stress field, we extracted the changes in the vertical stress σ_z, the horizontal stress σ_x and the shear stress τ_{xz} between 120 and 20 ka (sea-level fall) and from 20 to 0 ka (sea-level rise) (Fig. 2.4). In concert with the changing water load, the vertical stress decreases during sea-level fall and increases during sea-level rise. The vertical stress changes have a maximum value of 1.23 MPa, which is equal to the magnitude of the applied water load, and primarily affect the region seaward of the coastline (Fig. 2.4a, b). Changes in the horizontal stress reach a maximum value of 0.75 MPa and are most pronounced in the
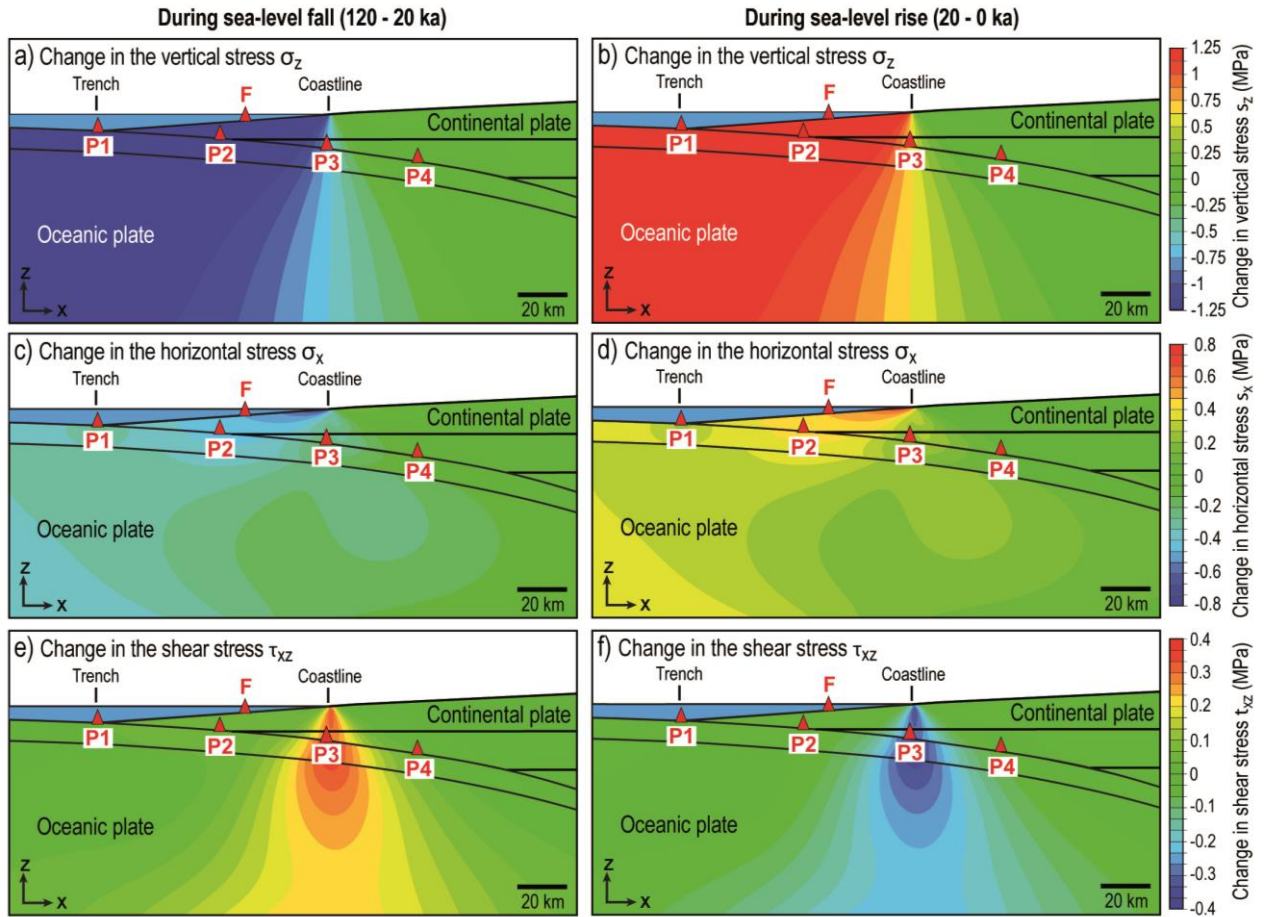
Figure 2.4 Stress variations caused by the sea-level changes. Left column shows the change in a) the vertical stress σ_z, c) horizontal stress σ_x and e) shear stress τ_{xz} during sea-level fall (120-20 ka). Right column shows the change in b) the vertical stress σ_z, d) horizontal stress σ_x and f) shear stressτ_{xz} during sea-level rise (20-0 ka).

submarine part of the forearc and on the plate interface in the vicinity of point P2 (Fig. 2.4c, d). In contrast to the vertical and horizontal stress, the shear stress increases during the sea-level fall, i.e. when the model region seaward of the coastline rises relative to the region landward of the coastline (Fig. 2.2a), and decreases during the sea-level rise. The shear stress change τ_{xz} is highest

(0.4 MPa) beneath the coastline and in the vicinity of point P3 (Fig. 2.4e, f), i.e. in the area that experiences the strongest flexural unbending and subsequent bending in response to the changing water load.

2.1.4 Discussion and conclusions

Our model results indicate that sea-level changes during glacial-interglacial cycles affect the displacement and stress field in the forearc, along the plate interface, and in the upper part of the downgoing oceanic plate. During a fall of the sea level, uplift and seaward movements prevail (Fig. 2.5a), whereas during sea-level rise subsidence and landward movements occur (Fig. 2.5b). The vertical displacements reach the highest values (up to 0.7 m) in the upper 10-15 km of the two plates and decrease rapidly with depth (Fig. 2.2). Although the horizontal displacements are relatively small (up to 0.12 m), the region that is affected is larger and located in the forearc beneath the coastline (Fig. 2.3). In our model, we used a simplified sea-level curve with a linear rise of the sea level over 20 ka, which results in maximum rates of vertical and horizontal displacements of 0.035 m/ka and 0.006 m/ka, respectively. Taking into account geological evidence indicating that the post-LGM sea-level rise occurred mainly between 15 and 5 ka at a rate of ~12 m/ka (e.g. Peltier and Fairbanks, 2006), increases the rates of subsidence and landward movement by a factor of two, respectively. For short time intervals in the late Pleistocene, the rate of sea-level rise even reached maximum values of ~30 m/ka, as shown by U/Th dating of corals (Bard et al., 1990). An additional factor that may further enhance the postglacial subsidence of the forearc and the oceanic plate is the transport of sediments from the continent to the ocean and their deposition in the forearc region and the trench. After glacial periods, the rates of sediment transport and deposition in the oceans have increased considerably (e.g. Church and Slaymaker, 1989; Hebbeln et al., 2007; Covault et al., 2011). The additional loading by sediments would further increase the flexure induced by the rising sea level. As shown by studies of the Cascadia and Chilean convergent margins, the postglacial sediment input was probably high enough to affect the style of deformation in the accretionary prisms (Bourgois et al., 2000; Adam et al., 2004).

The displacements caused by unloading and subsequent loading of the oceanic plate and the forearc are associated with changes of the vertical and horizontal stresses (Fig. 2.4). In the region seaward of the coastline, the vertical stress change is equivalent to the change in the water load and affects the entire lithosphere. It diminishes in a narrow transition zone underneath the coast (Fig. 2.4a, b). The spatial distribution of the vertical stress indicates that the area beneath the coastline experiences the strongest flexure, which is also reflected in the spatial distribution of the shear stress that is focussed in a bell-shaped area beneath the coast (Fig. 2.4e, f). Our finding that the region below the coast experiences the strongest variations of vertical and shear stress is consistent with the results from semi-analytical flexural modelling (Luttrell and Sandwell, 2010), which showed that the flexural stresses induced by eustatic sea-level variations are highest near the coast. In contrast to the study by Luttrell and Sandwell (2010), who approximated the Cascadia subduction thrust by a plane of constant dip, our model setup allows to analyse the spatial variations in displacement and stress along the convex contact between the bended oceanic plate and the continental plate. The results of this analysis are shown in Fig. 2.6 for a profile along

the plate interface between the trench, i.e. point P1, and point P4 located at a depth of ~20 km. With respect to the vertical displacement, the profile shows that the sea-level changes cause uplift or subsidence of 0.58 m in the shallow part of the plate interface (Fig. 2.6a). The vertical displacement decreases to almost zero at point P4. In contrast, the horizontal displacement reaches the highest values ~30 km landward of the trench and near point P3 (Fig. 2.6b). During the sea-level fall, the resolved normal stress on the plate interface decreases by up to 1.2 MPa beneath the submarine part of the forearc, i.e. in the shallow part of the plate interface, whereas it increases during the sea-level rise (Fig. 2.6c). Similar to the vertical displacement, the changes in normal stress diminish toward point P4. The change in the resolved shear stress on the plate interface has a peak beneath the coastline, where it reaches a value of 0.32 MPa at a depth of ~15 km (Fig. 2.6d). Beneath most of the submarine forearc, the change in shear stress is ~0.1 MPa.
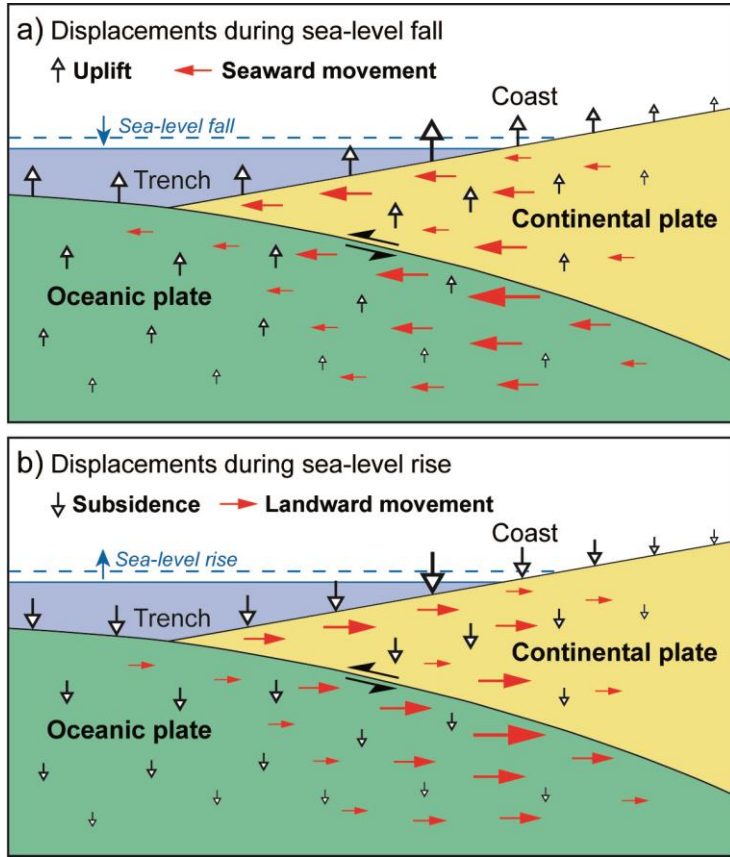
Figure 2.5 Sketch summarizing the vertical and horizontal displacements resulting from a) a falling sea level and b) a rising sea level (not to scale).

The part of the plate interface that experiences the most pronounced displacements and stress changes in the model coincides, in nature, with the upper portion of the seismogenic plate interface, which typically extends from a depth of a few kilometres to 30-50 km depth (Hyndman and Wang, 1995; Stern, 2002). As coseismic stress drops on inter-plate faults have been inferred to be of the order of 0.01-10 MPa (Kanamori and Anderson, 1975; Hanks, 1977; Scholz, 2002), the stress changes induced by sea-level variations may ultimately be able to promote or delay earthquakes in subduction zones. To evaluate the impact of the sea-level variations on the plate interface in more detail, we calculated the change in the Coulomb stress $\Delta C = \Delta\tau - \mu\Delta\sigma_n$, with $\Delta\tau$ being the shear stress change, μ the friction coefficient and $\Delta\sigma_n$ the normal stress change. For the

friction coefficient we used values of 0.1, 0.2 and 0.3, respectively. The results show that sea-level fall increases the Coulomb stress on the plate interface between points P1 and P4 (Fig. 2.6e), which implies that earthquakes are promoted by a falling sea level. The highest increase in Coulomb stress occurs beneath the coastline, where it reaches a value of 0.55 MPa for a friction coefficient of $\mu = 0.3$ and 0.4 MPa for $\mu = 0.1$. Beneath the submarine forearc, the Coulomb stress is increased by 0.46 MPa for $\mu = 0.3$ and 0.22 MPa for $\mu = 0.1$, respectively. In contrast, a sea-level rise reduces the Coulomb stress (Fig. 2.6f), with the minimum values occurring beneath the coast. This implies that the occurrence of earthquakes is delayed during a rising sea level.
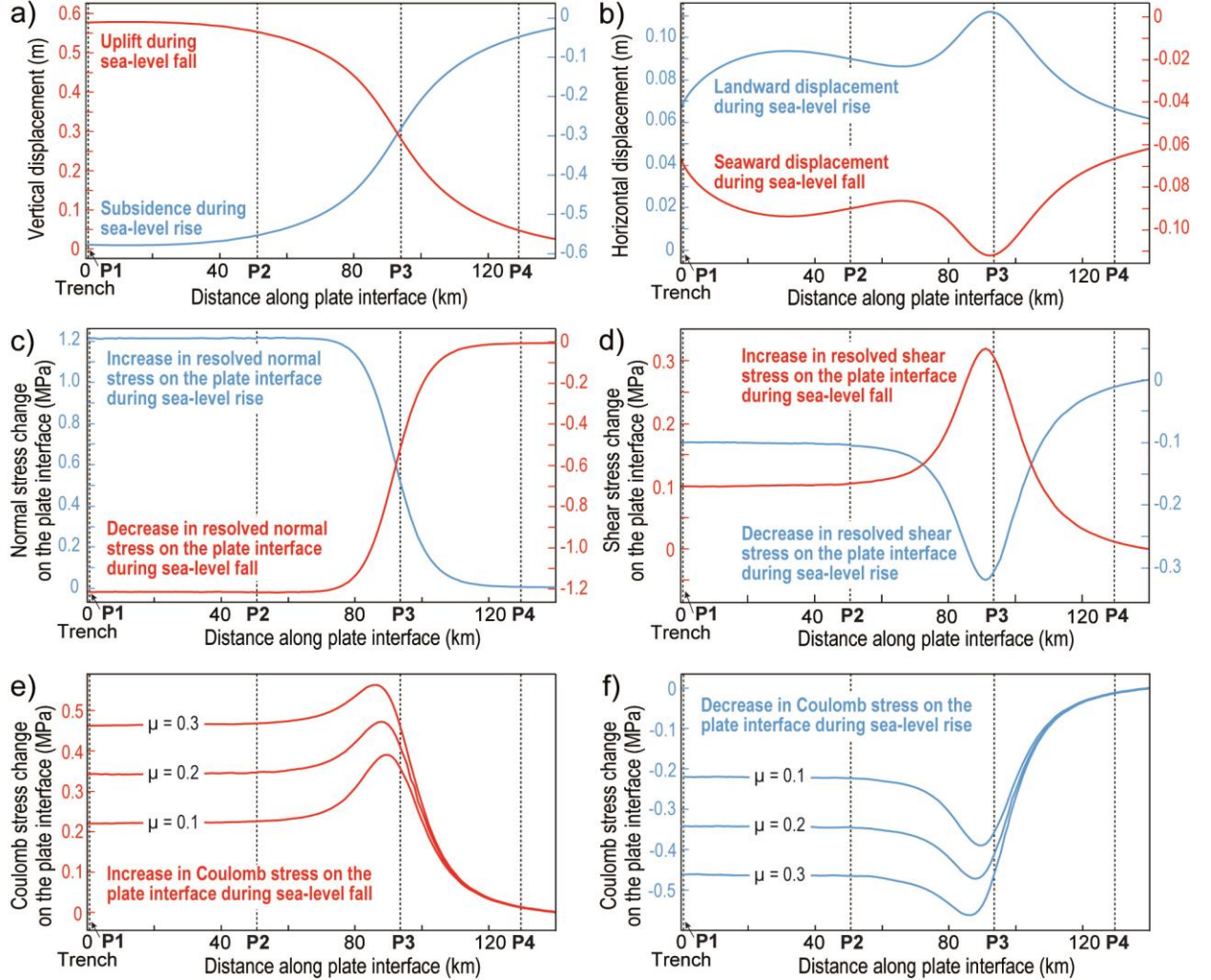
Figure 2.6 Profiles along the plate interface showing displacement and stress changes induced by sea-level fall (red curves and scales) and sea-level rise (blue curves and scales). a) Vertical displacement, b) horizontal displacement, c) resolved normal stress on plate interface and d) resolved shear stress on plate interface. Changes in the Coulomb stress e) during sea-level fall and f) during sea-level rise were calculated using different values (0.1, 0.2 and 0.3) for the friction coefficient μ. For location of points P1-P4 see Fig. 2.1a.

The promotion of earthquakes during sea-level fall and their delay during sea-level rise indicated by our model results may be recorded by sedimentary deposits in the forearc of subduction zones. For instance, at the southern Chilean active margin, turbidites were more frequent during glacial periods than during the Holocene and marine isotope stage (MIS) 5 (Blumberg et al., 2008). Under the assumption that the turbidites were mainly triggered by earthquakes, the authors infer

19

that the recurrence interval of large subduction earthquakes was 100-200 years during glacial periods. In contrast, the turbidite recurrence time was substantially higher during MIS 5 and the Holocene. Although the increase in turbidite recurrence time appears to be mainly controlled by a decrease in sediment availability (Blumberg et al., 2008), the reduction in Coulomb stress changes induced by postglacial sea-level rise may also have contributed to the increase in turbidite recurrence time by delaying earthquakes on the plate interface.

In conclusion, our two-dimensional finite-element model shows that sea-level changes may be able to affect the deformation in the forearc and the state of stress along the seismogenic part of the plate interface. During sea-level fall, seismic slip of the plate interface may be promoted, whereas it may be delayed by a rising sea level. Future modelling will be needed to assess the order of magnitude of the displacement and stress changes induced by sea-level variations if viscoelastic deformation, additional loading by enhanced late-glacial sediment deposition as well as coseismic and interseismic deformation of the upper plate are taken into account.

2.2 Effect of erosion and sedimentation on the displacement and stress field in the forearc and along the plate interface of subduction zones

2.2.1 Introduction and geological background

In Chapter 2.1, we used a two-dimensional numerical model to investigate the effects of eustatic sea-level change during the last glacial-interglacial cycle since ~120 ka on subduction zones (see also Li and Hampel, 2012). In this previous model, sediment erosion and deposition were not considered. However, climate-induced sea-level changes may also modulate the rate of sediment delivery across from the forearc to deep sea (e.g. Vail et al., 1977; Posamentier et al., 1991; Covault and Graham, 2010; Covault et al., 2011). By analysing the development of deep-sea depositional systems at major continental margins, Covault and Graham (2010) showed that deep-sea deposition of terrigenous sediment can occur at any sea level at the examined continental margins under different tectono-morphologic settings and climatic variability associated with glacial-interglacial transitions (e.g. change in subglacial discharge and/or in precipitation rate). Nevertheless, they observed that the sediment deposition rate during periods of marine transgression and low sea level since 35 ka is about twofold of the deposition rate during high sea level.
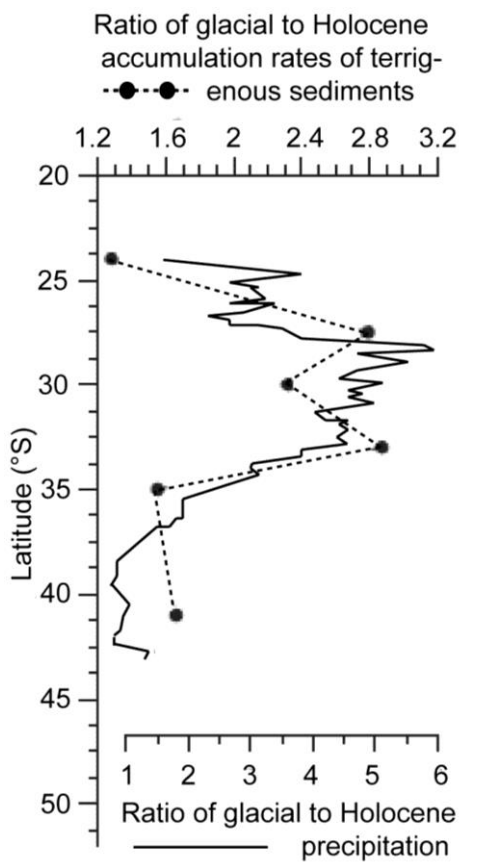
Figure 2.7 Glacial and interglacial precipitation and sedimentation patterns in and off Chile (modified from Hebbeln et al., 2007, Figure 2C. See methods for calulations of the ratios). Note the highest relative increase in accumulation rates during the LGM parallels the highest relatice increase in precipitation (Hebbeln et al., 2007).

The Andean margin is one of the ideal areas for studying the impact of climate change on erosion and tectonic processes due to its along-strike variability in temperature and precipitation (Montgomery et al., 2001; Melnick and Echtler, 2006). Compiling the

paleoenvironmental data and sedimentation rates over the past 24 ka, Hebbeln et al. (2007) showed a direct link between relative changes in precipitation and relative changes in offshore sediment deposition along Chilean margin (Fig. 2.7). They observed a more than twofold interglacial to glacial increase in the deposition of terrigenous material in north-central Chile, where the highest relative increase in precipitation during glacial period is expected. Similar correlations between continental erosion and glacial-interglacial climate are observed also in East Asia, though strong erosion was inferred to be more related to rock uplift and monsoon precipitation (Clift, 2006). Montgomery et al. (2001) derived hypsometric curves, which show the proportions of a landscape at different normalized elevations, for the Andes. In the southern part of Andes, the hypsometric curves show a shoulder pattern, which indicates high elevations have been strongly eroded by the glaciers (see Fig. 2 in Montgomery et al., 2001).

The rapid increase of trench fill off southern Chile during the last glacial period has been linked to the glacial erosion process as the southern Andes was covered by the extended Patagonian ice sheet during the LGM (Hallet et al., 1996; Denton et al., 1999; Melnick and Echtler, 2006; Hebbeln et al., 2007). Many studies have attributed the glacial-interglacial variations of offshore sedimentation rate along Chilean margin to the influences of climate change (Lamy et al., 1999, 2001; Völker et al., 2006; Hebbeln et al., 2007). Combined studies of seismic reflection surveys, bathymetric mapping, sediment profiles and core samples across Peru-Chile trench revealed that the sediment supply to the trench was strongly affected by the large fluctuations in glaciations during the Pleistocene (Völker et al., 2006).

The glacial-interglacial changes in sediment flux were inferred to have affected the deformation of accretionary prisms at the Chilean margin, where the Pleistocene glaciation has contributed significantly to fill the Chile Trench and accelerated accretion rates of trench fill (Bangs and Cande, 1997). Melnick and Echtler (2006) showed that the rapid increase of glacial trench fill since the Pliocene may have caused the shift from an erosive to an accretionary margin and the onset of forearc compression in south-central Chile. By investigating the turbiditic trench deposits covering a complete glacial to interglacial cycle (140 ka) at the south-Chilean margin, Blumberg et al. (2008) demonstrated that the turbidite recurrence times during glacial periods of low sea level are very similar to earthquake recurrence intervals within the last three millennia. They also determined a mean sedimentation rate without turbiditic deposition of 0.5 m/ka over the last 140 ka, which varies between 1 m/ka or more during the last glacial period and less than 0.1 m/ka during the Holocene (Fig. 2.8). Blumberg et al. (2008) related these marked contrast in the turbidite recurrence rates to the climate change, which can alter the sediment availability in the source area and eventually affect the slope stability. However, they also argued that the observed change in turbidite recurrence time may not only reflect changes in sediment flux but also indicate variation in local earthquake circle induced by glacial load or postglacial isostatic rebound in this region.

Modelling studies demonstrated that erosion and sedimentation may closely interact with the tectonic deformation during mountain building and continental subduction (Beaumont et al., 1992; Willett, 1999; Burov and Toussaint, 2007). Recently, Gray and Pysklywec (2012) applied a thermal-mechanical numerical model of continental collision and examined the

coupled processes of tectonic deformation and crustal mass flux. They demonstrated that the presence of sediment in the trench can lead to a greater degree of coupling between the continental plates and decoupling of the upper and lower crust of the incoming plate, which leads to a more diffuse style of upper-crustal deformation. So far, studies have been carried out to investigate the interaction between glacial-interglacial trench supply variation and the crustal deformation at continental margins (Bangs and Cande, 1997; Bourgois, et al., 2000; Contreras-Reyes et al., 2010; Contardo et al., 2011; Becerra et al., 2013). Based on a compilation of published and new seismic refraction and reflection data along the south central Chile margin, Contreras-Reyes et al. (2010) studied the processes of sediment
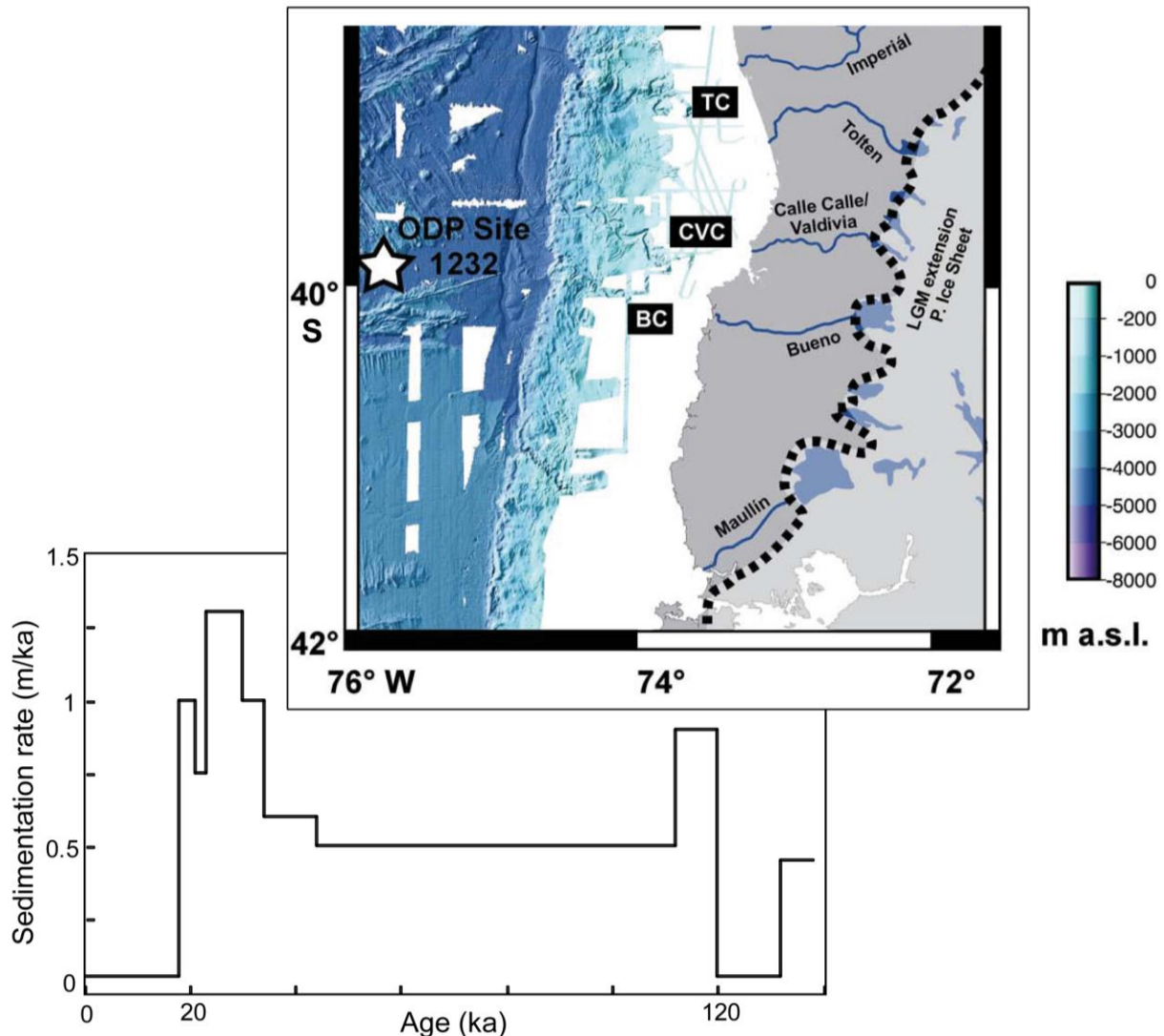
Figure 2.8 Sedimentation rate in southern Chile in the past 140 ka (after Blumberg et al., 2008). Blumberg et al. (2008) calculated the sedimentation rate based on the oxygen isotope records of ODP Site 1232 for the hemipelagic sections excluding the turbidites. The ODP Site 1232 is located at the outer rim of the Peru-Chile trench, ~85 km west of the continental slope in a water depth of 4072 m.

accretion and subduction and their implications on megathrust seismicity. They explained the differences in earthquake and tsunami magnitudes in terms of the size of frontal accretion prism, which can control the location of the updip limit of the seismogenic zone. However, the impact of erosion and sedimentation on the displacement and stress field of forearc and plate interface at subduction zones is not yet resolved. Against this background, the finite-

element model from Li and Hampel (2012) (Chapter 2.1) was modified such that the variations in sediment flux are included together with sea-level changes in the same glacial-interglacial cycle.

2.2.2 Modifications to the model setup in Chapter 2.1

Figure 2.9 a) Setup of the finite-element model with modifications to take into account erosion of the continental shelf and sediment deposition in the trench. All other parameters including the sea-level variations remain the same as in Li and Hampel (2012). The trench is located 4875 m below the surface of the model water body (termed "ocean" in the figure), which together with a pressure P_{oc} equivalent to 125 m of water represents a maximum water depth of 5000 m at the trench. Note that it was chosen to use a maximum water depth of 5000 m to allow direct comparison with the model without sea-level changes (Chap. 2.1), though the Peru-Chile trench is only 4000 m deep (Völker et al., 2006). A control run with a maximum water depth of 4000 m confirmed that the difference in the absolute water depth results causes only very minor differences in the displacement and stress fields. A box marks the model domain shown in b) and subsequent figures. b) Model forearc and the assigned pressures during model runs (left). Pressure variations due to erosion P_E (green arrows) and sediment deposition P_D (red arrows) at the forearc are simulated according to the erosion and sedimentation rates (right) inferred for the Chilean margin (Blumberg et al., 2008) (cf. Fig. 2.8). Bulk density of sediment is 1000 kg/m^3 (see explanations in text).

In the modified model, the geometry of the forearc was slightly changed such that it includes a 25-km-wide horizontal continental shelf (Fig. 2.9). The shelf represents the source area of sediment, which is subsequently deposited in the trench (Fig. 2.9b). All model steps are carried out as static states, i.e. viscous deformation is not considered. All model steps regarding to the establishment of the subduction zone geometry and isostatic equilibrium are performed as in the model from Li and Hampel (2012). During the final model step, erosion is implemented by decreasing the pressure at the continental shelf, whereas sedimentation is implemented by increasing the pressure at the trench. The pressure change is calculated simultaneously according to the assigned changes in the amount of eroded and deposited sediments, respectively (Fig. 2.9b). At the same time, the sea-level variations are implemented by varying pressure applied on top of the water body (Fig. 2.9a).

The assigned erosion and sedimentation rates are -1 m/ka and 1 m/ka during glacial period (120-20 ka) and reduced to -0.1 m/ka and 0.1 m/ka during the subsequent interglacial period (20-0 ka), respectively. The applied rates are based on the results from Blumberg et al. (2008) (see Chap. 2.2.1, Fig. 2.8). The bulk density of the sediment is assigned for 1000 kg/m^3 in the model, which is in the range of bulk densities of latest Pleistocene-Holocene turbidites offshore Southern California (Inman, 2008; Covault et al., 2011).

2.2.3 Results from models with erosion and sedimentation

In the following, the changes in the vertical and horizontal displacement as well as stress field in the upper part of a subduction zone are shown as cross-sections (Fig. 2.10-12). Additionally, the temporal evolution of these parameters is shown at seven selected points, i.e. point F located in the submarine part of the forearc, the reference point P0 and point P1 located 300 km and 6.4 km seaward to the trench at the surface of the ocean basin, respectively, and points P2-P5 located on the plate interface. The model time is shown as time before present in all the subsequent figures.

Vertical displacement

In the model with erosion and sedimentation, uplift dominates in the forearc as well as in the oceanic plate seaward to the trench during glacial period (120-20 ka). The highest uplift occurs in the forearc and the uplift maximum of 1.05 m is located on the continental shelf at point F (Fig. 2.10). Uplift diminishes ~20 km landward of the coast and below a depth of ~60 km in the oceanic plate. During the subsequent interglacial period (20-0 ka), the forearc and the oceanic plate subside by up to 0.7 m close to point F owing to the increase in the water load. Subsidence decreases gradually with depth. However, compared to the previous uplift, the amount of subsidence is smaller, but occurs throughout the ocean basin (Fig. 2.10b).

Along the plate interface (Fig. 2.10c), strongest uplift (~0.60 m) occurs at point P3. A similar amount of uplift also occurs at reference point P0. The vertical displacements of point P0 show the impacts solely from the sea-level changes, which correspond to the displacement at point P0 in Fig. 2.2c. Point P1 seaward to the trench experiences ~0.33 m of uplift during the glacial period but the strongest subsidence (~0.60 m) amongst the observation points during

the subsequent interglacial period. Point P5 that is located ~130 km landward to the trench and ~20 km below P1 is only negligibly affected by the climate-induced changes in sea level and sediment flux.
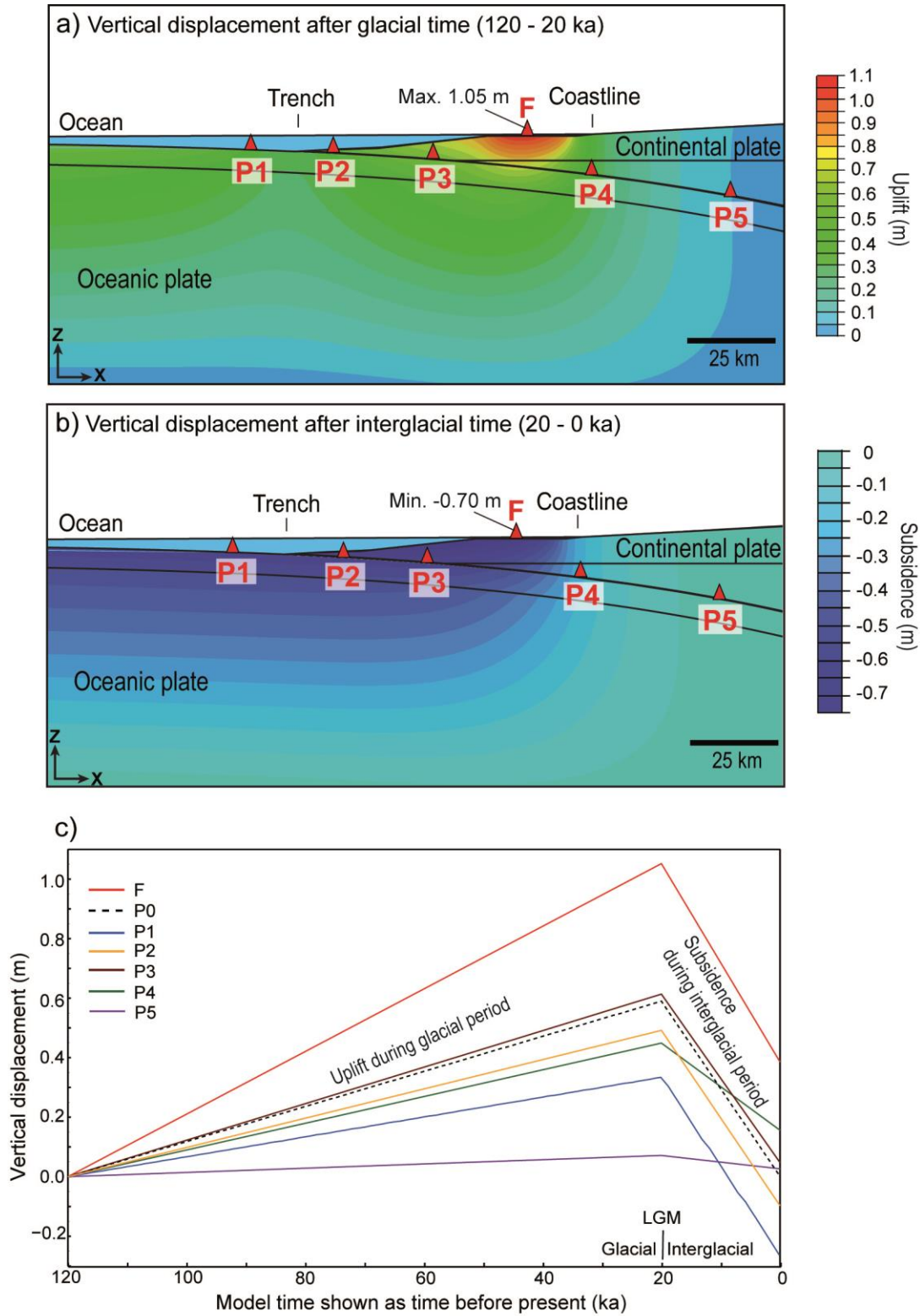

Figure 2.10 Vertical displacement during (a) glacial period with (120-20 ka) and (b) interglacial period (20-0 ka). (c) Temporal evolution of the vertical displacements at point F in the forearc, at point P1 in the deposition area and at points P2-P5 located on the plate interface (Fig. 2.9b).

26

Horizontal displacement

During the glacial period, seaward displacement with a maximum value of 0.15 m is induced at the upper part of the submarine forearc, whereas the region beneath the coast moves up to 0.11 m landwards (Fig. 2.11a). During the subsequent interglacial period, these regions move in opposite horizontal directions but the maximum landward displacement of 0.11 m occurs in the lithospheric mantle of the oceanic plate, whereas the regions beneath the coast move $\geq$ 0.06 m seawards (Fig. 2.11b). The magnitude of the horizontal displacement of points P2-P5 on plate interface is larger during the glacial period (Fig. 2.11c) than during the subsequent interglacial period, which is in contrast to point P1 at the ocean basin. Highest seaward horizontal displacement of plate interface reaches ~0.12 m and occurs at point P4. In comparison to points P2-P4, point P5 has the smallest difference between seaward and landward horizontal displacement. Regarding to the time evolution of horizontal displacement among P1, P4 and P5, this implies that the distance between P4 and P1 decreases during the glacial period, whereas it increases during the interglacial period. In contrast, the distance between P4 and P5 increases during the glacial period and decreases during the interglacial period.

Stress changes

The changes of the vertical stress σ_z, horizontal stress σ_x and shear stress τ_{xz} at subduction zone are shown by cross-sections in Fig. 2.12. During the glacial period, the vertical stress decreases in the ocean basin. Superimposed on this pattern are the effects of sediment erosion on the continental shelf and sediment deposition in the trench (Fig. 2.12a), which results in two main zones in the model domain with higher magnitude of change in the vertical stress. The zone with -2.2 to -1.4 MPa of decrease in σ_z is located beneath the submerged continental shelf and extends downwards with a ring-shaped pattern. The unloading of 125 m of water and 100 m of glacial sediment results to a decrease in σ_z by ~2.2 MPa at the submerged continental shelf. A zone of decrease in σ_z up to -1.2 MPa continues till reaching ~80 km in depth as well as dominates the region below the continental slope, which is mainly affected by the 125-m unloading of water in the model. Change in σ_z from -1.0 to -0.24 MPa is present beneath the trench, which indicates the compensation of the unloading of 125-m water by the loading of 100-m-thick glacial sediment. The oceanic plate seaward adjacent to this area experiences a vertical stress change of -1.2 MPa, which is equivalent to the sea-level fall. During the subsequent interglacial period, the vertical stress increases especially in the region beneath the ocean basin and seaward of the coast. The pattern as well as the magnitude of increase in σ_z is similar to the corresponding model results shown in Fig. 2.4b, where only sea-level changes are investigated.

The horizontal stress in the subduction zone domain generally decreases during glacial period (Fig. 2.12c); decrease up to -1.25 MPa occurs below the continental shelf. However, horizontal stress beneath the coast and at the trench increases by up to 0.25 MPa. In contrast, the interglacial horizontal stress change increases in the submarine part of the forearc with a maximum value of 0.65 MPa at the continental shelf (Fig. 2.12d).
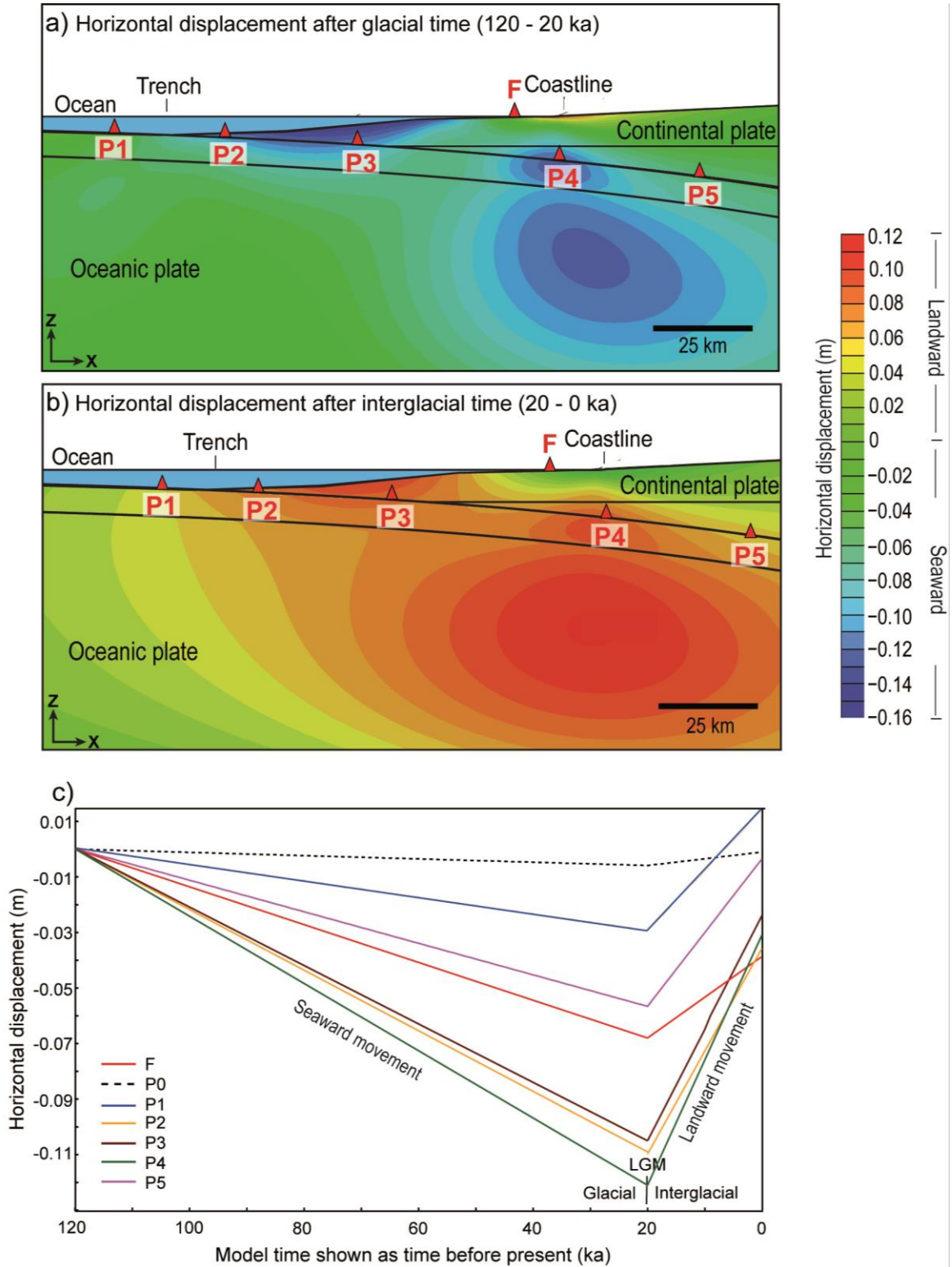
Figure 2.11 Horizontal displacement during (a) glacial period (120-20 ka) and (b) interglacial period (20-0 ka). (c) Temporal evolution of the horizontal displacements at point F in the forearc, at point P1 in the deposition area and at points P1-P5 located on the plate interface (Figs. 2.9b). For reference, the result from the control run (with only sea-level change) is shown for point P1.

With respect to the shear stress, τ_{xz} increases up to 0.59 MPa beneath the coast but decreases up to -0.29 MPa at the trench and below the edge of the continental shelf, respectively (Fig.

2.12e). During the subsequent interglacial period, the shear stress generally decreases (Fig. 2.12f), as the model domain seaward of the coastline subsides relative to the model domain landward of the coastline. Along the plate interface, changes in τ_{xz} are consistently largest in the section beneath the coast during the model time, where experiences the strongest flexural unbending and subsequent bending in response to the changing loads (Fig. 2.12e, f).
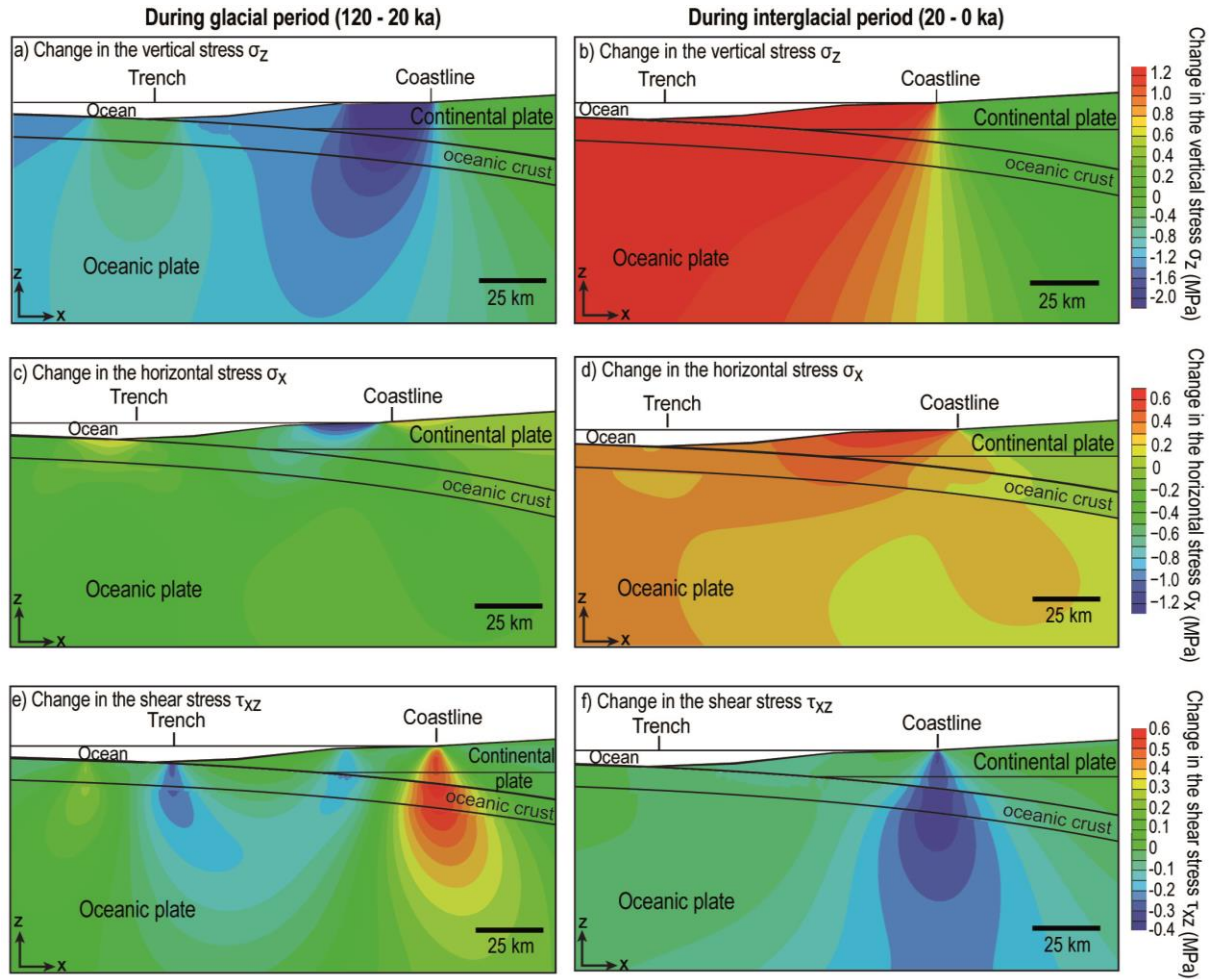

Figure 2.12 Stress variations caused by the glacial-interglacial load variations. Left column shows the change of (a) the vertical stress σ_z, (c) horizontal stress σ_x and (e) shear stress τ_{xz} during glacial period. Right column shows cross-sections of the model during (120-20 ka) with the change in (b) the vertical stress σ_z, (d) horizontal stress σ_x and (f) shear stress τ_{xz} during interglacial period (20-0 ka).

2.2.4 Discussion

The model results presented in this study demonstrate that load changes induced by sediment flux together with sea-level changes during a glacial-interglacial cycle can considerably perturb the displacement and stress field in the forearc and along the plate interface. The main application of this modelling study are subduction zones like the Chilean margin and the geometry of the model forearc is constructed according to the seismic reflection profiles in previous studies (e.g. Völker et al., 2006; Blumberg et al., 2008).

Although the examined sediment erosion-deposition scenario is relatively simple, it corresponds with the sedimentary history over the last glacial-interglacial cycle at the Chilean convergent margin. High trench infill is attributed to climatic conditions, e.g. high

precipitation, cold-humid climate (Lamy et al., 1998; Blumberg et al., 2008; Hebbeln et al., 2012) and local tectono-morphological factors, e.g. onset of glacial denudation in the uplifted high Andes and a decrease in plate convergence rate during the Pliocene (Melnick and Echtler, 2006). Analyses of the cores from ODP Leg 141 in southern Chile trench revealed high Pliocene-Quaternary trench sedimentation rates of 0.3-1 mm/a (Melnick and Echtler, 2006). A similar rate ~1 m/ka for the Pleistocene was determined by Blumberg et al. (2008), based on a gravity core in the Chile Trench. They speculated that the low sea level under glacial conditions exposes the continental shelf to erosion, which may enhance the terrestrial sedimentation rate and reduce the time and space for sediment accumulation. During the interglacial period, limited ice coverage as well as lower precipitation causes dramatic reduction on the source of terrigenous sediments (Hebbeln et al., 2007). Also, sea-level rise prevents sediments from being transported to the trench. Therefore, the sedimentation rate at the trench has been reduced to values of less than 0.1 m/ka (Blumberg et al., 2008).

A compare with the results of the model with only sea-level changes (Chap. 2.1) shows that the effect of the changing erosion and sedimentation rates on the displacement and stress field in the forearc is superimposed on the effect of the sea-level changes. During glacial period, the sediment deposition rate (1 m/ka) at the trench is comparable to the rate of sea-level fall (-1.25 m/ka), i.e. unloading of water is compensated by the sediment loading. Therefore, uplift at the trench in this model is only ~0.3 m (Fig. 2.10a), which would be ~0.3 m more if only sea-level fall is considered (see Fig. 2.2a). In contrast, erosion (-1 m/ka) induces a further decrease in the vertical stress together with the unloading of water at the continental shelf, and therefore uplift is enhanced, e.g. maximum uplift at point F is 1.05 m compared to 0.7 m with only sea-level fall. However, during the subsequent interglacial period, as sedimentation and erosion rates become one magnitude smaller than during the glacial period, the effect of the sediment flux is counteracted by the rising sea-level, which occurs at a rate of 6.25 m/ka. As a result, the model responds with only minor changes in displacement field in comparison to the model with only sea-level change (cf. Figs. 2.10b, 2.11b and Figs. 2.2b, 2.3b). The amount of horizontal displacement depends on the changes in sediment load, which vary spatially. The bending part of the oceanic plate as well as the overriding plate shows stronger seaward movement than landward movement. Furthermore, Figs. 2.10c and 2.11c show that the induced vertical and horizontal displacements in the upper part of forearc (point F) and the plate interface (point P1-P5) are not equal, which implies that permanent deformation would occur in nature. This pattern was not observed from the model in Chap. 2.1, where the changes in the displacement field had the same magnitude during the glacial and interglacial period, respectively (Figs. 2.2 and 2.3).

The deformation of model forearc is caused by changes of the vertical and horizontal stresses (Fig. 2.12). The two main patterns of vertical stress changes (Fig. 2.12a), which occur beneath the continental shelf and trench during glacial period, respectively, indicate that glacial sediment flux can significantly alter the stress field when erosion and sedimentation rates are comparable to the rate of the glacial sea-level fall. Moreover, the changes in sediment load can lead to stress changes deep in the lithospheric mantle of the subducting oceanic plate (Fig. 2.12a, c and e). This finding is consistent with previous modelling studies of continental

collision, which showed that surface processes may affect deformation in the mantle (e.g. Burov and Toussaint, 2007).

Compression and shortening of the forearc during the glacial period is reflected by an increase in the horizontal stress at the trench (Fig. 2.12c). In addition, a pattern of decrease in shear stress is observed that connects the trench and the left edge of continental shelf during glacial period (Fig. 2.12e). These model responses on stress changes during glacial period are consistent with the results by Melnick and Echtler (2006), which link the onset of forearc compression to the rapid growth of glacial trench fill. They investigated the forearc basins in south-central Chile, which comprise a nearshore stratigraphic sequence from the Eocene to the Quaternary by seismic reflection profiles and coastal exposures. They related the existence of the compressional forearc to the increasing trench fill since about the Pliocene, as the taper of the forearc wedge was continuously lowered by the increasing frontal accretion and subduction of water-rich sediment that reduce the basal effective friction. These processes together with a decreasing late convergent rate during the glacial cycles in Pliocene formed a wider seismogenic coupling zone and resulted in forearc compression.

Previous studies revealed that the offshore sediment accumulation rate at Chilean margin in Holocene may be consistently about twice lower than the previous glacial time due to a decrease in precipitation in southern Andes (Lamy et al., 1999, 2001; Hebbeln et al., 2007). Moreover, sea-level transgression or continuous highstand of sea level might inhibit also the transport of sediment from the continental shelf to the trench (Völker et al., 2006; Blumberg et al., 2008). As shown in Fig. 2.12b, d and f, the magnitude and patterns of the interglacial stress changes are similar to previous model results calculated with only sea-level rise (Fig. 2.4b, d and f), which indicates that ocean loading may play a more important role in this period with respect to changes in displacement and stress fields.

To analyse the evolution of the displacement and stress on the plate interface, we extracted the results along a 175-km-long profile along the plate interface, which starts at the trench and includes four points (P2-P5) (Fig. 2.13). P2 is ~18 km landward to the trench and P4 locates beneath the coastline on the plate interface. The patterns of displacement and stress changes at plate interface correspond to the glacial-interglacial stress changes in the model domain (Fig. 2.12), which reflect the combined effect of the erosion and sedimentation during sea level changes. As shown in Fig. 2.13a, uplift is about 0.32 m at the trench and increases till reaching a maximum of 0.73 m at ~70 km along the plate interface, which is beneath the continental shelf, and then it decreases almost to zero after P5. Subsidence is strongest at trench and continuously decreases to zero along the plate interface. The patterns of uplift and subsidence are asymmetric trenchward of point P4. With respect to the horizontal displacement (Fig. 2.13b), two maxima are shown at ~30 km from the trench and close to point P4 on the plate interface, respectively, where seaward displacement is stronger than the landward displacement relative to the trench. The decrease in the resolved normal stress shows at least 3 minima along the plate interface (Fig. 2.13c). At the shallower part of the plate interface (~10 km), the normal stress decreases by up to 0.2 MPa, which indicates that the deposition of glacial sediment compensates the effect of the sea-level fall. In comparison, the largest decrease of -2.2 MPa at ~73 km landward from the trench corresponds to the

unloading by sediment erosion and sea-level fall at the continental shelf. A transition zone with a stress change of about -1.2 MPa is presented on the segment from 10 to 50 km beneath the continental slope. The resolved shear stress increases by up to 0.53 MPa at ~80 km of the plate interface during the glacial period. However, decreases in resolved shear stress up to -0.17 MPa and -0.12 MPa occur at ~15 km and ~60 km landward to the trench, respectively.
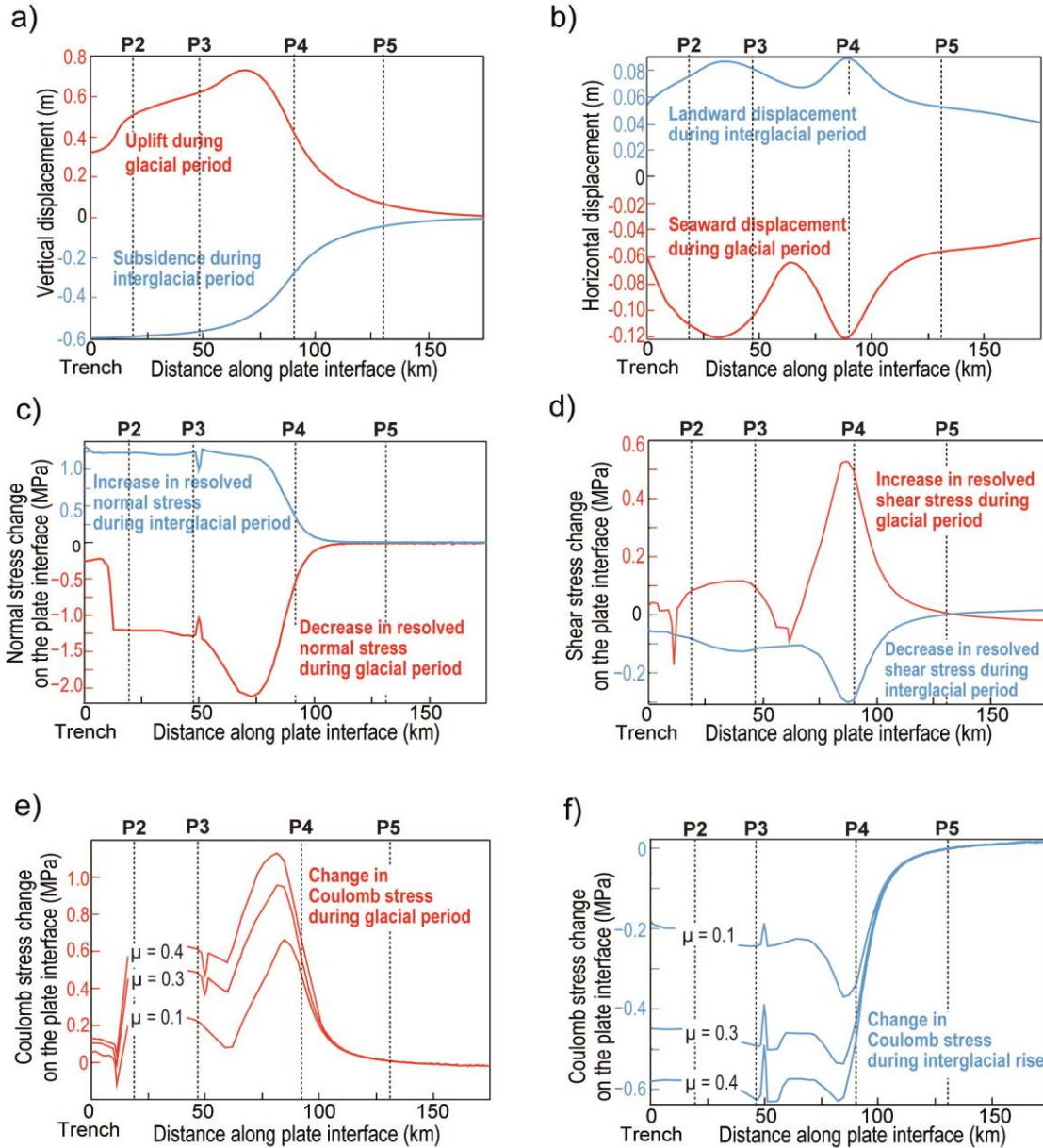

Figure 2.13 Profiles along the plate interface showing displacement and stress changes during glacial period (red curves and scales) and interglacial period (blue curves and scales). (a) Vertical displacement, (b) horizontal displacement, (c) resolved normal stress on plate interface and (d) resolved shear stress on plate interface. Change in the Coulomb stress (e) during sea-level fall and (f) during sea-level rise calculated for different values (0.1, 0.3 and 0.4) of the friction coefficient μ.

The observed glacial shear-stress changes on the plate interface correspond to the changes at the submarine forearc (see Fig. 2.12e). The decrease in shear stress indicates the deposition of glacial sediment may modulate the motion of the plate interface, if the sedimentation rate is comparable to the rate of sea-level fall. This may indicate the trench fill may play a major role in enhancing the coupling along plate interface, which was also inferred from previous studies

(Lamb and Davis, 2003 and references therein; Melnick and Echtler, 2006; Gray and Pysklywec, 2012). For example, Lamb and Davis (2003) calculated the plate interface shear stress with thermal modelling along the Andean margin and observed a significant decrease in shear stress in the high Andes at ~10° S, where there is a remarkable increase in the thickness of the trench fill. Melnick and Echtler (2006) found that the compressional forearc at south-central Chile is the result of continuous frontal accretion of glacial trench fill, which leads to a wider seismogenic coupling zone. During the subsequent interglacial period, the displacement and stress changes at plate interface (Fig. 2.13) are similar to the results in Chap. 2.1 (see Fig. 2.6) for the same period, which reflects the low sediment deposition rate (0.1 m/ka) in comparison to the fast sea-level rise (6.25 m/ka).

Compared to the coseismic stress drop on inter-plate faults that is generally of the order of 0.01-10 MPa (Kanamori and Anderson, 1975; Hanks, 1977; Scholz, 2002), the glacial-interglacial variations of normal and shear stress may be large enough to affect the seismicity of the plate interface. Similar to Fig. 2.6e, f in Chap. 2.1.4, the change in Coulomb stress is also calculated in order to evaluate the impact of glacial-interglacial sediment erosion and deposition on plate interface. Coulomb stresses were calculated with friction coefficients μ of 0.1, 0.3 and 0.4, respectively (Fig. 2.13e, f). The highest increase in Coulomb stress occurs between P3 and P4 beneath continental shelf, which reaches a maximum value of 1.13 MPa for a friction coefficient of 0.4 and 0.66 MPa for $\mu = 0.1$, respectively (Fig. 2.13e). However, along the shallower part of the plate interface ~12 km landward to the trench, the Coulomb stress increases only up to 0.15 MPa for $\mu = 0.4$ and 0.08 MPa for $\mu = 0.1$, respectively. An abrupt pattern in Coulomb stress changes with a decrease at ~12 km and subsequent increase to the maximum value at ~80 km (Fig. 2.13e) is coincident with the pattern in the resolved shear stress at the same position (Fig. 2.13d). A transition zone with a moderate change of ~0.6 MPa ($\mu = 0.4$) and ~0.25 MPa ($\mu = 0.1$), respectively, occurs between 13-60 km landward at the plate interface. The increase in Coulomb stress along plate interface corresponds with the spatial redistribution of glacial sediment, i.e. erosion at continental shelf and subsequent sedimentation at the trench. In the model with only sea level-changes, Coulomb stresses generally increases during sea-level fall over the plate interface until ~120 km landward and symmetrically decreases during the subsequent sea-level rise (Fig. 2.6e, f). Therefore, erosion may further enhance fault slip, whereas sedimentation may inhibit fault slip. In this case, earthquakes may be preferably triggered on the part of the plate interface that is beneath the continental shelf. In contrast, during interglacial period, Coulomb stress decreases along the plate interface until P5, where minimum values occur beneath the coast near P4. This implies that the occurrence of earthquakes is delayed during the interglacial period.

Seismic-reflection profiles and offshore stratigraphic records have provided evidence that an increase in the trench fill may be associated with earthquake occurrences in subduction zones (Ruff, 1989; Lamb and Davis, 2003; Blumberg et al., 2008). For example, based on the turbiditic trench deposits within the Perú-Chile trench over 140 ka, Blumberg et al. (2008) found that the thickness of glacial turbidites is generally much higher than the interglacial period. They assumed that the turbidites were triggered mainly by earthquakes and therefore

inferred that the high sediment availability and low sea level during the glacial period may contribute to the reduction of the earthquake recurrence rate to only 100-200 years. This finding is supported by the modelled changes of the Coulomb stress along plate interface shown in Fig. 2.13e.

2.2.5 Conclusions

This study investigated the impact on deformation of forearc and the stress state of plate interface of a subduction zone under the influence from the glacial-interglacial surface sediment erosion and sedimentation. With the modified two-dimensional finite-element model from Chapter 2.1, a simplified glacial-interglacial sediment scenario derived from the sedimentary record of Chilean convergent margin has been examined. In comparison to Chapter 2.1, the model results from the modified model demonstrate that the glacial sediment flux can additionally cause spatial variations in the forearc deformation as well as in the displacement and stress field of the plate interface. Owing to the elastic rheology of the model lithospheres, the effect of erosion and sedimentation is superimposed on the effect of the sea-level changes. Moreover, owing to the strong glacial sediment erosion at the continental shelf and subsequently high sedimentation in the trench, uplift of the forearc is enhanced at the continental shelf and seismic slip is promoted at the plate interface beneath. In contrast, uplift is reduced at the toe of the forearc and the seismic slip of the plate interface between trench and continental shelf can be delayed. However, as the rate of sediment flux is one magnitude smaller during the interglacial period, the influences from sediment erosion and sedimentation are small compared to the effect from the sea-level rise.

Previous studies have shown that the sedimentation flux at Chilean margin from the Pliocene to the Holocene could be strongly influenced by the climate conditions (e.g. high or low precipitation and sea-level changes) and local tectonic factors (e.g. plate convergence and uplift rate). Therefore, the implementation of glacial-interglacial sediment flux is important for the study of the interaction between climate and tectonics at subduction zones. Although the applied scenario of erosion and sediment deposition is simple, this study sheds light on the potential response of the forearc and plate interface to climate-induced changes in surface loads.

3. Two- and three-dimensional models of earthquake cycles

3.1 Introduction and motivations

Earthquake cycles in subduction zones

The cyclic build-up and release of tectonic stress in the seismogenic region of subduction zone earthquakes is reflected by the patterns of crustal deformation (Thatcher and Rundle, 1984). Geodetic, seismological and analytical as well as numerical modelling studies have revealed the interseismic and coseismic deformation patterns at subduction zones (Thatcher and Rundle, 1984; Hyndman and Wang, 1995; Cohen, 1999 and reference therein; Turcotte and Schubert, 2002). During the interseismic phase, uplift prevails in the coastal region, whereas the submarine part of the forearc and the area landward of the coast experience subsidence; horizontal displacements of the forearc are typically directed landward (Fig. 3.1a) (Thatcher and Rundle, 1984; Savage and Thatcher, 1992; Hyndman and Wang, 1995). During the coseismic phase, subsidence occurs at the coast, while the neighbouring regions experience uplift (e.g. Dragert et al., 1994; Hyndman and Wang, 1995; Klotz et al., 1999; Ozawa et al., 2012); in the entire forearc seaward horizontal displacements occur (Fig. 3.1a and b) (e.g. Klotz et al., 1999; Kodaira et al., 2012). Studies dedicated to understanding these displacement patterns showed that the displacement patterns can be explained by the fact that the ongoing subduction drags down the overriding plate because a portion of the plate interface is locked. As a consequence, elastic strain is accumulated in the forearc and results in flexural uplift farther inland along with crustal shortening owing to the landward movements (e.g. Hyndman and Wang, 1995). This accumulated strain is fully or partially released by one or series of earthquakes, which causes coseismic subsidence and seaward movements, as well as slip of up to tens of meters on the plate interface (Kanaromi, 1986; Chlieh et al., 2007; Ozawa et al., 2012). Apart from these characteristic displacement patterns, trench-parallel variations on displacement and strain accumulation rates have also been observed, e.g. GPS data sets show along-strike shifts from compressional to extensional tectonic deformation within the upper plate in New Zealand, Japan, and Vanuatu (Wallace et al., 2012, and reference therein). Such findings are mostly attributed to the along-strike variation in the depth and downdip limit of interseismic coupling (Wallace et al., 2012; Wang et al., 2012). The vertical and horizontal displacement rates are commonly determined from geodetic observations. Many earlier geodetic observations relied mainly on levelling and tide gauge data, particularly for determining the interseismic vertical deformation in the coastal area (e.g. Fig. 3.1a) (see also Thatcher and Rundle, 1984; Savage and Thatcher, 1992). However, tide gauge data must be corrected for relative sea-level changes and the resolution in time and space of these records is usually limited. Moreover, tide gauge data are more reliable for determining deformation occurring seaward of the coast, except when the trench is close enough to coast that significant deformation can be measured on land, e.g. at the Nankai Trough subduction zone in SW Japan (Thatcher, 1984a; Savage and Thatcher, 1992). The application of Global Positioning System (GPS) since the early 1990s has enabled more detailed and larger-scale investigations on crustal deformation (Dragert and Hyndman, 1995;

Klotz, 1999; Wang et al., 2012) (e.g. Fig. 3.1b). With this method, measurements of relative motions among different regions, as well as continuous monitoring of co-, post- and interseismic deformation at many subduction zones became possible by the dense network of GPS monitoring stations, e.g. in the subduction zone of Japan (Wang et al., 2012). Dense GPS monitoring has also been applied since the 1990s in Chile, which is considered as an ideal natural laboratory for quantifying the spatial variations of interseismic coupling, given its fast convergent rates and relatively simple structures without diverse slip directions in the central part (Klotz et al., 1999; Métois et al., 2012). The interseismic uplift rate at convergent margins is determined commonly a few millimetres per year at the coast and decreases landwards (Thatcher, 1984b; Hyndman and Wang, 1995). The flexural uplift and the transition between interseismic subsidence and uplift can be further landward for a
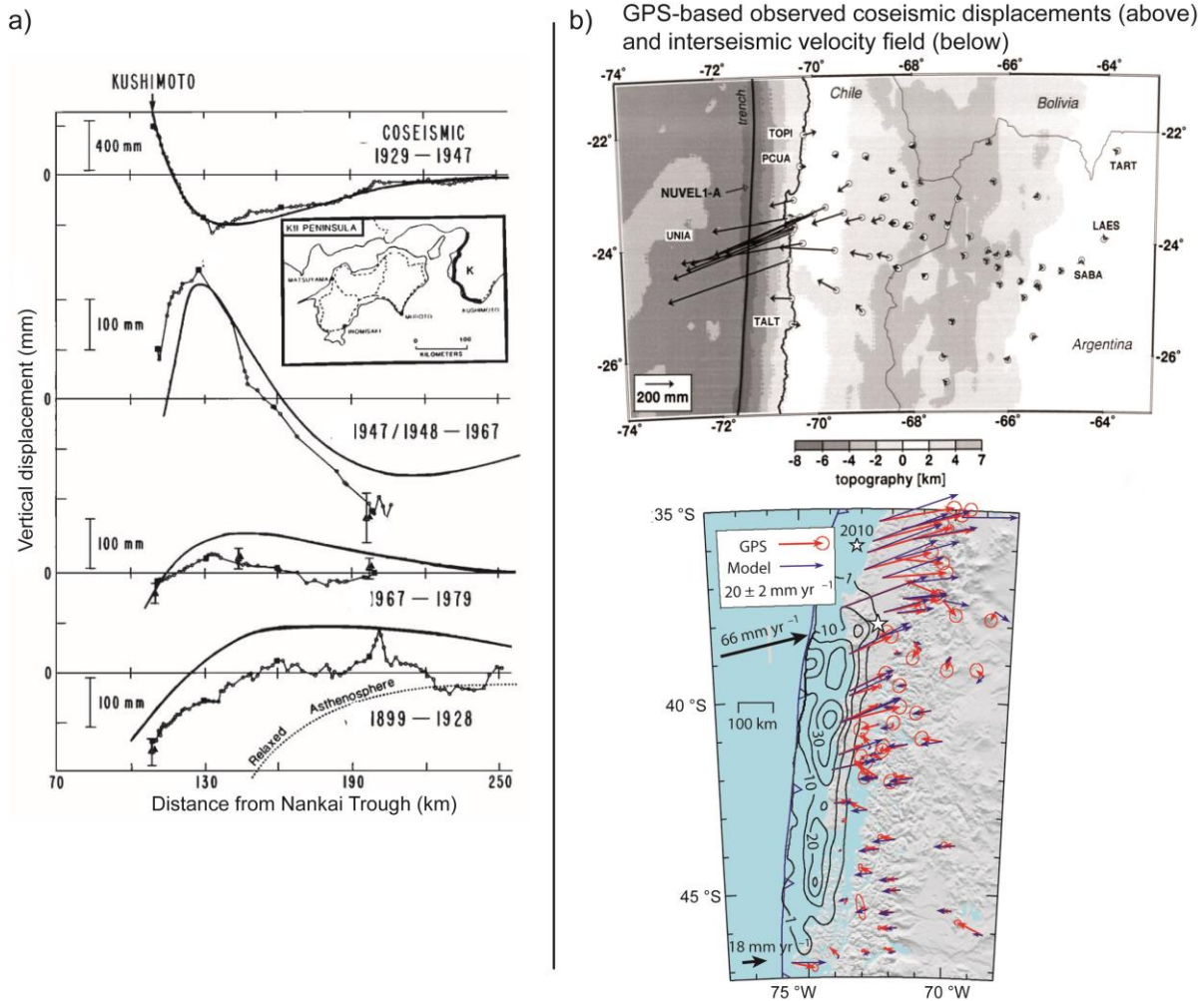

Figure 3.1 a) Observed levelling (dotted lines) and tide gauge data (triangles with one standard deviation error bars) in southwest Japan compared with model results (solid lines) in Thatcher and Rundle, 1984 (modified from fig. 14 in their work); b) examples of GPS observed coseismic horizontal displacements of northern Chile and northwest Argentina (above) and interseismic velocity field at Chile (below). In the upper image, the vectors represent computed motions relative to stations TART, LAES, and SABA in the eastern part of the network, where the motion was fixed to zero. Displacements are based on station positions measured 21 months prior to and 3 months after the 1995 M_w 8 Antofagasta earthquake (modified from Klotz et al., 1999). In the lower image, red and blue arrows indicate GPS and model-predicted interseismic velocity field at Chile, respectively, which is four decades after the 1960 M_w 9.5 earthquake (epicentre indicated by the larger white star). Estimated coseismic slips of the 1960 earthquake are delineated with black isoclines (modified from Wang et al. 2012).

wider seismogenic zone (Hyndman and Wang, 1995). Crustal shortening commonly occurs at the coastal region during the interseismic period. The shortening rate strongly depends on the plate convergent rate and the interseismic coupling of the plate interface (Kato and Yoshida, 2011; Wallace et al., 2012). For example, Klotz et al. (1999) derived a crustal shortening rate of 3-4 mm/a in northern Chile from GPS data observed two years before and after the 1995 Antofagasta $M_w = 8$ earthquake. They compared their results with the previously determined long-term shortening rate of ~10 mm/year in Central Andes within 27 million years, and attributed this decrease in shortening rates to the changes in the degree and distribution of seismic coupling along the plate interface. Coseismic subsidence accompanied by seaward displacement can be up to a few meters in the coastal area and depends on the pattern of interseismic strain accumulation in the upper plate and the recurrence time of earthquakes (Thatcher and Rundle, 1984; Hyndman and Wang, 1995). The slip resulting from the release of interseismic strain can be meters to tens of meters. For example, the observed seaward coseismic displacements of the 2011 $M_w = 9$ Tohoku-Oki earthquake reached up to 5 m and subsidence by up to 1.2 m along the coastal line of Tohoku region, relative to Fukushima site, where the estimated coseismic slip near the epicentre was up to 27 m (Ozawa, 2011). However, observed data spanning over the entire earthquake cycle are still limited owing to the long recurrence times between great earthquakes, therefore, historical data are still important (Cohen, 1999).

Modelling of subduction zones

Elastic dislocation models have been broadly used for simulating the interseismic deformation at subduction zone or to explain the deformation patterns observed by geodetic measurements (e.g. Savage, 1983; Thatcher and Rundle, 1984; Dragert et al., 1994). The principal of elastic dislocation models is the assumption that the deformation of a viscoelastic Earth throughout an earthquake cycle results from coseismic slip, afterslip and fault locking in an elastic half-space model domain, and inelastic deformation is ignorable within relative short timescales as the seismic cycle (Savage, 1993; Kanda and Simons, 2010). Surface deformation at subduction zones is simulated by assigning a reverse dip-slip imposed on the downdip end of the locked plate interface imposed on the locked plate interface, i.e. commonly by considering interseismic fault slip as a normal slip, which is known as back-slip models for calculating cumulative interseismic deformations (e.g. Savage, 1993; Hyndman and Wang, 1993; Hyndman et al., 1995; Zhao and Takemoto, 2000). The advantages of applying elastic dislocation models are the simplifications of the subduction zone geometry and material properties, e.g. a homogenous elastic half-space model (e.g. Dragert et al., 1994; Hyndman and Wang, 1995; Hyndman et al., 1997; Wang and He, 1999). Alternatively, thickness of the elastic plate and bending stresses can be included into back-slip models, but these models assume that flexural stresses of the subducting plate are released continuously during bending or at depth (Kanda and Simons, 2010). As numerical modelling techniques and computational capacities have advanced, more sophisticating modelling studies about the influence of interseismic plate coupling on deformation and earthquake cycles have been carried out (e.g. Hu et al., 2004; Cailleau and Oncken, 2008; Kato and Yoshida, 2011). Those studies have demonstrated that the inhomogeneities of the plate interface regarding depth extent, length

and frictional properties can influence the interseismic deformation and stress accumulation as well as the coseismic, postseismic and aseismic slip on the plate interface. These parameters are considered as crucial for generating great earthquakes (e.g. Hu et al., 2004; Métois et al., 2012; Ozawa et al., 2011, 2012). Moreover, models were developed for calculating along-strike variations on interseismic coupling rate, which have been observed at many convergent margins (Kanamori, 1986; Kato et al., 2011; Wallace et al., 2012; Wang et al., 2012). However, previous modelling studies often assumed a pure elastic and/or homogenous half-space, in which the effects of viscoelastic flow in upper mantle and the lower crust on time-dependent deformation are not considered (Cohen, 1999). In their review, Wang et al (2012) pointed out that ignoring the role of viscous mantle flow in interseimic surface deformation will lead to incorrect depiction of the locking state of the subduction fault, since the deformation can then be mainly, or only, attributed to the locking and slip of various part of the subduction faults. It has been pointed out by Masterlark et al. (2001) that three-dimensional finite-element models are better suited for simulating tectonic deformation during all phases of the seismic cycle, because they can take into account variations in material properties, boundary condition and contact surface interactions. Recently, on the basis of 3-D finite-element modelling approach, Trubienko et al. (2013) argued that lateral viscosity variations associated with the slab at depth and low viscosity wedge should be taken into account, which may affect the predictions on interseismic velocities.

So far, only few modelling studies investigated forearc deformation over one and more earthquake cycles. This became the motivation of the study presented here, which applies 2-D and 3-D finite-element modelling. First, systematic variations in the parameters controlling the plate interface were carried out to investigate the behaviour of the upper plate with layers of different viscoelastic properties during one earthquake cycle. The 2-D experiments carried out aim at examining the influence of heterogeneous frictional properties and the position and length of the seismogenic zone on the interseismic and coseismic displacement patterns of the upper plate as well as on the coseismic slip on the plate interface. Afterwards, 3-D experiments were carried out to investigate the effect of lateral variations of the studied parameters on the displacement patterns, and their results were compared with previous 2-D models. Finally, additional 3-D modelling has been carried out for addressing more realistic cases focusing on the effect of a heterogeneous spatiotemporal distribution of earthquake sequences. The models were designed for the application to the Chilean margin, where the rupture zones of two subsequent large earthquakes (1960 M_w 9.5 Valdivia and 2010 M_w 8.8 Maule) overlapped (Moreno et al., 2011; Métois et al., 2012), and to the Japanese margin where a sequence of M_w 7 earthquakes occurred before the March 2011 Tohoku-Oki earthquake (Kato and Yoshida, 2011; Ozawa et al., 2012).

3.2 Setup of the finite-element models

3.2.1 Two-dimensional subduction-zone models

Subduction zone models applied in this study are established with the finite-element commercial code Abaqus standard (version 6.12). The 2-D subduction-zone model consists of a subducting plate and an overriding plate. The plate interface between them is simulated as contact surface, which is initially divided - from the trench to the base of the continental lithosphere - into a seismogenic zone, a transition zone and a landward free slip zone. Note that these three zones are different mainly in length and their frictional coefficients, which has been initially assigned with 0.1, 0.3 and 0 (frictionless), respectively (Fig. 3.2). The friction coefficient of the transition zone remains constant in the pre- and interseismic phases but is changed to the values in seismogenic zone in the coseismic phases. The subducting plate is simulated as a rigid analytical body, i.e. undeformable during the simulation, while the upper plate is deformable. Deformation of the subducting plate is assumed ignorable here, given the recurrence time of great earthquake commonly falls in a relative short timescale, e.g. several hundred years. Also, the focus of this study is the deformation and stress accumulation in the upper plate over one or more seismic cycles. The upper plate is subdivided into a 20-km-thick elastic upper crust, a 20-km-thick viscoelastic lower crust overlying a 70-km-thick viscoelastic lithospheric mantle. The rheological parameters are shown in Fig. 3.2. Plate convergence is simulated by prescribing an angular velocity on the subducting plate, which is equivalent to a convergence rate of 100 mm/a along the plate interface (cf. Cailleau and Oncken, 2008).
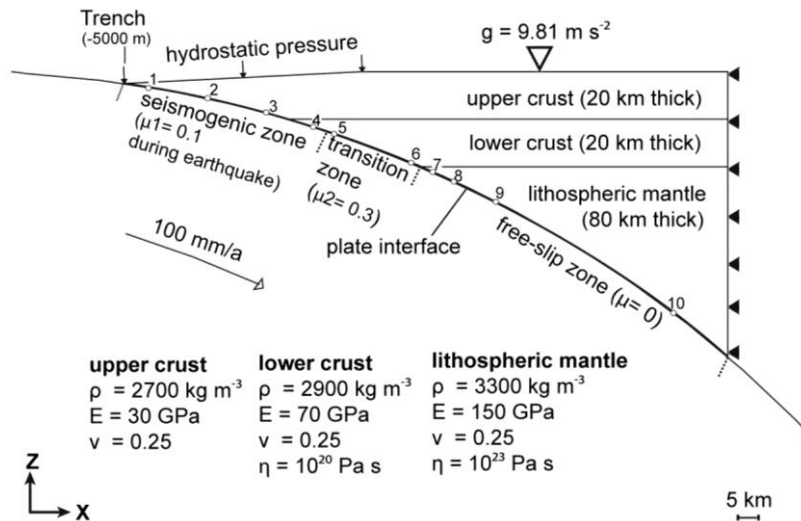

Figure 3.2 Model setup of the applied 2-D subduction-zone model. Hydrostatic pressure equivalent to a 5000-m-deep ocean is assigned at the continental slope of the upper plate, which is highest at the trench and reduces to zero at the coastline. Material properties of the layered lithosphere of the upper plate are listed below the model. The model plate interface is subdivided into seismogenic zone, transition zone and free-slip zone, in which the frictional properties are different. Stable sliding is allowed at the free-slip zone accommodated with the 100 mm/a assigned subducting rate. Numbers 1-10 at plate interface indicate locations where simulated slip histories are shown in Fig. 3.4. Note that this model setup is applied for the reference model (REF).

The elements used in the 2-D models are quadratic triangular plane-strain elements with a

mean edge length of 5000 m. As an initial step, the model is first run for 100,000 a with no motion of the subducting slab. At this stage, a Poisson's ratio $\nu = 0.5$ is applied, i.e. the material is incompressible, so that the lithostatic prestress can be established when gravity is invoked (cf. Wang and He, 1999). The gravity increases from zero to its maximum values in this step, which stabilizes the contact between slab and upper plate with no sliding observed in the seismogenic and transition zones (cf. Cailleau and Oncken, 2008). The accumulated stresses are then imported as initial stress field into a second model run, in which now $\nu = 0.25$ is applied. The gravity is fully assigned at the upper plate since the beginning of a new first step, in which the convergence begins (cf. Cailleau and Oncken, 2008). The seismogenic zone of the plate interface is locked over 100 a (preseismic phase). It is allowed to slip during the subsequent step for 60 s (coseismic phase) and then locked again for another 100 a (postseismic phase).

In the subsequent models, three different values of friction coefficient μ (0.1, 0.2 and 0.3) were examined in the seismogenic zone. Also, the length of the seismogenic zone, i.e. the position of the downdip limit was varied (Fig. 3.9). The results of these models are described in section 3.3.1 and 3.3.2, respectively.

3.2.2 Three-dimensional subduction-zone models

The three-dimensional (3-D) finite-element models consist of an undeformable subducting plate and an overriding plate (Fig. 3.3).
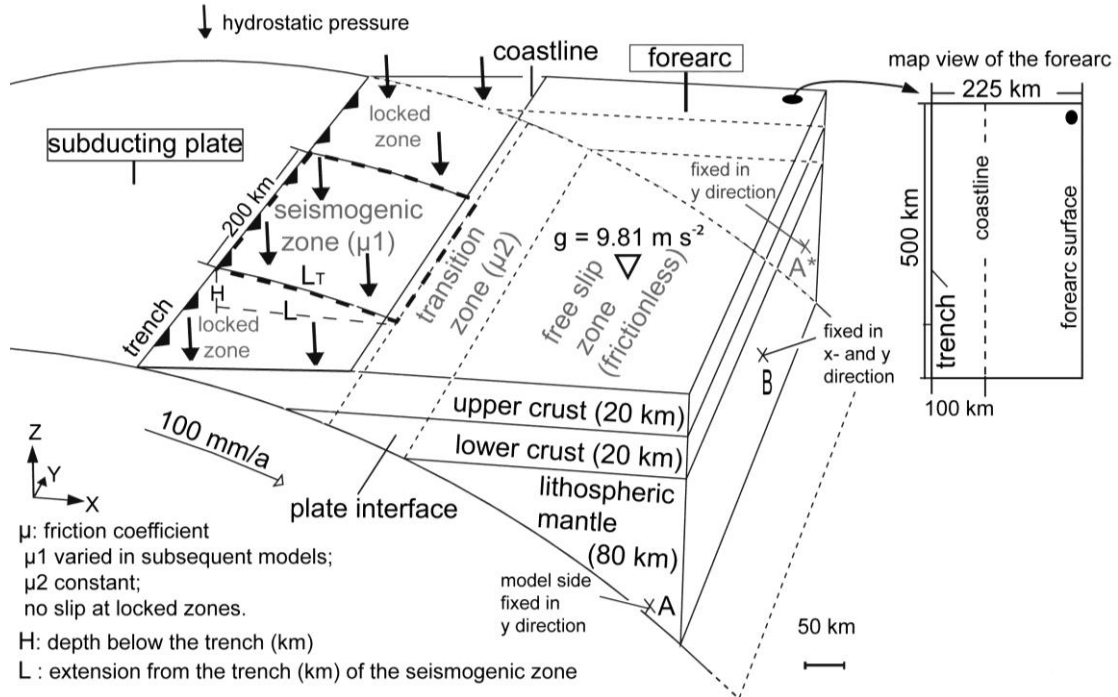

Figure 3.3 Model setup for the 3-D subduction zone model. The dimensions of the model are given by the map view of the forearc surface. Motions of side A, A* and B of the upper plate are constrained by given boundary conditions, respectively. The geometry and dimension of the seismogenic zone are varied (see text). Gravity and hydrostatic pressures are also considered. Pressures equivalent to 5000-m-deep ocean are assigned at the surface of the forearc seaward to the coastline, which reaches maximum value at the trench and reduces to zero at the coastline. Rheological parameters of the layered lithosphere of the overriding plate are same as in the 2-D models (see Fig. 3.2). This model step is applied for the 3-D reference model (REF-3D).

40

The applied elements of the 3-D models are linear tetrahedral 3-D stress elements with a mean edge length of 5000 m. Similar to the 2-D models, the overriding plate is subdivided into three layers, i.e. an elastic upper crust, a viscoelastic lower crust and a viscoelastic lithospheric mantle, which are homogenous and assigned with same material properties as in the 2-D models (see Figs. 3.2, 3.3). In order to test the impact of the lateral extent of the subduction zone, the same subduction zone geometry was taken for the 3-D models as in 2-D models but extended by 500 km in the along-strike direction. Each side of the overriding plate (indicated with A, A* and B in Fig. 3.3) are constrained by boundary conditions so that the influence of the deformation at the model boundaries can be minimized. The plate interface is initially subdivided into a seismogenic zone that is centred in the model domain and surrounded by two locked zones and a transition zone, and a free-slip zone, which extends to the bottom of the model. In the parameter study, the along-strike extension of the seismogenic zone is 200 km and located in the centre of the shallower portion of the plate interface and between the two locked zones. Note that the locked zones and the seismogenic zone are refined by elements with a 2000-m edge length. Simulations of each 3-D model have been carried out similar to the work flow applied in the 2-D models (see Chap. 3.2.1). Initial stress was calculated and imported at the beginning of the preseismic phase. In this phase, the seismogenic zone is locked, i.e. no slip is allowed in this region, and then it is released (coseismic phase) and subsequently locked again (post- or interseismic phase). Note that the locked zones in 3-D models are locked throughout the simulation.

In subsequent models, the friction coefficient ($\mu 1$) and the depth (H) as well as the landward extension (L) of the downdip limit of the seismogenic zone were varied (see Figs. 3.3, 3.9). The modelling results are shown in Chap. 3.3.2 and compared with the 2-D models in Chap. 3.3.3, respectively.

3.3 Model results

3.3.1 2-D model results

In the following section, results of the 2-D modelling in this study are presented. Slip histories of observation points 1-10 of the 2-D reference model (see Fig. 3.2) are shown in Fig. 3.4. The step-like increase in slip rate at point 1, 2, 3 and 4 (P1- P4) in the seismogenic zone indicates the coseismic fault slip, of which the highest magnitude of 14.5 m occurs at P2. The maximum coseismic slip of 14.7 m occurs close to P2, which indicates the centre of the seismic rupture zone located at the shallower segment of the plate interface. Coseismic slip decreases with increasing depth and the effect of the earthquake on slip rates is strongly reduced in the downdip direction away from the seismogenic zone. Steady-slip occurs in the preseismic phase at P5 and P6 of the transition zone as well as at P7-P10 situated in the free-slip zone. Slip rates recover to steady slip rates within a few years after the coseismic phase. However, the subsequent interseismic slip rate at P5 has been changed, i.e. the preseismic slip rate was disturbed by the earthquake, which leads to change in slip direction. This phenomenon is not observed in P6 that is close to the downdip end of transition zone. Because of the frictionless contact in the free-slip zone, the transient slip rates at P7-P10 are comparable to the assigned subducting rate (100 mm/a); they increase with depth and reach

up to 99 mm/a at P10. In the free slip zone, slip rate was increased after the earthquake, e.g. at P7, but this effect reduces from P7 to P10.
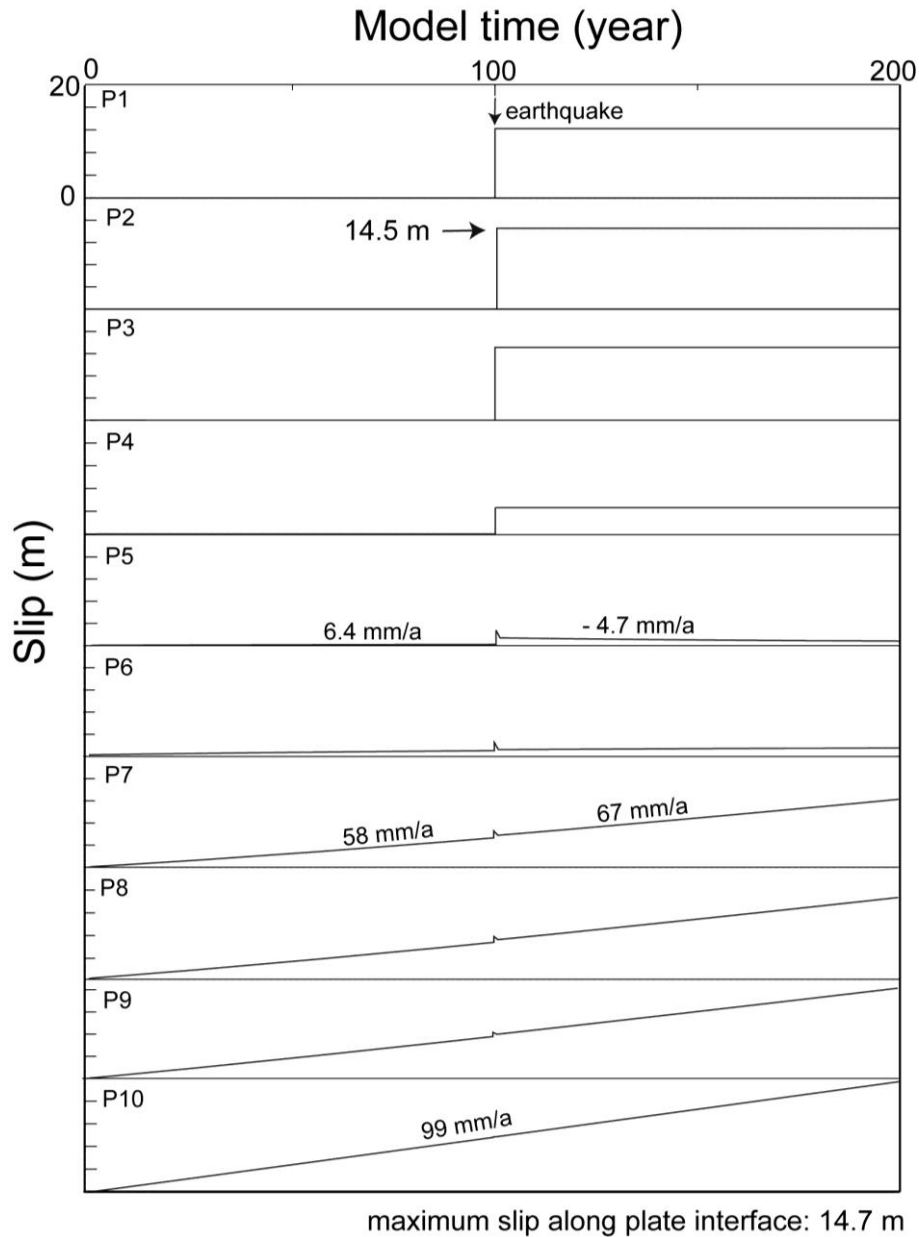

Figure 3.4 Simulated slip histories at ten points on the plate interface of the reference model (REF) within one earthquake cycle. Model settings as well as the positions of the observation points are shown in Fig. 3.2. Among all points, maximum model slip is 14.5 m at point P2. Slip rates before and after the earthquake are calculated at point P5, P7 and P10, respectively.

Changes in friction coefficient of the seismogenic zone

In the subsequent models, the effects of a variable friction coefficient µ on the deformation of the forearc as well as the slip behaviours of the plate interface were investigated. µ = 0.1 (reference model), 0.2 and 0.3 were examined for the coseismic phase, respectively, whereas in pre- and interseismic phase, the seismogenic zone is locked. Note that in this experiment, the length and depth of the seismogenic zone remain unchanged as in the reference model (Fig. 3.2). The modelling results are summarized and shown in Figs. 3.5-8.

42

As shown in Fig. 3.5a-d, preseismic displacements at the forearc surface as well as along the plate interface are very similar among the three models, which is due to the duplications of the same initial model setup (see details in Chap. 3.2.1). In general, subsidence dominates in the area starting from the trench till until the transition zone. The minimum occurs at the submarine forearc above the downdip limit of the seismogenic zone (Fig. 3.5a). Uplift of ~0.1 m occurs during the preseismic phase, whereas stronger uplift occurs
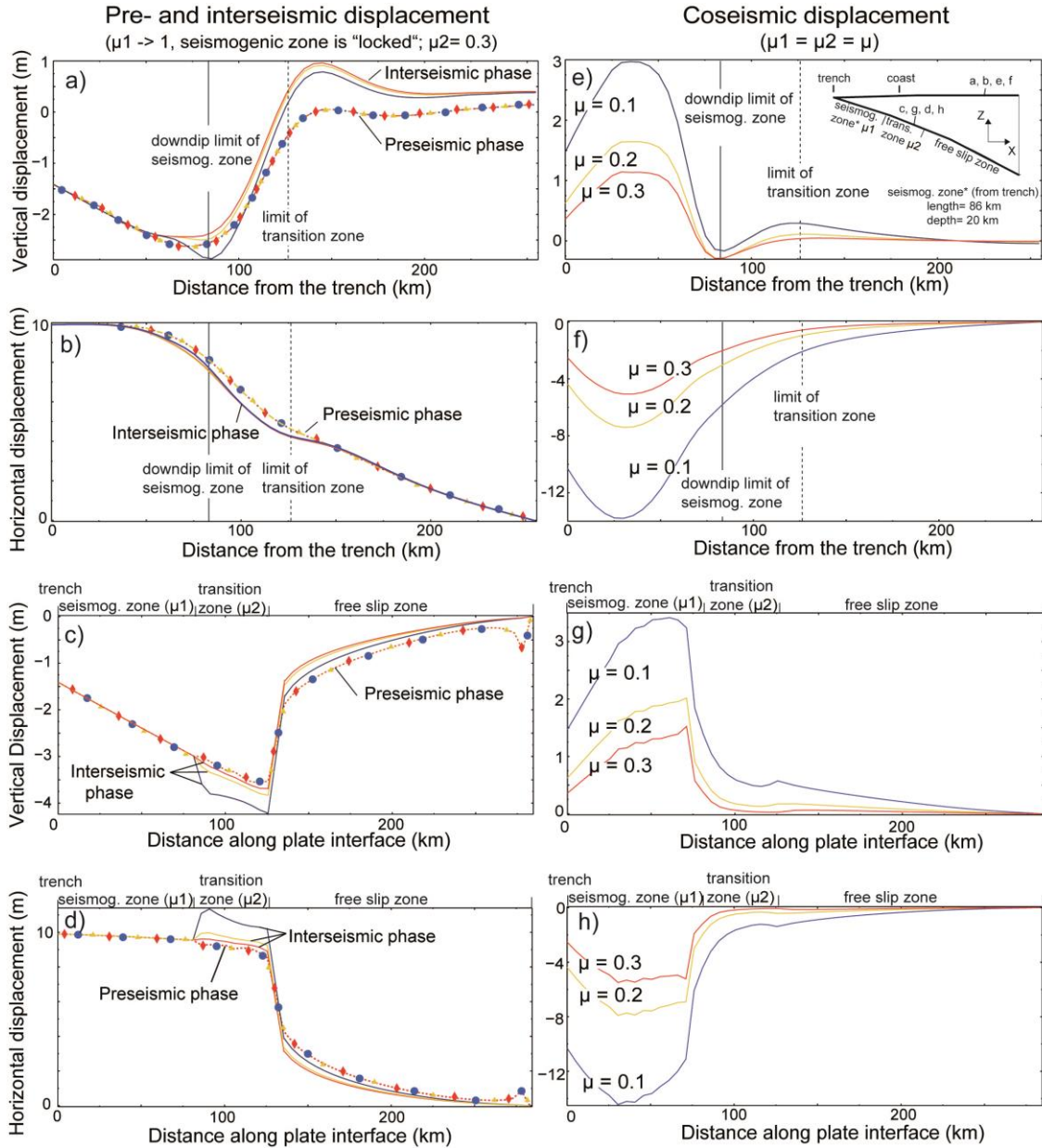
Figure 3.5 Pre- and interseismic displacements (left) and coseismic displacements (right) on the forearc surface (a, b, e and f) and plate interface (c, d, g and h) from models with different friction coefficient at the seismogenic zone. The positions of the present profiles in this figure are highlighted in the sketch at the right upper corner; the length and depth of the seismogenic zone for this experiment are also given. Limits of the seismogenic zone and transition zone projected on the forearc surface are indicated with black solid and dotted lines, respectively. Boundaries of the seismogenic zone, transition zone and free-slip zone at the plate interface are indicated above the x-axis. Coseismic displacements are shown in the right column, in which yellow, red and blue lines represent the results from friction coefficient μ = 0.1 (reference model), 0.2 and 0.3, respectively; accordingly, the pre- and interseismic displacements of these models are shown with the same colours in the left column. Preseismic displacements are additionally indicated with symbols "▲", "♦" and "●", respectively.

in the interseismic phase and reaches its maximum value of ~0.8 m (in case of μ = 0.1) at ~150 km from the trench. Furthermore, a larger friction coefficient, e.g. by μ = 0.3, results in smaller interseismic subsidence seaward but larger interseismic uplift landward of the coast. The resulting difference in subsidence displacement between μ = 0.1 and 0.3 is ~0.5 m. Landward horizontal movements dominate and are strongest close to the trench. Their rates correspond to the assigned subducting rate (100 m/a) (Fig. 3.5b). Along the plate interface (Fig. 3.5c, d), except for the similarities in both the vertical and horizontal displacement patterns of the pre- and interseismic phases, the impact of different friction coefficients in coseismic phase is more pronounced in the interseismic phase. Moreover, in between the transition zone, interseismic displacements are generally larger than in preseismic phase and increase with decreasing friction. In the coseismic phase, as slipping is allowed in the seismogenic zone, the coseismic displacement as well as the stress field and slip behaviour of the plate interface varies with different friction coefficients (Fig. 3.5e-h and Figs. 3.6-7).
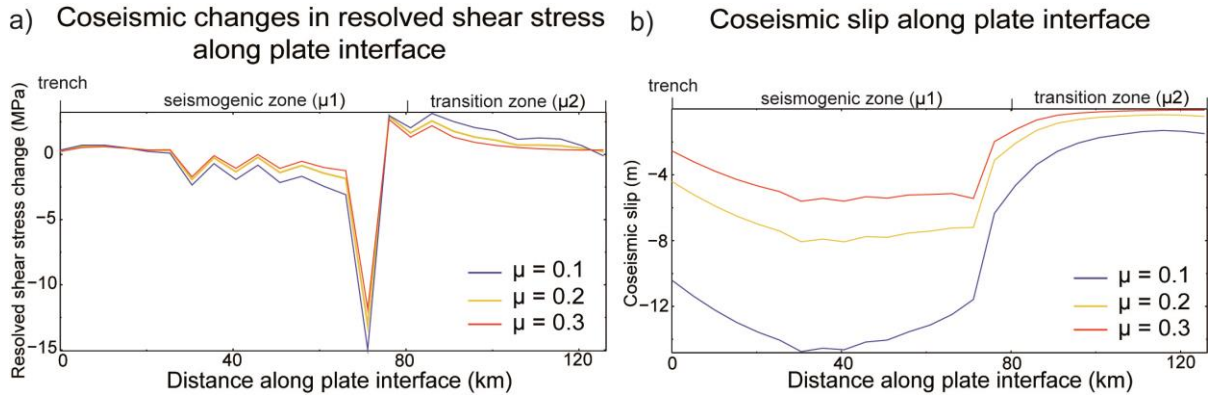

Figure 3.6 a) Coseismic changes in resolved shear stress and b) slip of the seismogenic zone and transition zone along the plate interface with friction coefficient of 0.1, 0.2 and 0.3. Boundaries of the seismogenic zone and transition zone are indicated above the x-axis.

As shown in Fig. 3.5e-h, strong coseismic uplift as well as seaward horizontal movement occurs at the forearc surface above the seismogenic zone. Similar trend of displacements is observed along the plate interface. Coseismic displacement is strongest at the shallower depth of the plate interface. At the forearc surface above the downdip limit of the seismogenic zone, subsidence occurs, whereas moderate uplift appears toward the limit of the transition zone (Fig. 3.5e). In general, the magnitudes of coseismic displacements are strongly influenced by the friction coefficient: lower friction results in stronger coseismic displacement, e.g. the differences between μ = 0.1 and μ = 0.3 in coseismic uplift and seaward horizontal movement reach up to 2 m and 8 m, respectively (Fig. 3.5g, h). With respect to the coseismic changes in resolved shear stress and slip, Fig. 3.6 illustrates that the resolved shear stress drops along the plate interface are strongest closed to the boundary between seismogenic and transition zones. The maximum shear-stress drop reaches -15 MPa for μ = 0.1 and is ~-3 MPa higher than μ = 0.3 (Fig. 3.6a). Nevertheless, the largest slip does not occur at the location where stress drop is highest but at ~30 km landward to the trench within the seismogenic zone (Fig. 3.6b), which is the same in all three models. The corresponding shear stress drop at this position of each model is similar, which is only ~-3.5 MPa (Fig. 3.6a). Lower friction results in larger

coseismic slip in both seismogenic and transition zone, and the difference reaches up to 8.5 m between $\mu = 0.1$ and 0.3.
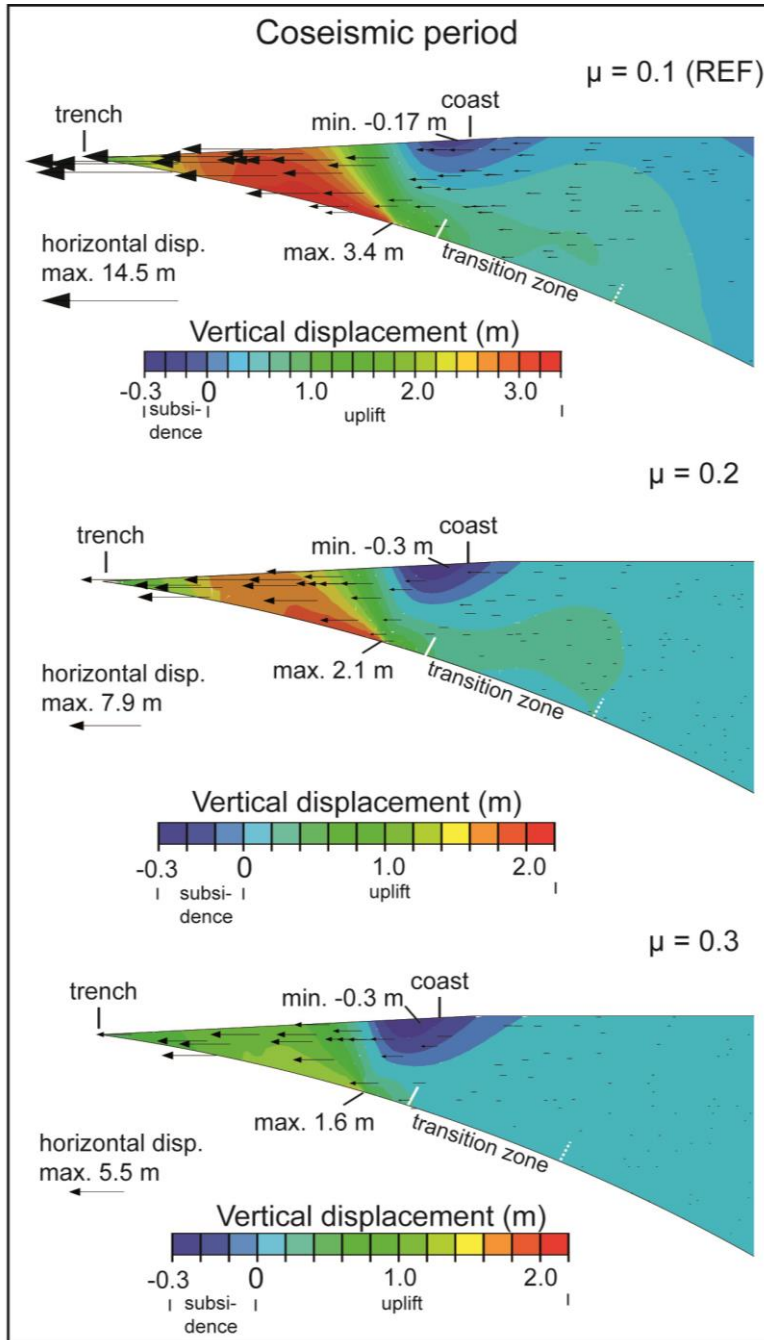

Figure 3.7 Cross sections of the overriding plate showing coseismic displacements with friction coefficient $\mu = 0.1$, 0.2 and 0.3 at the seismogenic zone. Arrows indicate directions and magnitudes of the coseismic horizontal displacements, of which the maximum values for corresponding friction coefficient are given, respectively. Note the distribution of arrows is directly extracted from Abaqus 6.12. Maximum and minimum vertical displacements are indicated directly on the cross sections. Boundaries separating the seismogenic, transition and free slip zones along the plate interface are indicated with white short lines. Note that the length of each seismogenic zone is the same as to the reference model REF.

Coseismic displacement field of forearc is also shown as cross-sections for $\mu = 0.1$, 0.2 and 0.3, respectively (Fig. 3.7). Uplift dominates the submarine forearc but is strongest in area adjacent to the lower segment of the seismogenic zone. Maximum uplift decreases as μ

increases from 0.1 to 0.3. Subsidence is strongest at the coast and above the downdip limit of the seismogenic zone, which corresponds with the results shown by surface profiles in Fig. 3.5e. The maximum seaward movement coincidences with the area of strongest uplift and displacements decrease landwards. An increase in friction lowers the magnitude of the maximum horizontal movements (Fig. 3.7).

The resulting slip histories of selected observation points from variable friction are summarized in Fig. 3.8. The resulting slip patterns at individual points are similar to the reference model (see also Fig. 3.4 and text). However, an increase in friction coefficient results in a decrease in maximum coseismic slip, which is similar to the resulting change in coseismic displacement (Fig. 3.5g, h). Moreover, the tendency of changing in slip direction at P5, which is clearly indicated in the reference model (μ = 0.1), reduces as the friction coefficient increases. In our models, the slip rate at P10 was barely influenced during the whole model time.
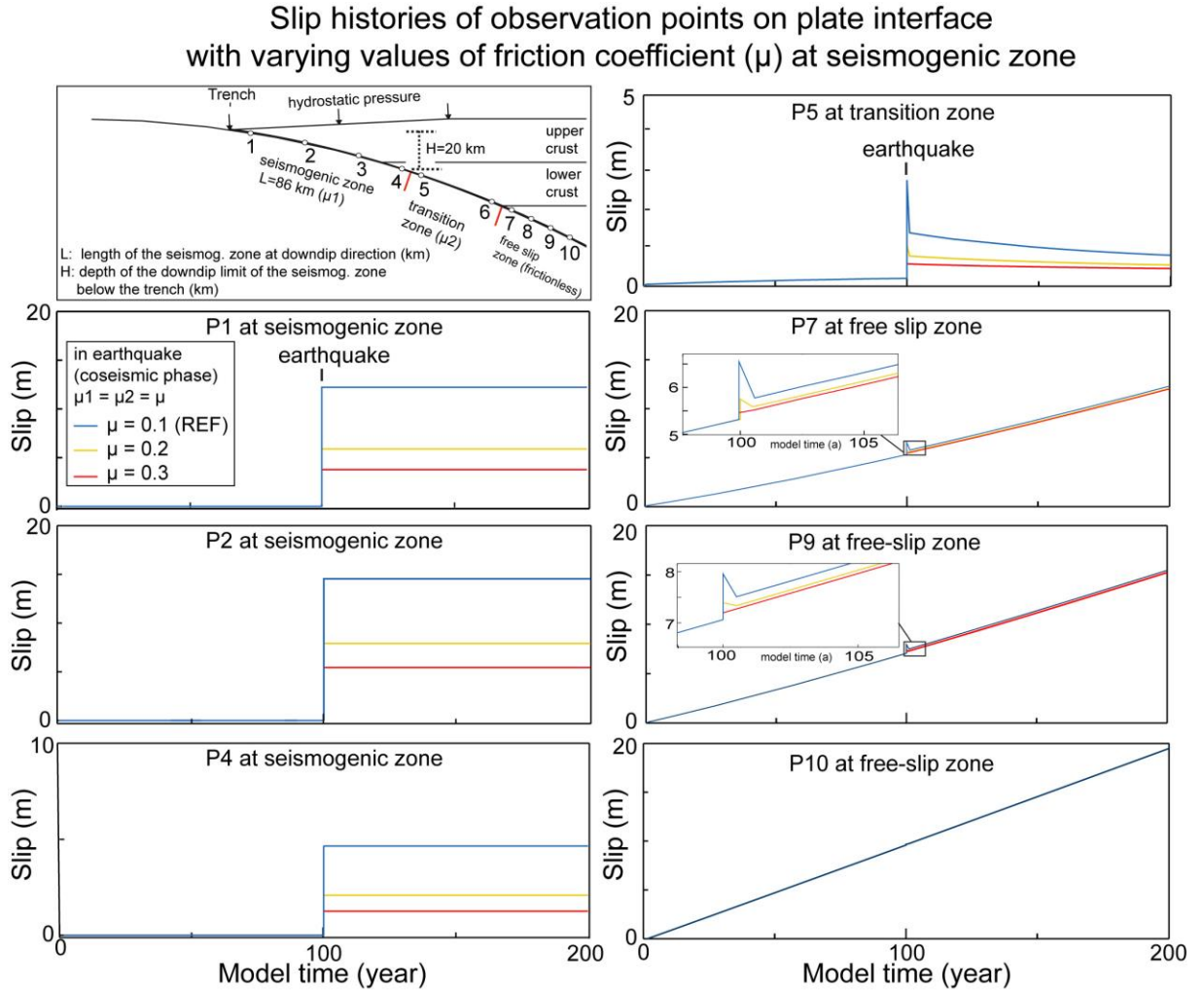

Figure 3.8 Simulated slip histories at selected points of the plate interface within one seismic cycle. Blue, yellow and red lines indicate results of friction coefficient μ = 0.1, 0.2 and 0.3, respectively. Locations of the observation points are shown in the left upper corner as well as indicated in each graph. Perturbation on fault slip rate by the earthquake varies at different segment of the plate interface and reduces with increasing depth, where the slip rate of point 10 (P10) is barely influenced.

Changes in downdip limit of the seismogenic zone

In subsequent models, modifications on the models were carried out with variable length and depth of the downdip limit of the seismogenic zone (Fig. 3.9). A 2-D model with a deep (86 km in length, see Fig. 3.9, same as in the following models) seismogenic zone - the reference model (see also Fig. 3.2), intermediate (52 km) and shallow (26 km) model seismogenic zone has been examined, respectively. The boundary of the transition zone and free-slip zone remains unchanged. The results are shown in Figs. 3.10-13.
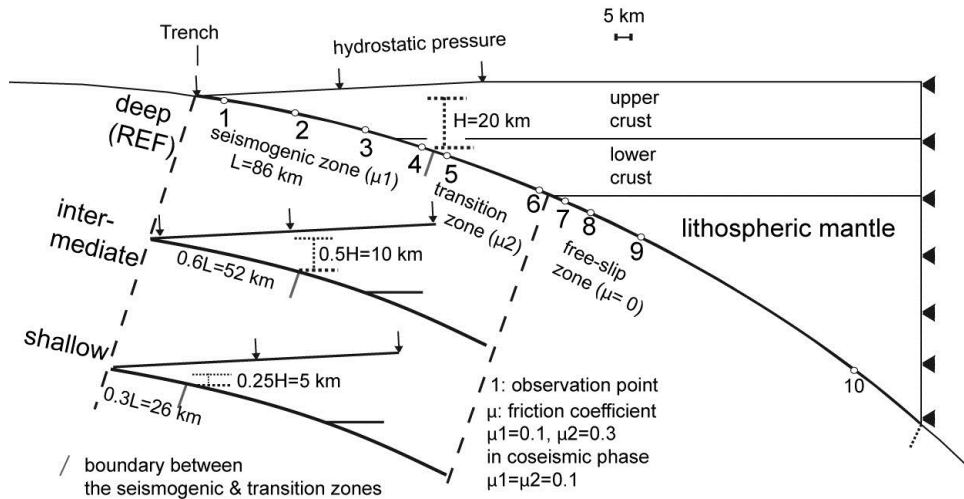

Figure 3.9 Model settings for experiments with varying downdip limit of the seismogenic zone. Positions of the downdip limit are indicated by "deep", "intermediate" and "shallow" seismogenic zone, of which the corresponding length (L) and depth (H) of seismogenic zone are given. Positions of the observation points are the same as in the reference model REF.

Fig. 3.10 summarizes the pre-, co- and interseismic displacements with respect to different length and depth of the seismogenic zones. Preseismic and interseismic displacements are shown as total displacements, which comprise both vertical and horizontal displacements. During the preseismic phase (Fig. 3.10a), the total displacement at the seismogenic zone reaches ~10 m in 100 a in each model, which accommodates the assigned subducting rate of 100 mm/a. Strong displacement occurs mainly at the forearc above the seismogenic zone and the area varies according to the given length of the seismogenic zone; it also occurs at the lower segment of the transition zone. In coseismic phase (Fig. 3.10b), strong coseismic uplift occurs above the seismogenic zone. A deep seismogenic zone results in coseismic uplift up to ~3.3 m close to the downdip limit, whereas the maximum uplift in the shallow seismogenic zone reaches ~2.7 m. The magnitude of coseismic uplift reduces both seawards and landwards. The coseismic horizontal displacement is dominated by seaward movement; strong displacement occurs accompanied by strong uplift. The largest seaward horizontal displacement is shown in the shallow coseismic zone. The pattern of the total displacement in preseismic and interseismic phases is similar (Fig. 3.10a, b), though the magnitude of interseismic displacement is higher. For example, the magnitude of interseismic displacement of the shallow seismogenic zone is almost twice higher than in the preseismic phase.
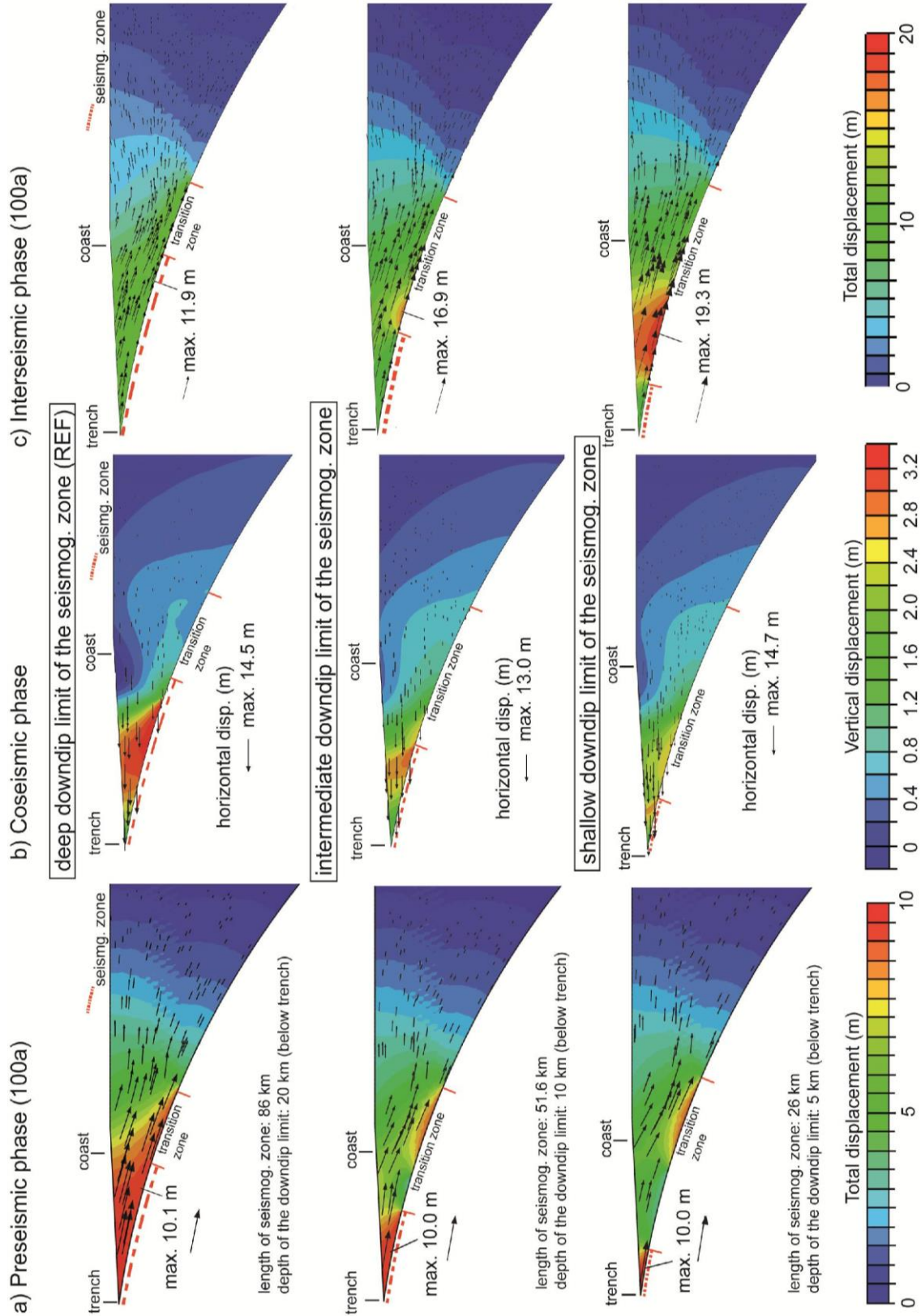
Figure 3.10 Cross sections of the overriding plate showing a) pre-, b) co- and c) interseismic displacements with varying depth of downdip limit of the seismogenic zone, which are shown in the upper, middle and lower row, respectively. Arrows in a) and c) indicate direction and magnitude of the total displacement in the pre- and interseismic phases, respectively, of which maximum values are given, whereas arrows in b) indicate coseismic horizontal displacements. Note the density of the arrows is slightly modified based on the exporting files from Abaqus 6.12. Boundaries separating the seismogenic, transition and free slip zones along the plate interface are indicated with red short lines.

Displacements are shown in Fig. 3.11 with two profiles along the forearc surface as well as along the plate interface, respectively. In the cases of the intermediate and shallow seismogenic zone, quasi-symmetric patterns of pre- and interseismic subsidence are shown from the trench to the end of transition zone, where both patterns are similar in the reference model (Fig. 3.11a). The plate interface behaves similarly, except for the segment of the deep seismogenic zone between ~80 km and the end of transition zone (Fig. 3.11c). Similar
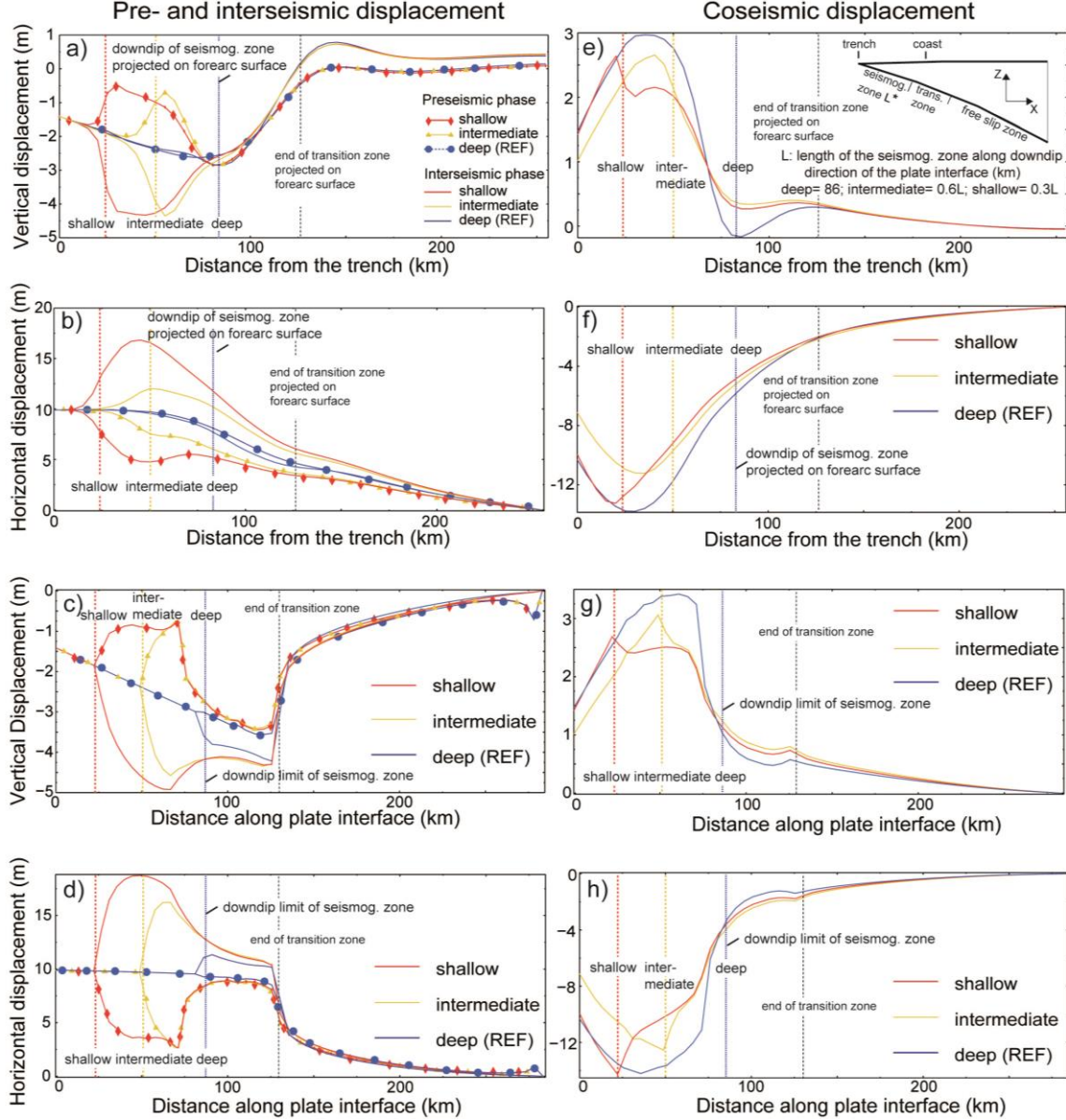

Figure 3.11 Pre- and interseismic displacements (left column) and coseismic displacements (right column) on the forearc surface (a, b, e and f) and plate interface (c, d, g and h) from models with varying downdip limits of the seismogenic zone. The downdip limits of the shallow, intermediate and deep seismogenic zones projected on the forearc surface as well as along the plate interface are indicated with red, yellow and blue vertical broken lines, respectively; the end of transition zone is indicated with black broken line. The corresponding length (L) and depth (H) of each examined seismogenic zone are given in the sketch at the right upper corner. Red, yellow and blue curves represent the results for the shallow, intermediate and deep seismogenic zone, respectively; preseismic displacements are additionally indicated with symbols "▲", "♦" and "●".

phenomenon can be seen also in horizontal displacement (Fig. 3.11b, d), i.e. horizontal displacements are relatively higher in interseismic phase than preseismic phase (see also Fig.

3.10). Moreover, it is also shown that the peak of subsidence, both on forearc surface and plate interface, corresponds with the position of the downdip limit of the seismogenic zone, in particular for the shallow and intermediate cases.

Similarly, in the coseismic phase (Fig. 3.11e, f), the peak of uplift as well as seaward movement also corresponds with the downdip limit of the intermediate and shallow seismogenic zone; whereas the peak still occurs at the shallower segment of the deep one. Interestingly, coseismic subsidence only occurs at the forearc surface in the reference model (Fig. 3.11e).

Resolved shear stress drops along the plate interface in three models are all highest at ~70 km landward to the trench (Fig. 3.12a). The magnitude is the highest in the reference model. Independent to the stress drop, coseismic slip occurs generally at the shallower depth of the seismogenic zone, in which the maximum slip coincides with the downdip limit of the shallow and intermediate seismogenic zone but is preferable to occur in the shallower segment of the deep seismogenic zone (Fig. 3.12b).
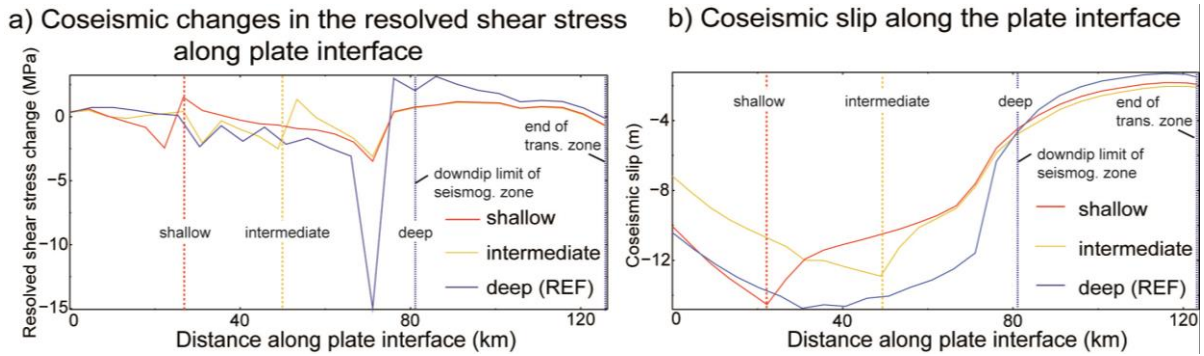

Figure 3.12 Coseismic changes in a) resolved shear stress and b) slip of the seismogenic and transition zones along the plate interface. The profiles all begin from the trench and the location of the variable downdip limit of the seismogenic zone is indicated with red, yellow and deep broken line for the shallow, intermediate and deep seismogenic zone, respectively. Note the landward limit of the transition zone is fixed but its seaward limit varies according to the downdip limit of the seismogenic zone.

The slip histories of selected observation points along the plate interface are summarized in Fig. 3.13. Note that the positions of the observation points do not vary with the length of the seismogenic zone. Largest coseismic slip occurs in the shallower segment of the seismogenic zone and decreases in both updip and downdip direction (see Fig. 3.13, P1-P4 in "deep" and P1-P2 in "intermediate"). The steady slip rates of P5 and P6 in transition zones indicate mainly two types of variations. The steady preseismic slip is terminated as the earthquake occurs and followed by the interseismic slip rate; however, the segment in the vicinity of P5, which is within the lower crust, experiences changes in slip direction (see also Fig 3.4 and text). Furthermore, it is shown that the tendency of changing slip direction reduces as P5 locates farther away from the downdip limit of the seismogenic zone. However, this phenomenon is not shown at P6 instead of that decrease in slip rate occurs after the earthquake. In contrast, the steady slip rate of P7 and P9 in free-slip zone increases after the earthquake, but point P10 is barely affected.

Slip histories at observation points along the plate interface with varying downdip limit of the seismogenic zone

H: depth of the downdip limit
   below the trench (km)
L: extention of the downdip limit
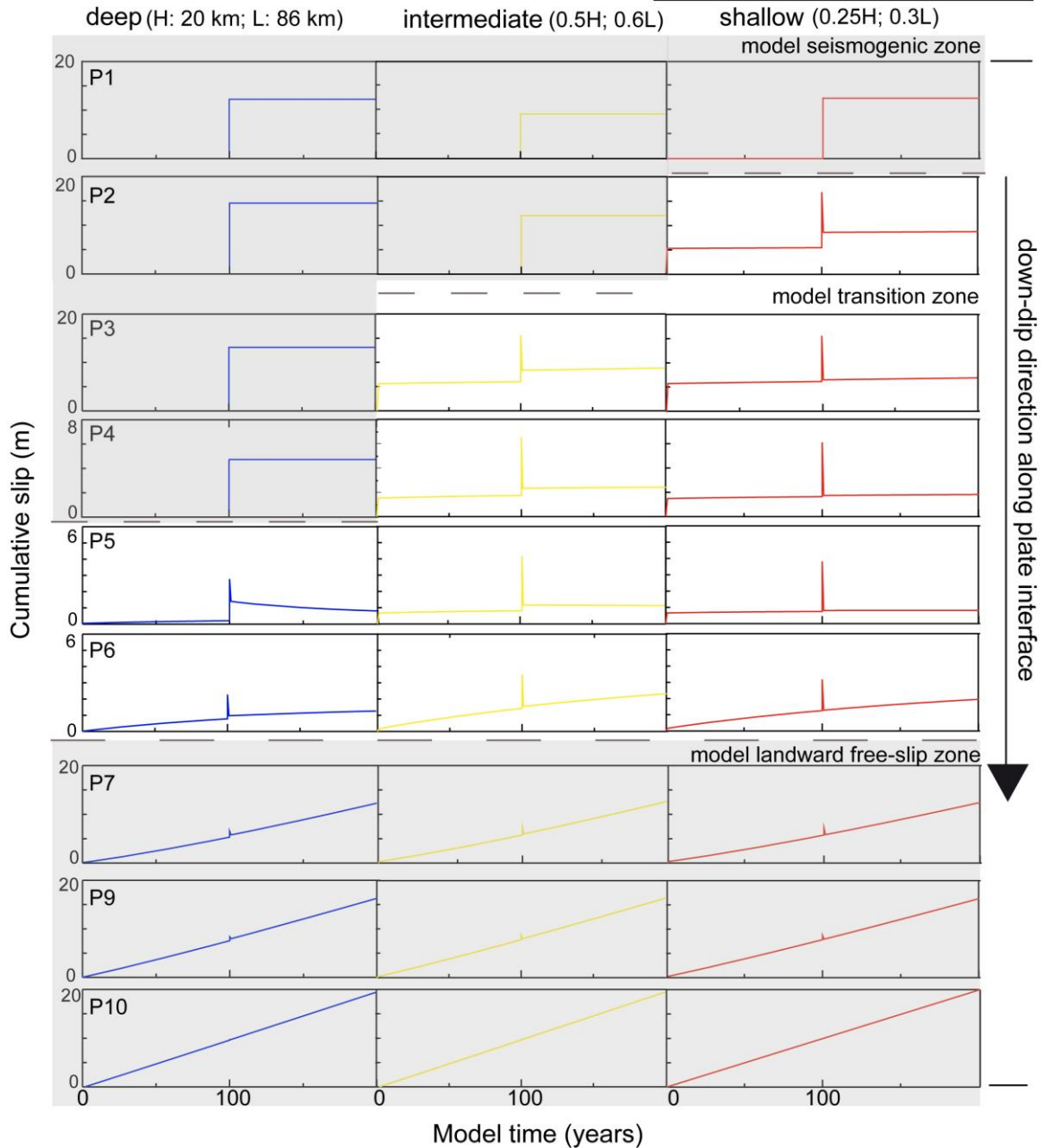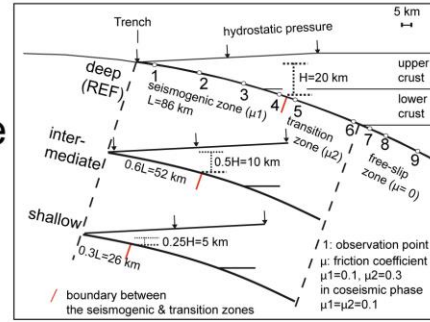   from the trench along the plate interface (km)

Figure 3.13 Summary of simulated slip histories at selected points of the plate interface within one seismic cycle. Locations of the observation points are fixed and are shown in the right upper corner (see Fig. 3.9 for location of P10). Blue, yellow and red lines indicate results of models with a deep, intermediate and shallow seismogenic zone, respectively; the results of each individual model are shown in column. Length and depth of each seismogenic zone are indicated. The boundaries of the model seismogenic zone, transition zone and free-slip zones along the plate interface are indicated with shaded background as well as black broken lines.

3.3.2 3-D model results

As discussed in Chap. 3.1 and 3.2, the present 2-D models were extended to three dimensions, i.e. trench-parallel component of a subduction zone is included. The model setup of the 3-D model is shown in Fig. 3.3. In subsequent models, the impacts of variations in the friction coefficient as well as the downdip limit of seismogenic zone on forearc deformation and the slip history were investigated. Results of individual experiments and comparisons with the reference model (REF-3D) are shown in Figs. 3.14-20.

Changes in friction coefficient of the seismogenic zone

Three values of the friction coefficient μ (0.1, 0.2 and 0.3) were examined with the same geometry of the seismogenic zone. Similar to the 2-D modelling approach, the above values of friction coefficient are only applied in coseismic phase of the individual model.

The model results are shown along two profiles along the middle of the forearc surface and plate interface are drawn for observations (Fig. 3.14). As shown in Fig. 3.14a, preseismic and interseismic vertical displacements on the forearc surface are similar from the trench until ~75 km landward, however, interseismic vertical motions become stronger closer to the downdip margin of seismogenic zone. Here, no significant changes on both vertical and horizontal displacements are observed when applying different friction coefficient (Figs. 3.14a, 3.15). Nevertheless, changing friction coefficient causes significant variations on coseismic displacements and slip rate (Figs. 3.14b, 3.15). Coseismic subsidence and uplift occurs on the forearc surface with increasing wavelength and magnitude from the trench to ~70 km landward (Fig. 3.14b). Maximum uplift occurs at ~50 km landward to trench and reaches ~1.5 m, 0.8 m and 0.6 m for friction coefficient of 0.1, 0.2 and 0.3, respectively. Subsidence is strongest for $\mu = 0.1$, for which it reaches up to ~-0.9 m and it is followed by another sequence of moderate uplift and subsidence to the end of transition zone. Patterns of coseismic uplift and subsidence are similar in all models, while the magnitude of displacement decreases with increasing friction. A similar tendency is also seen in the coseismic slip along the plate interface (Fig. 3.14c) as well as in the coseismic horizontal displacement at the forearc surface (Fig. 3.15).

The coseismic deformation shown in cross-section view in Fig. 3.16 confirms again the previous observation, i.e. the deformation patterns are similar, regardless of the value of friction coefficient, but the magnitude of displacement reduces with increasing friction. Displacements in similar magnitude but in opposite directions are shown at the lower segment of the seismogenic zone, i.e. a small region of subsidence accompanied with landward movement, which is located between two regions of uplift plus seaward movement (Fig. 3.16). It is also shown that this subsidence as well as landward movement is strongest close to the interface but reduces upwards. Results shown in Fig. 3.14a and Fig. 3.15 indicate the patterns of both pre- and interseismic surface deformation in this experiment are similar, therefore only results of coseismic deformation are demonstrated in cross-section view.

a) **Pre- and interseismic vertical displacement of the forearc surface A-A´ (3D)**

in pre- & interseismic phase, seismog. zone "locked", µ2= 0.3

Interseismic phase

coast

trench A

A´

B

seismogenic zone

downdip limit of the seismogenic zone (projected on AA') "locked"

downdip limit of transition zone (projected on AA')

Preseismic phase

Vertical displacement (m)

Distance from the trench (km)

b) **Coseismic vertical displacement of the forearc surface A-A´ (3D)**

µ = 0.1 (REF-3D)
µ = 0.2
µ = 0.3

in coseismic phase, µ1 = µ, µ2 remains 0.3

downdip limit of transition zone (projected on AA')

downdip limit of the seismogenic zone (projected on AA')

Vertical displacement (m)

Distance from the trench (km)

c) **Coseismic slip of the plate interface A-B (3D)**

µ = 0.1 (REF-3D)
µ = 0.2
µ = 0.3

in coseismic phase, µ1 = µ, µ2 remains 0.3

downdip limit of the seismogenic zone (length = 89.8 km)

downdip limit of transition zone

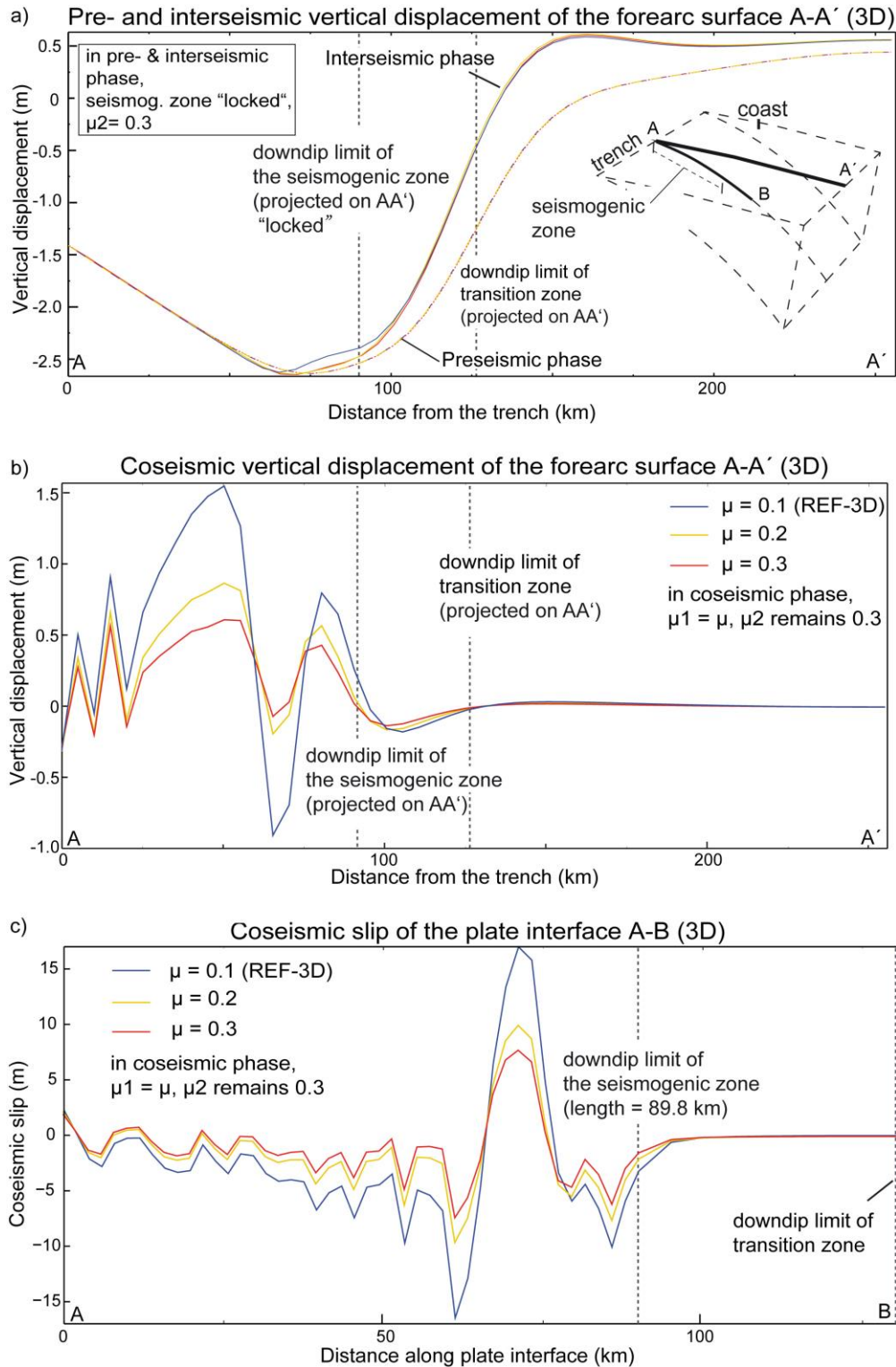Coseismic slip (m)

Distance along plate interface (km)

Figure 3.14 a) Pre- and interseismic and b) coseismic vertical displacements of the forearc surface, and c) coseismic slip of the selected profile on plate interface from models with different friction coefficient µ at seismogenic zone. The positions of the present profiles in this figure are highlighted in the sketch at the upper right corner. Limits of the seismogenic zone and transition zone projected on the forearc surface as well as on the plate interface are indicated with black and grey broken straight lines, respectively. Values of friction coefficient in each phase are given in the figures. Blue, yellow and red lines represent the results from µ = 0.1, 0.2 and 0.3, respectively. Pre- and interseismic displacements in a) are shown with the same colour patterns for coseismic phase in b) and c), except preseismic displacements are indicated with broken lines.
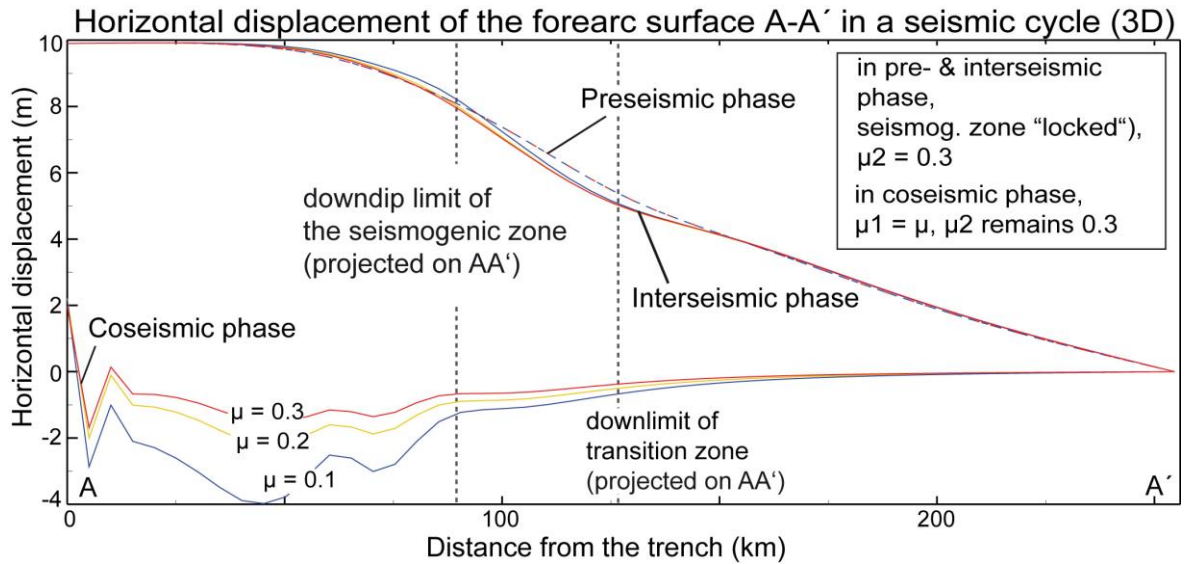
Figure 3.15 Horizontal displacements of the forearc surface with different friction coefficients. Blue, yellow and red lines represent the results for friction coefficient $\mu = 0.1$, 0.2 and 0.3, respectively. Pre- and interseismic displacements in are shown with the same colour patterns for coseismic phase, except preseismic displacements are additionally shown with broken lines.

Fig. 3.17 shows the resulting total horizontal surface displacement of the coseismic phase for different friction coefficients, in which only the trench-parallel and trench-normal components (x and y) are considered. The total surface displacement is strongest near the centre as well as the near-trench edge of the seismogenic zone, and it reaches maximum values of 4.2 m, 3.2 m and 2.7 m for friction coefficients of 0.1, 0.2 and 0.3, respectively. Seaward displacements dominate in the presented area but the surface displacement vectors diverge in the seismogenic zone; it is also shown in $\mu = 0.1$ (Fig. 3.17b) that total surface displacements spread further landwards and the divergence is also stronger, in comparison to $\mu = 0.1$, 0.2 (Fig. 3.17c, d).

Changes in downdip limit of the seismogenic zone

Experiments with variable downdip limit of the seismogenic zone were also conducted in the 3-D domain. Positions of downdip limits vary along with the lengths of seismogenic zone. Three lengths of seismogenic zone - 35.6 km ("shallow"), 53.3 km ("intermediate") and 89.9 km ("deep") - are examined in the subsequent models, in which the last one is the reference model (REF-3D). Fig. 3.18 shows the resulting surface displacement within a seismic cycle with two profiles on the forearc surface and along the plate interface, respectively. In preseismic and interseismic phases, subsidence occurs from the trench and propagates ~140 km landwards at the forearc surface, where pre- and interseismic uplifts occur (Fig. 3.18a). In the reference model, maximum values of preseismic subsidence and uplift are ~-2.5 m and ~0.3 m, respectively; and interseismic subsidence reaches also up to ~-2.5 m but the interseismic uplift reaches ~0.5 m at ~150 km landward to the trench and slightly reduces further landward. Both the pattern and magnitude of uplift from different downdip limits are similar during the preseismic and interseismic phases, respectively. However, variations in patterns of preseismic subsidence are obvious, which reflects the
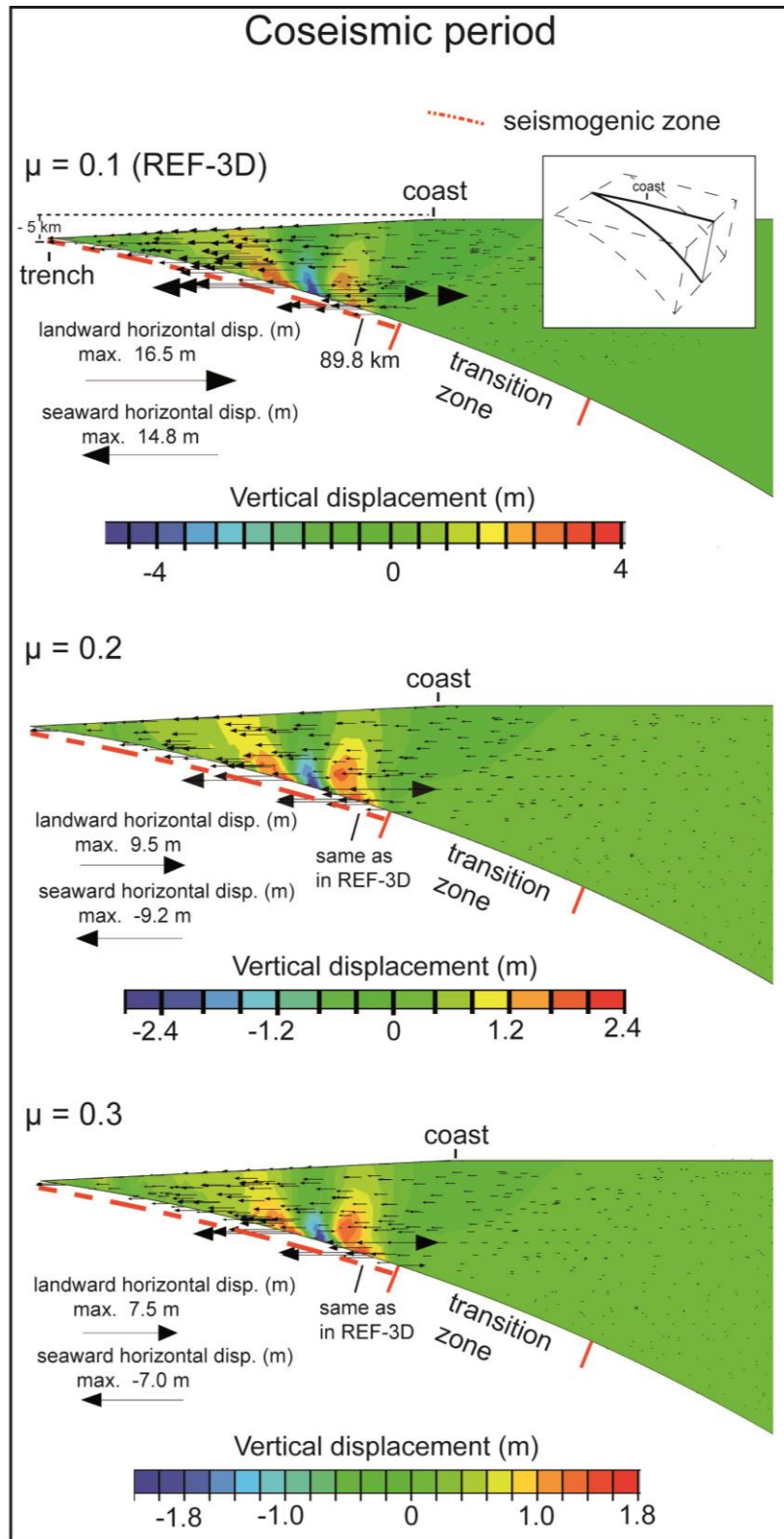
Figure 3.16 Cross-sections of the overriding plate showing coseismic vertical displacements with friction coefficient μ= 0.1, 0.2 and 0.3 at seismogenic zone. The present cross-section intercepts the middle of the overriding plate and is delineated with thick black lines in the small sketch at the right corner. Arrows indicate directions and magnitudes of the coseismic horizontal displacements, which are scaled with the maximum values for individual μ. Note the distribution of arrows is directly extracted from Abaqus 6.12. Boundaries separating the seismogenic, transition and free slip zones along the plate interface are indicated with red short lines. Note here the length of each seismogenic zone is the same as the reference model REF-3D.
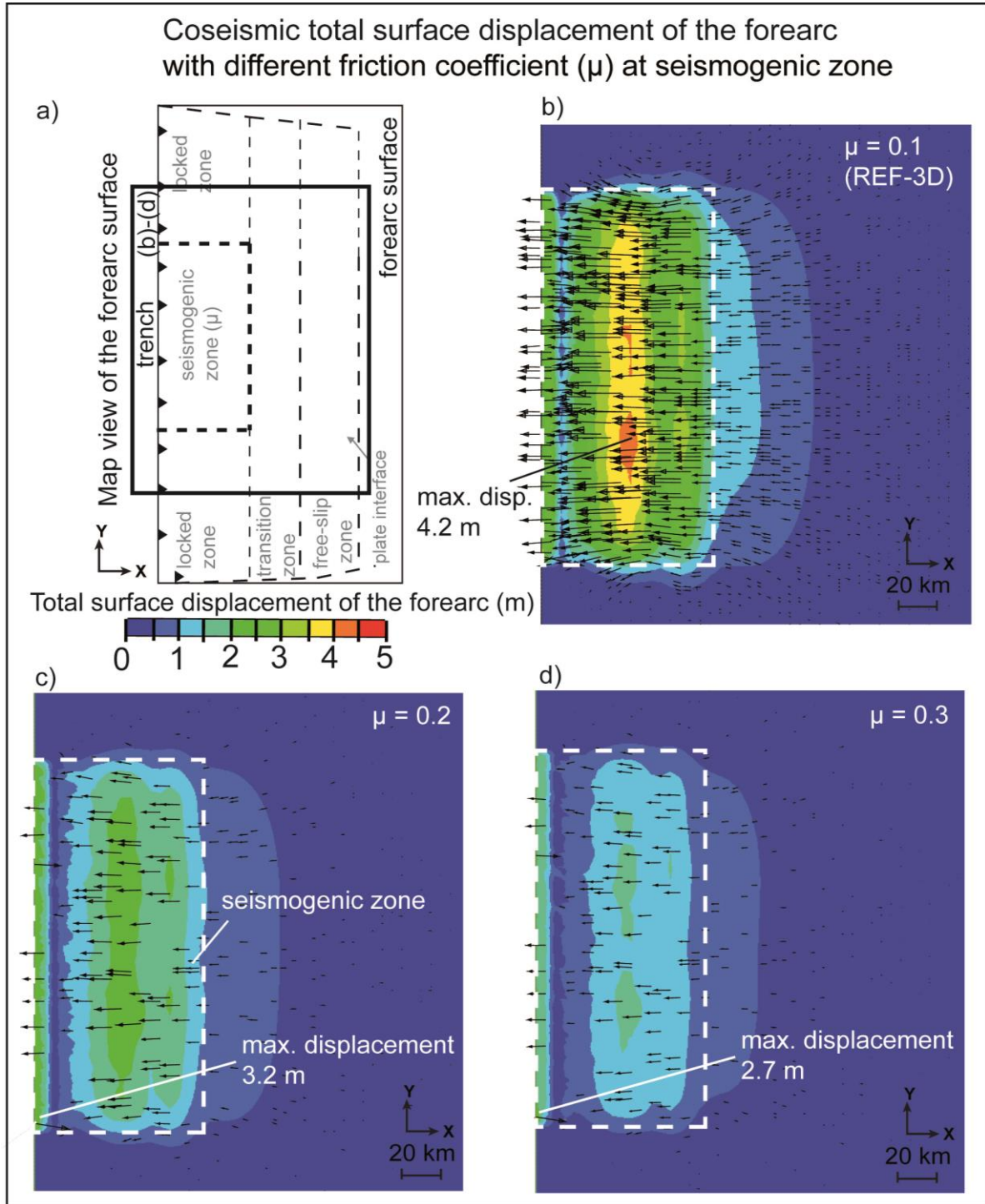
Figure 3.17 Map view of the forearc surface showing coseismic total surface displacements with friction coefficient μ = b) 0.1, c) 0.2 and d) 0.3 at seismogenic zone. a) Sketch illustrating the presented area in b)-d) on the forearc surface. Total displacement is shown by both colour coding and arrows, which denote the vectors of the coseismic motions. The observed displacement reaches maximum value of 4.2 m by μ = 0.1, and the size of the arrows in b) and c) is scaled with this value, respectively. Note the distribution of arrows is directly extracted from Abaqus 6.12. Boundaries of the seismogenic zone projected on the forearc surface are indicated with white broken lines. Note the geometry and area of the projected seismogenic zone is the same in each model.

variations in the length of seismogenic zone. In the cases of shallow and intermediate seismogenic zone, preseimic subsidence fluctuates between 35-100 km landward from the

trench.

Fig. 3.18b, c show the resulting coseismic vertical displacement of the forearc and coseismic slip along the plate interface, respectively. In the reference model, the maximum of coseismic uplift is ~1.5 m and followed by strong subsidence of up to -0.9 m (Fig. 3.18b). Another sequence of moderate uplift and subsidence (up to ~0.8 m and ~-0.2 m, respectively) occurs also in the reference model, but it is not shown in other shallower seismogenic zones. With respect to coseismic slip, the maximum slip occurs close to the downdip limit of shallow and intermediate seismogenic zone, respectively (Fig. 3.18a). Nevertheless, in the reference model, slips with similar magnitude but of opposite directions are shown in the lower segment of the (deep) seismogenic zone. This phenomenon is indicated also in the cross-section view shown in Fig. 3.19b. Coseismic horizontal movement at the forearc is dominated by the seaward movement; however, landward movement occurs in the lower segment of the deep seismogenic zone, in which coseismic subsidence also occurs and is observable in the forearc surface between two uplift patterns (see Fig. 3.18b). Moreover, it is also indicated in Fig. 3.19b-d that the spatial distributions as well as magnitudes of coseismic displacements depend on the depth of the downdip limit of the seismogenic zone (see also Fig. 3.18b), i.e. sequences of costal uplift and subsidence occur further seawards as the downdip limit is shallower. Nevertheless, no indication from opposite motions can be seen along the plate interface in the cases of shallow and intermediate downdip limits (Figs. 3.18c, 3.19c-d).

Fig. 3.20 shows the resulting total horizontal surface displacement of the forearc surface with respect to different downdip limits. The maximum value of displacement is ~10 m for both preseismic and interseismic phases and occurs in the trench-parallel region, but its landward extension decreases along with shallower downdip limit (Fig. 3.20b, left and right columns). Coseismic displacements concentrate mainly in two areas, which are separated by a narrow transition zone of little displacement within the seismogenic zone. Divergent motions are shown at the shorter edges of the seismogenic zone. The horizontal surface displacement extends further landwards in the reference model with the deepest downdip limit. Moreover, as the downdip limit of the seismogenic zone decreases, the maximum value of coseismic displacement decreases. Also, the area of coseismic displacement declines.
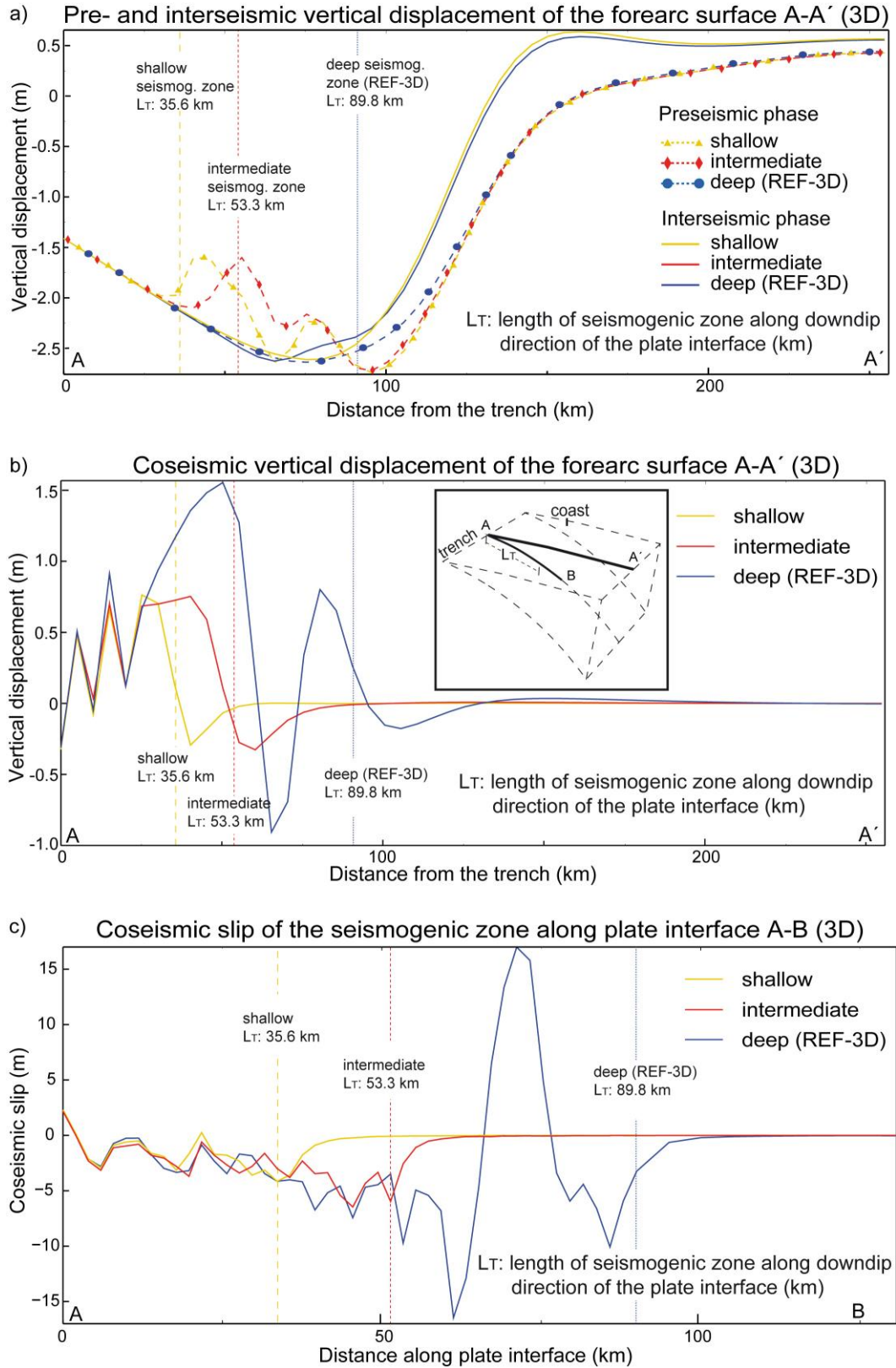
Figure 3.18 a) Pre- and interseismic and b) coseismic vertical displacements of the forearc surface, and c) coseismic slip of the selected profile on plate interface with varying length of seismogenic zone. The positions of the present profiles in this figure are highlighted in the middle sketch. Individual limits of the examined shallow, intermediate and deep seismogenic zones projected on the forearc surface as well as on the plate interface are indicated with yellow, red and blue broken straight lines, respectively. Pre- and interseismic displacements in a) are shown with the same colour patterns for coseismic phase in b) and c). Note that preseismic displacements are additionally indicated with symbols "▲", "♦" and "●", respectively.
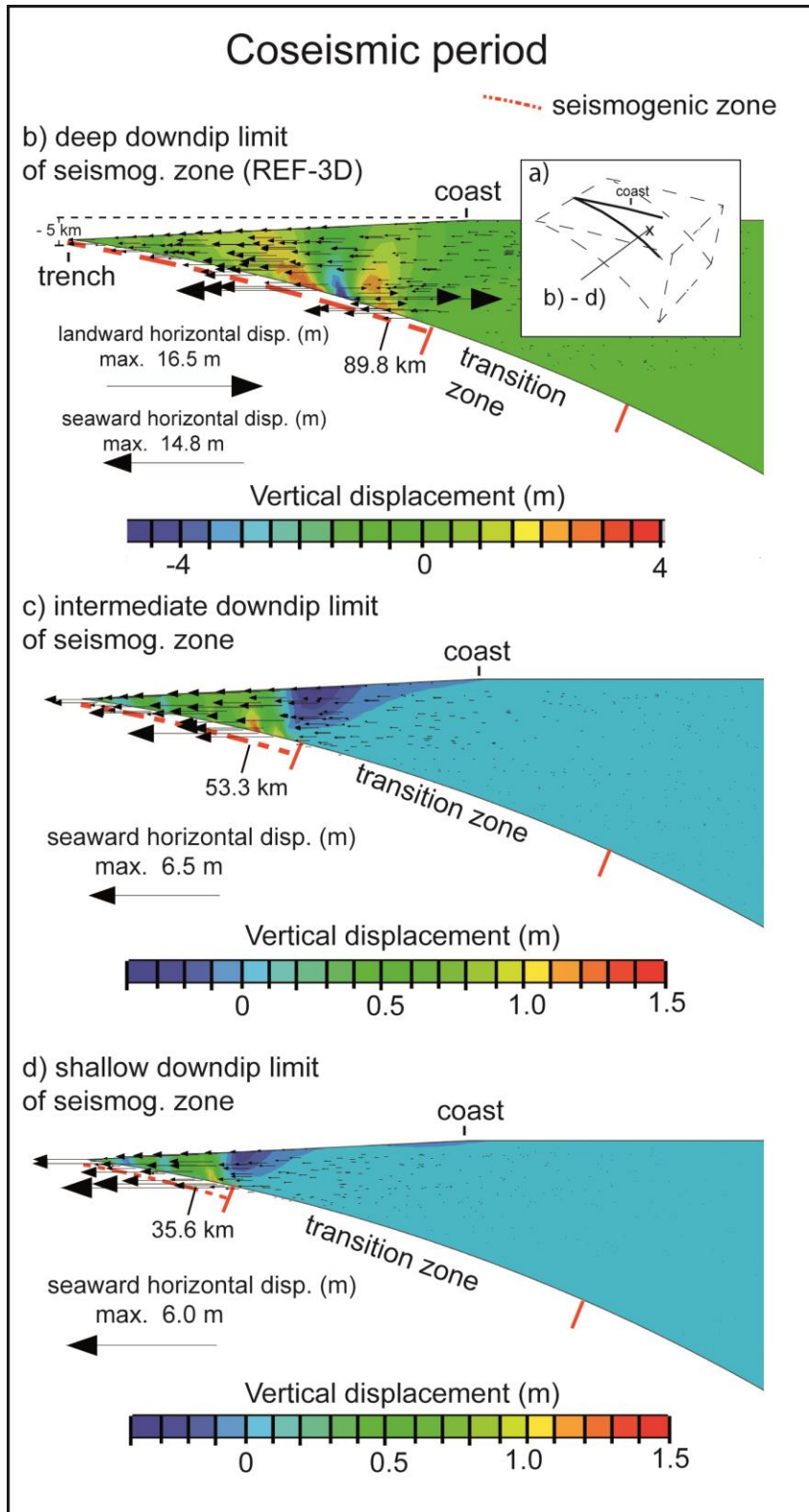
58

Figure 3.19 Cross-sections of the overriding plate showing coseismic displacements of a) deep, b) intermediate and c) shallow seismogenic zone, respectively. a) Sketch illustrating the position of the presented cross-section in b)-d). Colour codes indicate vertical displacements; arrows indicate both directions and magnitudes of the coseismic horizontal displacements, respectively. Note the distribution of arrows is directly extracted from Abaqus 6.12. Boundaries separating the seismogenic, transition and free slip zones along the plate interface are indicated by red short lines. Length of each examined seismogenic zone is given.
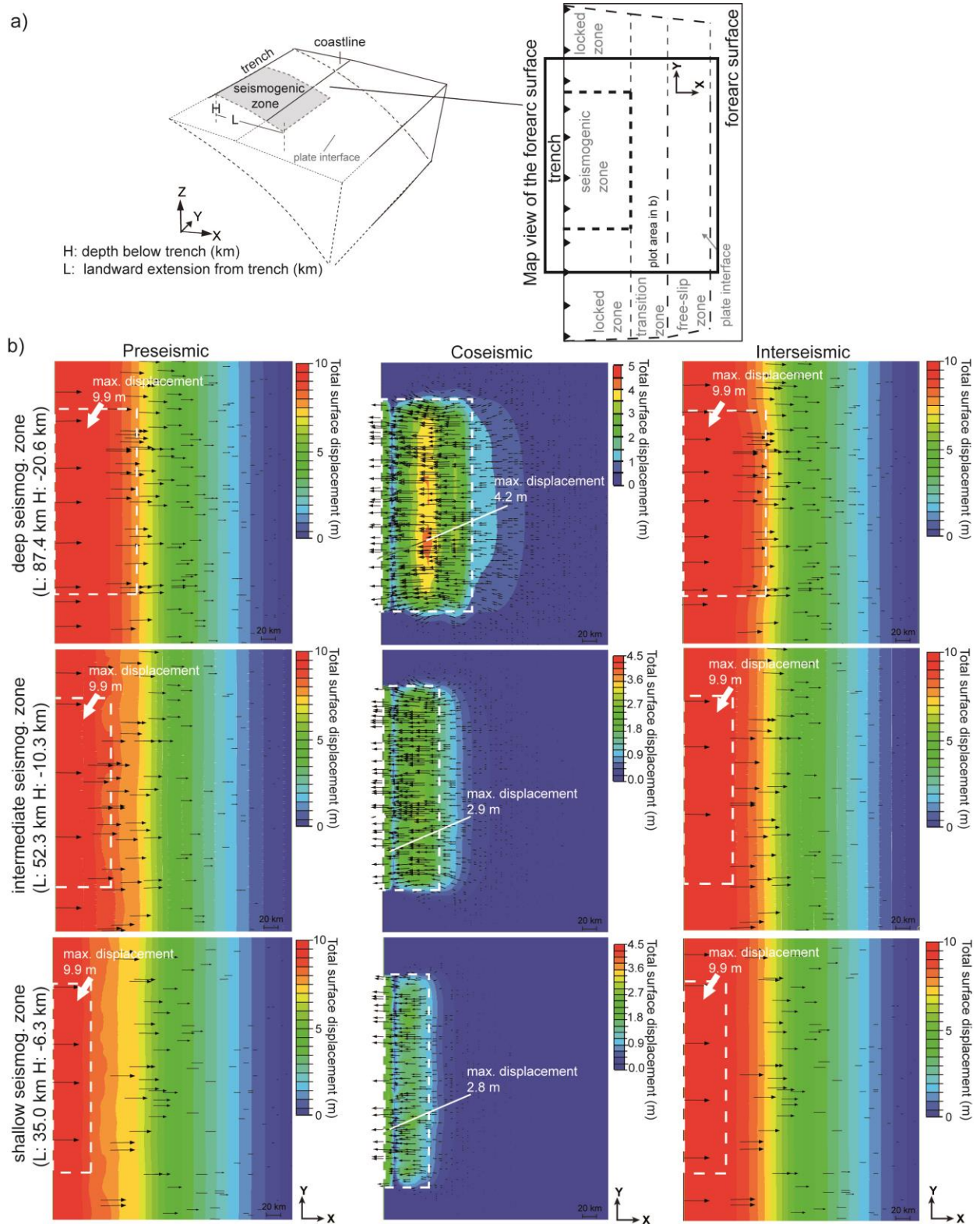
Figure 3.20 a) Map view of the presented area of the forearc surface in b): pre-, co- and interseismic total horizontal surface displacements (in columns) of a deep, intermediate and shallow seismogenic zone (in rows). Total horizontal displacement is shown by both colour coding and black arrows. Note the illustration of these arrows is directly extracted from Abaqus 6.12. Values of maximum displacements are given on each graph, which are indicated by white arrows pointing to the relevant area. Boundaries of the examined seismogenic zone projected on the forearc surface are indicated with white broken lines.

3.3.3 Comparisons between 2-D and 3-D subduction earthquake-cycle modelling

In this section, results from the 2-D and 3-D reference models are compared with profiles along the plate interface and through the forearc surface, which are also shown individually in Chap. 3.3.1 and 3.3.2, respectively. As complementary for the comparisons, selected results in trench-parallel direction extracted from the 3-D models are also shown (Fig. 3.21e, f).

As shown in Fig. 3.21a, vertical displacements predicted by 2-D and 3-D models start to differentiate at ~75 km from the trench. Preseismic uplift is more obvious at ~150 km of the 2-D than the 3-D profile, of which a clearer convex pattern can be seen from the 2-D model in landward direction but a more homogenous uplift pattern from the 3-D model. Similar patterns are observed in the interseismic phase, except now the uplift has been enhanced stronger in the 2-D model than in 3-D model. Patterns of pre- and interseismic horizontal displacement are similar and different slightly in magnitudes between the 2-D and 3-D model (Fig. 3.21b). More notable differences are shown in coseismic displacements. The maximum magnitude of coseismic uplift and seaward horizontal movements are ~1 m and ~8 m stronger in the 2-D than in the 3-D model, respectively. Fluctuations occur at the forearc surface of the 3-D model including a stronger coseismic subsidence than the 2-D model (Fig. 3.21c). The magnitude of coseismic horizontal displacement is remarkably lower in the forearc surface of the 3-D model, where slight uplift occurs behind the trench; also, the pattern is more heterogeneous than the 2-D case (Fig. 3.21d).

In addition, displacements parallel to the strike of the trench are shown as profiles at different distances from the trench (Fig. 3.21e). It is shown that the trench-parallel movements tend to diverge from the centre of the seismogenic zone. This trend is stronger in the profiles close to the coast and reduces landward. Note that the magnitude of coseismic trench-parallel displacement in the 3-D model (Fig. 3.21e) is much smaller in comparison to its horizontal (trench-normal) and vertical displacements shown in Fig. 3.21c and d.

Regarding to coseismic slip, trench-parallel slips up to ~0.5 m is indicated in the profile across the seismogenic zone, which is 8 km distant from the trench in downdip direction of the plate interface (Fig. 3.21f). It can be seen that the trench-parallel slip is at least one order of magnitude smaller than the dip slip in the seismogenic zone, and such difference is kept in the further downdip area (not shown in the figure). At last, coseismic dip slips of the 2-D model are compared with the 3-D model as shown in Fig. 3.21g. The slip in opposite directions can be seen close to the downdip limit of the seismogenic zone in the 3-D model (but not in the 2-D model), where coseismic slips up to ~5 m are also indicated in trench-parallel direction. Moreover, the magnitude of dip slip in the 3-D model fluctuates strongly along the plate interface, whereas more homogenous pattern is obtained in the 2-D model.
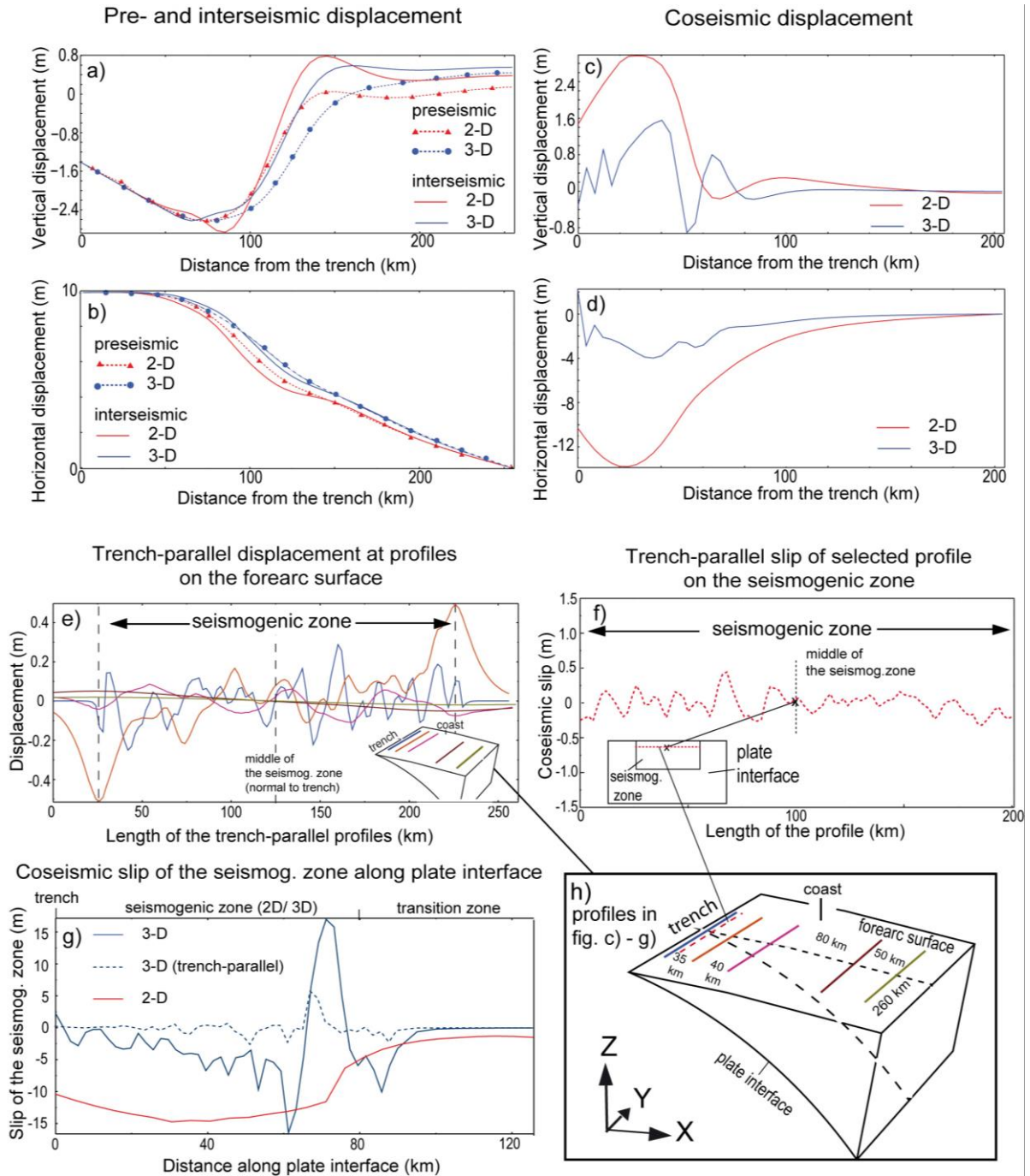
Figure 3.21 Comparison of the displacement and slip through the seismic cycle between the reference models in 2-D and 3-D. The positions of the presented profiles are indicated in h): black broken lines delineate the profiles for a)-d) and g) on forearc surface and plate interface, respectively; the red broken line on the plate interface illustrates a trench-parallel profile across the middle of the seismogenic zone with its results in f), whilst the colour lines, which are same in length and the distance between each line is given, indicate trench-parallel profiles on the forearc surface with results shown in e). a) & b): vertical and horizontal displacements in pre- and interseismic phases as well as c) & d) in the coseismic phase are compared; e): coseismic trench-parallel displacements (-y direction) of the selected profiles on the forearc (only possible in 3-D model), the colours of the curves are same with the colour of corresponding profiles on the forearc surface shown in h); f): coseismic slip in trench-parallel direction; g): coseismic slip of tangential direction (dip slip) shown in the profile at plate interface in the 2-D (red line) and 3-D model (blue line); blue broken line shows coseismic slip in trench-parallel direction of the same profile in 3-D model.

3.4 Discussion and conclusions

The objectives of this study were to improve our understanding of stress accumulation during the pre- and interseismic phases of large earthquakes, and the release of the accumulated stress in subsequent earthquakes, in order to obtain into the insights on the seismic cycles of large subduction zones.

Previous studies have revealed that high-magnitude earthquakes, e.g. the recent 2010 M_w 8.8 Maule and 2011 M_w 9 Tohoku-Oki earthquakes, are generated at the shallow part of the plate interface (Moreno et al., 2010; Kato and Yoshida, 2011; Kodaira et al., 2012; Ozawa et al., 2012). Based on this consideration, the downdip limit of the model seismogenic zone in this study was < 25 km below the forearc surface. Previous studies showed that the downdip limit of the seismogenic zone is thermally constrained, i.e. it downdip limit is the 350 °C-isotherm followed by a transition zone to 450°C where ductile deformation begins; moreover, a transition from seismogenic velocity-weakening to stable-sliding velocity-strengthening behaviour can occur (Hyndman and Wang, 1995; Wang et al., 1995). In this study, the transition zone reaches until a depth of 40 km and it is assumed that the rupture zone of large earthquakes also extend to the transition zone. Furthermore, updip limits of the seismogenic zone, which is also thermal controlled by temperatures of 100-150 °C and locates 2-15 km deep (Cailleau and Oncken, 2008), is set to the trench in this study, concerning that the rupture zone of large earthquake can extend to the trench axis, as shown, e.g. for the Maule 2010 earthquake (Vignl et al., 2011) as well as the Tohoku-Oki 2011 earthquake (Lay et al., 2011; Kodaira et al., 2012; Ozawa et al., 2012; Lin et al., 2013; Tajima et al., 2013). The entire seismogenic zone is kept locked in the models during both the preseismic and interseismic phases, which are both 100 a long. Preseismic as well as interseismic locking has been proven to be indications of future ruptures of asperities in subduction zones (Chlieh et al., 2008; Ruegg et al., 2009; Moreno et al., 2010; Métois et al., 2012), and the recurrence time of large earthquake is within hundred years (Wang et al., 2012; Aron et al., 2013). Based on the model results, some fundamental features of subduction earthquakes can be summarized as following: 1) breaking of the entire seismogenic plate interface can result in some ten meters of coseismic slip of the upper plate relative to the subducting plate (Fig. 3.4); 2) coseismic slip is largest at the shallow part of the seismogenic zone, and it occurs also at the transition zone where shear stress accumulated (Fig. 3.6); 3) occurrences of earthquakes can modulate the forearc deformation rates during the locked period of megathrust; 4) coseismic deformations of the upper plate depend on the frictional properties and the position of downdip limit of the seismogenic zone.

The modelled maximum coseismic slip is ~15 m in this study, which is resulted by the release of stress accumulated in the upper-plate during the 100-a long preseismic phase and the assigned 100 mm/a convergent rate. The average slip estimated from the 2011 Tohoku-earthquake was 10-15 m (Hasegawa et al., 2012) but the maximum slip of 33 m was determined at the hypocenter of the 2011 Tohoku earthquake by Pollitz et al. (2011) using GPS date. It seems the applied model underestimated the coseismic slip. However, it must be accounted for a shorter locked period, given the fact that the last tsunamigenic earthquake

occurred in Japan was in 869 (Tajima et al., 2013) and the pacific plate is subducting against the Okhotsk plate at a rate of ~9 cm/a offshore of the Tohoku region (Ozawa et al., 2012). Therefore, it is assumed the applied model setting is representative for subduction zone settings associated with large interplate earthquakes. Moreover, the GPS-based estimations in Pollitz et al. (2011) were attributed mostly to the seafloor displacement up to 24 m at ~10 km depth, from which the rest is attributed to the displacement of the subducting slab in opposite direction (see also Ozawa et al., 2012). Note that deformations of subducting plate are not considered in the applied model, which may also contribute to the smaller modelled coseismic slip of the upper plate relative to the subducting plate. A similar undeformable slab was assumed in Cailleau and Oncken (2008), in which a rigid slab was applied and able to reproduce the Miocene kinematics for the forearc deformation in Nicaragua. Conrad et al. (2004) reported that a subduction zone under compressional or extensional stress environment can be associated with a weak or strong slab pull. However, rollback of subducting slab belongs to the processes that affect plate-coupling strength on million-year timescales. Therefore, it was assumed here that deformation of subducting slab can be ignored in one or more seismic cycles, however, for modelling the complex evolution of a convergent margin, the deformation of subducting plate in response to the hanging wall deformation should be considered (Cailleau and Oncken, 2008). Also, bending stress of the subducting plate can be important for the deformation patterns. Kanda and Simons (2010) included elastic plate thickness and bending stresses into their models basing on the concept of simple back-slip models, and they showed that their modifications are more applicable to fit with interseismic geodetic data at convergent margins since they compensated the neglected steady state deformation in a backslip model. However, they also pointed out that the application of blackslip modes is restricted to the case when the accumulated stress during the interseismic period are fully released by seismic or aseismic events in the shallow portion of the subduction zone. In this case, the application of finite-element models may overcome these restrictions by their complexity in geometry and material properties. Moreover, it is commonly realized that plate convergence provides first-order control on the evolutions of subduction zones (Stern, 2002; Wang et al. 2012). Therefore, ignoring subducting plate deformations as well as bending stress should be acceptable for this parameter study. Moreover, as reviewed by Cohen (1999) on modelling studies on crustal deformations occurring between major seismic events, homogenous or layered elastic models may explain first-order features of the earthquakes, but viscoelastic flow in upper mantle and the lower crust play important roles on another mechanism for time-dependent deformation, e.g. by aseismic fault slip. Here, a viscoelastic lower crust and a lithospheric mantle are assigned in both 2-D and 3-D model domains. With the given rheological parameters in Figs. 3.2-3, the relaxation time is calculated for over 10^4 years (cf. Turcotte and Schubert, 2002). In comparison, the modelled seismic cycle here is on a timescale of 10^2 years, because the aim of this study is not to derive the evolution of the forearc but to better understand the kinematics within seismic cycles, so the influence of viscous flow is not considered in this study. However, Trubienko et al. (2013) observed with numerical models that the ratio of the viscosity in the asthenosphere to the period of the seismic cycle may influence the distance over which seismic cycle perturbs the local displacement velocity, but they focused mainly on the interseismic deformations in response to varying rheologies of the upper plate.

Further study was carried out by applying both 2-D and 3-D finite-element models to systematically examine the fundamental parameters that have been considered to be crucial for seismicity of the subduction zone. Results are discussed in the following sections.

3.4.1 Factors influencing seismic cycles at subduction zones

Friction along the plate interface

Being aware of the first-order control of plate convergence on the evolution of subduction zones, more studies focus also on the second-order control, such as heterogeneities of rheology, plate coupling strength, material properties and physical properties of the plate interface on the deformation and seismicity of the subduction zones (Lay et al., 1982, 2012; Moreno et al., 2012; Tajima et al., 2013). The existences of asperities that cause high coseismic slip, but also act as barriers that show low or no slip, represents the heterogeneities of the plate interface. They may determine the pattern of interseismic stress accumulation and also of the coseismic energy release within the rupture area (Kanamori, 1986; Bürgmann et al., 2005; Melnick et al., 2009; Moreno et al., 2011, 2012; Tajima et al., 2013). Cailleau and Oncken (2008) investigated the role of inhomogenous friction along a megathrust on forearc deformation in Nicaragua, based on a 2-D numerical subduction zone model with an undeformable subducting plate in contact with a homogenous elastoplastic upper plate on the established plate interface. They demonstrated that by varying frictional properties of the plate interface, i.e. the depth, length and friction of different segments, the modelled strain accumulation can reproduce the deformation observed in Nicaragua. But they did not model any seismic cycle. The model results presented in Fig. 3.5 (2-D) and Fig. 3.14a (3-D) indicate that assigning different frictional properties, i.e. different friction coefficient for seismogenic, transition and free-slip zones, respectively, can capture the main features of forearc deformation within a seismic cycle. As the seismogenic zone is locked during the preseismic and interseismic phase, convergence (100 mm/a) is accommodated by subsidence and uplift, which occur seaward and landward to the coast, respectively. As shown in the 2-D reference model, the spatiotemporal distribution of uplift and subsidence is similar in both phases, in which subsidence rates are almost the same; however, preseismic uplift rate is calculated for only ~0.5 mm/a, which is two magnitudes smaller than the interseismic uplift rate of ~10 mm/a (Fig. 3.5a). This may be caused by the enhanced interseismic downdip displacement occurring at the shallower depth of the plate interface relative to the preseismic displacement (see Fig. 3.10a and c - results of REF), which indicates stronger strain accumulation at this region during the interseismic phase. Moreover, uplift of the coastal areas at rates of a few millimetres per year has been commonly observed in subduction zone with a narrow seismogenic zone (e.g. Thatcher and Rundle, 1984; Hyndman and Wang, 1995), but these data cover mainly a postseismic or interseismic period within one or more seismic cycles. Data on preseismic deformation has been relatively rare until the recent 2010 Maule (Chile) earthquake, where the last major event was in 1835 (Moreno et al., 2010). The rupture zone of the Maule earthquake was observed as highly locked areas (asperities) before the earthquake but the preseismic locking decreased rapidly downdip and in the direction of plate convergence (Moreno et al., 2010), which may result in smaller uplift. Furthermore, the subsidence reduces in the transition zone and indicates stress accumulation, which is released

in the subsequent earthquake (Fig. 3.6a). Coseismic uplift compensates approximately the preseismic subsidence at the same area (Fig. 3.5), which has been commonly observed in nature and also shown by other elastic dislocation models (e.g. Thatcher, 1984a; Savage and Plafker, 1991; Barrientos and Plafker, 1992; Hyndmann and Wang, 1995). Modelled coseismic subsidence also occurs in the area above the downdip limit of the seismogenic zone shown in Fig. 3.5e, which are rarely shown previously by either homogenous or elastic dislocation models. Nevertheless, Ozawa et al. (2012) observed also coseismic subsidence along the Pacific coastal area from the Tohoku 2011 earthquake, which they further regarded as one of the mechanisms for compensating the long-term uplift at Tohoku coastal region.

Increasing friction of the seismogenic zone results in a decrease in the magnitude of coseismic displacements as shown in Fig. 3.5e-h and Fig. 3.7, which also indicates that the stress and slip deficit accumulated in the preseismic phase are not fully released and compensated from the earthquake as indicated in Fig. 3.6. The rest of slip deficit may be compensated by afterslip and aftershocks, or results in subsequent earthquake events, which eventually moderate the seismicity of the subduction zones (Kanamori et al., 2006; Suito et al., 2011; Ozawa et al., 2012; Wang et al., 2012; Tajima et al., 2013). Kanamori et al. (2006) recognized that despite the significant earthquake activity along the east coast of Honshu, Japan, only part of the accumulated strain associated with subduction had been relieved. They anticipated the potential of a large earthquake that would combine the areas and characteristics of previous events, and this turned out to be the character of the 2011 Tohoku-Oki event as noted in Tajima et al. (2013). Although neither afterslip nor aftershock is considered in the presented models, the enhanced interseismic uplift shown in Fig. 3.5a can be then also regarded as a consequence of the unreleased stress.

Therefore, it is indicated that the friction state of the plate interface, no matter transient or steady state, may play an important role in the seismic cycle of subduction zones. The specific causes of variations in the frictional behaviour of plate interface are still under debate. Studies revealed the presence of fluids or high pore pressure could reduce the shear velocity and possibly the frictional strength of the plate interface, which may also moderate the tectonic stress state of the upper plate (e.g. Wang and He, 1999; Bilek and Lay, 1998; Seno, 2005; Zhao et al. 2011; Wallace et al., 2012; Tajima et al., 2013 and references therein). Accounting for the processes of changing frictional behaviours are beyond the objectives of this doctoral thesis, therefore it has been simplified by varying the frictional coefficient in the models, by which the resulting changes are also significant.

The above findings by 2-D modelling are also observed in the 3-D models as shown in Figs. 3.14-15). However, including trench-parallel components of the subduction zone may result in more complicating displacement patterns in terms of magnitude and distribution. The differences are shown in Chap. 3.3 and will be further discussed in the following section.

Variations in downdip limit

The updip and downdip limits of the seismogenic zone may control the size of rupture area of an earthquake that determines the magnitude of this event (Donald et al., 1994; Hyndman and

Wang, 1995; Wang and He, 1999). Previous studies focussed on determining the updip and downdip limits of the seismogenic zone of a subduction zone by seismological data and geodetic observations fitted with simplified models, e.g. elastic dislocation models (Dragert et al., 1994; Hyndman and Wang, 1995). Also, it has been realized that the downdip limit of the seismogenic zone is controlled by temperature (Wang et al., 1995; Hippchen and Hyndman, 2008) or by the position of the Moho of the upper plate forearc (Seno, 2005). Other studies focussed mainly on the mechanical impacts of varying frictional properties of the plate interface on post- and interseismic deformations, as well as on long-term deformations (Wang and He, 1999; Cailleau and Oncken, 2008; Kato and Yoshida, 2011; Métois et al., 2012). So far, forward modelling of the influence of downdip limit on upper plate deformation in a complete seismic cycle is not yet common (e.g. Trubienko et al., 2013). In this study, the updip limit of seismogenic zone in the presented models is fixed at the trench, whereas downdip limit is changed from 25 km to 10 km below surface. The objective of this experiment is to observe the sensitivity of upper plate deformation within a seismic cycle on changes in downdip limit.

It is shown in Fig. 3.11a, b, e and f that pre-, co- and interseismic displacements at the forearc surface are sensitive to the position of the downdip limit, particularly in the area above the seismogenic zone. Peaks of vertical and horizontal displacements are coincident to the position of the downdip limit of each model, i.e. surface displacements are stronger in the vicinity of the trench (0-25 km landward to the trench) than further landward. This has been also observed by Wang and He (1999) that a narrower and shallower frictional coupled area may cause large compression in the accretionary wedge of the forearc relative to further landward. However, it can be also seen that such sensitivity decreases as the downdip limit becomes deeper, which is reflected by smoother displacement patterns and also obviously less differences between the preseismic and interseismic displacement.

In the cross-section shown in Fig. 3.10a, preseismic deformations of the upper plate accommodate the assigned convergent rate as reflected by the total displacement in the seismogenic zones. However, strong preseismic deformations occur in the transition zone regardless to the positions of the downdip limit of the seismogenic zone, which are strongest at the lower segment of the transition zone but decrease rapidly as entering the free-slip zone. This can be due to the change in frictional properties that free-slip zone is assumed for frictionless, but it also indicates stress accumulates not only in seismogenic zone but also in the lower depth. The accumulated stress can be mostly released in subsequent earthquakes in form of coseismic slip and afterslip, however, their specific patterns are not yet well resolved by previous studies. Coseismic displacement shown in Fig. 3.10b indicates that large trenchward displacement occurs mainly in the shallower depth of the plate interface. A shallower downdip limit of seismogenic zone can result in lower coseismic vertical displacement but not necessarily smaller seaward horizontal displacement (see also Fig. 3.11h). It is also shown that the areas with large coseismic displacements are more depth-dependent rather than dependent to the positions of downdip limit, i.e. the positions of hinge (the transition between increase and decrease in uplift) are all located in the shallower segment of the plate interface (Fig. 3.10b and Fig. 3.11f). This finding is also indicated in Fig.

3.12a that the maximum coseismic stress drops from different length of seismogenic zone are all largest at ~70 km downdip of the plate interface. Shear stresses even slightly increase at the downdip limit of the seismogenic zone. In contrast, the peak of coseismic slip seems to be coincident with the downdip limit of the seismogenic zone (Fig. 3.12b), except in the case of the deepest seismogenic zone, maximum of coseismic slip still occurs at its shallower segment ~8 km below the trench. Moreover, the values of maximum slip are not much different among the three examined lengths of the seismogenic zone, except that the affected segment with high coseismic slip is wider in a deeper extended seismogenic zone. This indicates the coseismic-released stress is better transmitted in updip direction, which leads to higher coseismic slip in the seismogenic zone. The above observations are confirmed in the slip histories of observation points along plate interface as shown in Fig. 3.13. Since the positions of point P1-P10 are fixed, therefore the recorded slip histories of each point are subject to the frictional properties of the segment. As the seismogenic zone is locked in the preseismic phase, i.e. slip is zero, preseismic slip deficits are also pronounced in the whole transition zone but decreases from the beginning of the free-slip zone.

The different patterns in coseismic stress drops and displacement resulted by the different downdip limit determine their individual interseismic pattern. As shown in Fig. 3.10c, total displacement increases strongly in present of a shallower seismogenic zone, the magnitude of which even exceeds the assigned convergent rate of 100 mm/a. This is also reflected by the patterns of interseimic horizontal displacements shown in Fig. 3.11a-d, which clearly differs from the preseismic pattern particularly in the shallower part of the plate interface. This can be explained by the slip histories of the observation points shown in Fig. 3.13: after the perturbation of earthquake, the steady slip rates generally decrease in the transition zones of all three models, which may be interpreted as increase in plate coupling strength after a large earthquake. A highly coupled zone was observed at the southern boundary of Maule segment in south-central Chile, which only very few moderate earthquakes occurred since 1976 till the 2010 Maule earthquake (Métois, et al., 2012). Also, Wallace et al. (2012) suggested that the state of tectonic stress and structural permeability in the upper plate may determine the interseismic coupling depth on subduction interfaces, e.g. in New Zealand, Vanuatu and southwest Japan. Also, both stress state and fluid pressure of the upper plate might change throughout a seismic cycle (e.g. Wang and He, 1999; Wang et al., 2012; Aron et al., 2013). This implies that the downdip limit of seismogenic zone can be also one of the parameters for controlling the physical mechanisms of interseismic coupling. In contrast, at point P7 located in the free-slip zone close to the end of transition zone, the slip rate is somehow larger in comparison to preseismic rate, which might be an indication of continuous relax in stress and slip deficit from the shallower segment because free slippage is allowed but prohibited in updip direction. Similar results were obtained in the numerical models by Kato and Yoshida (2012), in which the plate interface is subdivided by regions with velocity-weakening and velocity-strengthening frictional properties. They found that the slip deficit is accumulated at the deeper part of the plate interface where M7 earthquake occurs because the locked shallow portion prohibits free slippage.

In conclusion, the amount of shear stress drop is not directly correlated with the magnitude of slip or earthquake, i.e. low shear stress drop may still result in high seismic slip, which agrees with the findings by Wang (1995) and Wang and He (1999). A recent study of Lin et al. (2013) observed a nearly total stress drop at the frontal plate interface in the 2011 M_w 9 Tohoku-Oki earthquake. Therefore, it suggests that the state of stress drop of the plate interface, rather than the absolute amounts of stress drop, may play a more important role on the magnitude of subduction earthquakes. The position of downdip limit somehow affects the patterns of the release of accumulated stresses, and the potential of subsequent earthquakes can be higher in a shallower seismogenic zone due to the accumulated stress in the transition zone but this stress may not fully release in one large earthquake.

Besides variations of plate interface properties at dip-direction, variation in the degree of interseismic locking is often inferred from geodetic measurements also in along-strike direction, which can affect the time and size of future rupture (Wang et al., 2012). The results of the presented 3-D models here include not only the variations in the downdip limit of the seismogenic zone, but also lateral variations by assigning two locked zones at each side of the seismogenic zone. In general, similar patterns to the results from 2-D models can be seen from displacement field throughout a seismic cycle of the 3-D models. However, coseismic displacements at the forearc surface of the 3-D models highly fluctuate relative to the 2-D profile, which are characterized by lower uplift but intercepted by stronger subsidence at ~60 km and ~110 km landward from the trench in comparison to the 2-D model (see Fig. 3.11e and Fig. 3.18b). Levelling data obtained after the Maule 2010 earthquake indicate a transition between coseismic uplift and subsidence located ~120 km from the trench (Vigny et al., 2011). The modelled coseismic displacement pattern from the present 3-D model is most obvious in the deepest seismogenic zone but not in the shallow and intermediate seismogenic zones. This may correspond to the patterns of the coseismic slip observed from the three models. As shown in Fig. 3.18c, coseismic slips in opposite directions occur in the lower segment of the deep seismogenic zone. No direct indications from the model setup itself can be found for explaining this phenomenon. However, it can be seen in Fig. 3.19 that seaward horizontal displacements at the trench of the deep seismogenic zone are much smaller than in a similar 2-D model, which are compared in Fig. 3.21d. The accumulated stress can be partly released in lateral trench-parallel direction as indicated in Fig. 3.21f, which results in smaller slip at the trench (Fig. 3.21g). This may prohibit stress from releasing in updip direction and therefore increase the tendency of downdip release, which results in the downdip slip. Nevertheless, due to the friction in transition zone, downdip slip cannot extend deeper, so it is constrained to resolve locally and leads to a narrow pattern of subsidence in the forearc surface above. In contrast, in the shallow and intermediate seismogenic zone models, coseismic slip is similar in seaward direction. It may be interpreted that the accumulated stress can release in both updip and lateral directions and therefore no downdip slip occurs.

3.4.2 Modelling subduction zone earthquake with 2-D or 3-D models?

In this thesis, same parameters were examined with 2-D and 3-D models using similar settings. The question to answer was how much do 2-D and 3-D models differ? 2-D modelling has been broadly applied in many studies given by its simplifications, whereas 3-D

models are closer to reality since a real subduction consists of segments with different characteristic earthquake periodicity, coupling depth and geometry (Trubienko et al., 2013). It can be seen from the individual results of 2-D and 3-D models that the general impacts of a variable friction coefficient and downdip limit of the seismogenic zone are not different (see Chap. 3.3.1-3). In particular, the resulting preseimic and interseismic displacements are very similar. Numerical modelling carried out by Trubienko et al. (2013) demonstrates that the horizontal displacement through a complete seismic cycle for 2-D and 3-D models at ~700 km the trench is rather similar; also, the predicted velocities of postseismic displacement from 2-D and 3-D are almost the same.

However, it is demonstrated in this study that fundamental differences exist in the model responds of coseismic phase between 2-D and 3-D models. It has been discussed in previous section that coseismic deformations can be attributed to additional mechanisms such as trench-parallel movements and/or lateral viscous flow, which are not captured by 2-D models. Finer elements with 2000-m edge length have been applied in the seismogenic zones of the 3-D models. Further refinement on the 3-D model grid can neither significantly improve the fluctuating patterns show in the coseismic displacements (as shown in Fig. 3.14b), nor eliminate the opposite-sense coseismic slip patterns appearing in the 3-D models. Therefore, these observed patterns should not be addressed to problems on model resolutions.

Furthermore, Wang et al. (2012) in their reviews on subduction zone models stressed that ignoring the role of viscous mantle flow in interseimic surface deformation will lead to incorrect depiction of the locking state of the subduction fault, since the deformation can be then mainly, or only, attributed to the locking and slip of various part of the subduction faults. Applying 3-D modelling can solve this concern. Moreover, including lateral variations of the plate interface provides better insight on the coseismic deformation of a subduction zone. For example, the calculated surface total horizontal displacements (Fig. 3.20) indicate that the displacement vectors diverge in the seismogenic zone, and also show that the spreading of coseismic displacements depends on the downdip limit of the seismogenic zone. The former observation has been studied by Hampel et al. (2013), in which similar divergent postseismic surface vectors were shown with numerical models as well as GPS data of several thrust faults, and they emphasized the importance of studying these patterns since they may infer the deformation patterns as well as the local rheology of the observed area.

3.4.3 Model application to case studies

Deformation patterns and dominating processes of earthquake cycles at each subduction zone can be different, due to local tectonic settings as well as the properties of the plate boundary. In this framework, apart from the previous parameter studies, two subduction zones, i.e. Chile and Japan, were selected as case studies for application of the models. Both convergent margins accommodate high convergent rates, ~7 cm/a in Chile and ~9 cm/a in Japan. Both are seismically active regions, including the occurrence of the largest seismic events recorded by modern instruments, e.g. the 2010 M_w 8.8 Maule and 2011 M_w 9.0 Tohoku-Oki earthquakes. The former has stimulated further research on the heterogeneous plate coupling, and the latter is a key example for variable earthquake size within the same subduction zones (Tajima et al.,

2013 and references therein). As shown in Fig. 3.22, the histories of seismicity of the Chile and Japan subduction zones are different, which are the results of their very different seismotectonic settings. Furthermore, previous studies demonstrated based on historical time-space records of great subduction earthquakes that ruptures tend to occur repeatedly within distinct seismotectonic sectors along the forearc (Melnick et al., 2009). In this thesis, the previous 3-D reference models were adopted and modified to reflect the rupture zones of the characteristic earthquake sequences in Maule (south-central Chile) and Tohoku-Oki (north-eastern Japan), in order to evaluate the potential impacts on the recurrence and magnitude of large earthquakes (Fig. 3.23). The two models are categorized into "Maule type" and "Tohoku-Oki type", respectively. In this section, the study area and the applied model are introduced, and then the results are shown and discussed.
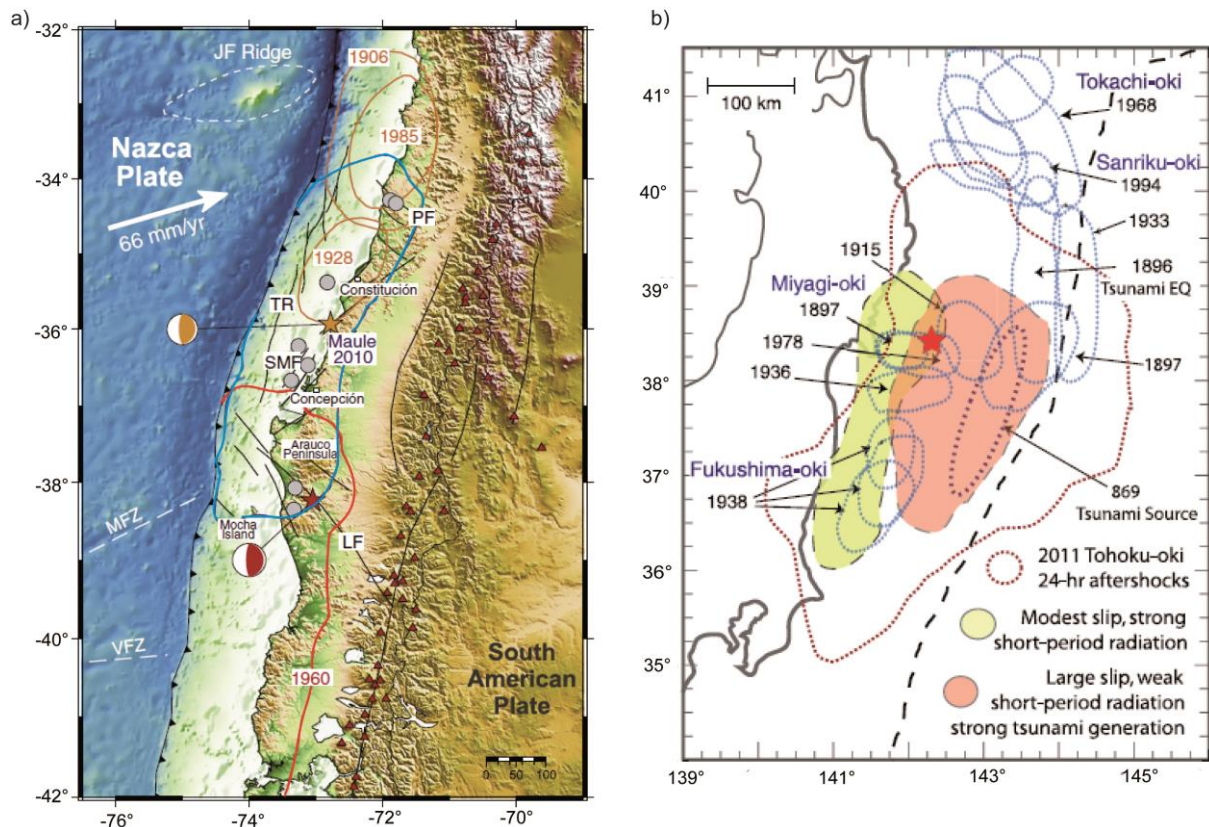

Figure 3.22 a) Recent earthquake events and regional tectonic setting of the south-central Chile megathrust (modified from Fig. 1 in Moreno et al., 2012). Rupture zones of the 1960 Valdivia and 2010 Maule megathrust earthquakes are delineated by red and blue line, respectively. Rupture zone of other events in 1906, 1928 and 1985 are indicated with orange lines. Gray cycles indicate location of aftershocks ($M_w > 6.5$). b) Schematic map showing the source areas of the historic offshore large earthquakes along the Tohoku coast (ellipses with blue dotted lines). Red star indicates epicentre of the M_w 9 Tohoku-Oki earthquake and red dots delineates its 1-day aftershock area from Fig. 3 in Tajima et al. (2013).

"Maule type" earthquakes

The south-central Chilean margin consists of different segments, which are characterized by distinct seismotectonic features and also indicated by heterogeneous interseismic locking (Melnick et al., 2009; Moreno et al., 2011; Métois et al., 2012). Different climate conditions during glacial-interglacial periods resulted in variations on erosion as well as the sediment supply to the trench along the long extended continental margin (more than 3500 km long).

71

Previous studies demonstrated that these different conditions may have altered the seismicity of the subduction zone by changing the frictional properties of the plate interface (e.g. Blumberg et al., 2008; Melnick, et al., 2009; Metois et al., 2012). Off Chile, two high-magnitudes subduction earthquakes occurred, i.e. the 1960 M_w 9.5 Valdivia and the 2010 M_w 8.8 Maule earthquakes. The observed rupture zones of the two earthquakes overlapped in their southern and northern extensions in the Arauco peninsula, which is a stable morphotectonic feature since the Pliocene (Melnick et al., 2009). The Maule segment is reported as highly coupled, with a well developed seismogenic zone prior to the 2010 event (Ruegg et al., 2009; Moreno et al., 2011; Métois et al., 2012). The last large earthquake event in Maule occurred in 1835 reported by Darwin (1851), which indicated a recurrence time of 175 years.

The "Maule type" model applied for this study is shown in Fig. 3.23a. Two overlapping ellipse seismogenic zones, which have the same in size with 200-km trench-parallel extension and 50 km in downdip direction, respectively, are located at a depth of 15 km. The model was run with a 100-year preseismic phase with two fully locked seismogenic zones and afterward the first earthquake of initiated by activating one of the seismogenic zone, whilst the other one remains locked. Then, the both seismogenic zones are locked again for another 100-year preseismic phase and subsequently the previous locked seismogenic zone is activated for the other earthquake.

As shown in Fig. 3.24, the patterns and the magnitudes of the coseismic slip within the activated seismogenic zone in subsequent earthquakes are very similar. The 1st earthquake results in > 18 m of maximum coseismic slip in some area within the seismogenic zone, which is comparable to the 17 m average slip from the 1960 Valdivia earthquake. Maximum coseismic slip is ~15 m in the 2nd earthquake. Slip in sense of convergence direction occurs at the deeper part of the seismogenic zone, which was also observed in the 3-D reference model (see Fig. 3.14c). The overlapping area experiences high coseismic slip with maximum values of ~16 m in the first earthquake but only < 2 m of slip in average occurring in the second earthquake. It can be interpreted that the accumulated stress in the overlapping area was mostly released by the 1st earthquake, and therefore results in much less slip in the 2nd earthquake than the other areas that are locked in the first earthquake. This can be clearly seen from the slip history of the selected observation points on the plate interface shown in Fig. 3.25a.

Fig. 3.25b shows the time evolution of the horizontal and vertical displacement of three observation points at the forearc surface above the centre of the two seismogenic zones and their overlapping zone. The histories of displacement above the centre of the seismogenic zone correspond to the occurrence time of the earthquake, and the magnitudes in coseismic displacement from the individual earthquakes are similar. It can be seen that the coseismic deformation of the overlapping zone is strongest at the 1st earthquake but almost not observable in the second one. A similar behaviour is observed for horizontal displacement of the forearc, from which the coseismic displacement of the 2nd earthquake terminates at the boundary of the overlapping zone.

The presented scenario is of course simplified in many aspects compared to the natural setting. For example, as previously mentioned, the two seismotectonic segments overlapping beneath the Arauco peninsula (see Fig. 3.22a) is characterized by a high Quaternary uplift, which is considered as a result of microplate collisions (Melnick et al., 2009). Although with the presented simplified model shows almost continuous subsidence after the 1st earthquake, it acts as a barrier controlling the propagation of the coseismic displacement of the 2nd earthquake. This feature is consistent to the findings in Arauco that there has been only very few moderate events ($M_w < 6.5$) at the southern boundary of the Maule segment, where also high coupling rate remains (Métois et al., 2012). Also, the rupture of the 1960 M_w 9.5 Valdivia earthquake has stopped at this intersegment area (Fig. 3.22a, also Melnick et al.,
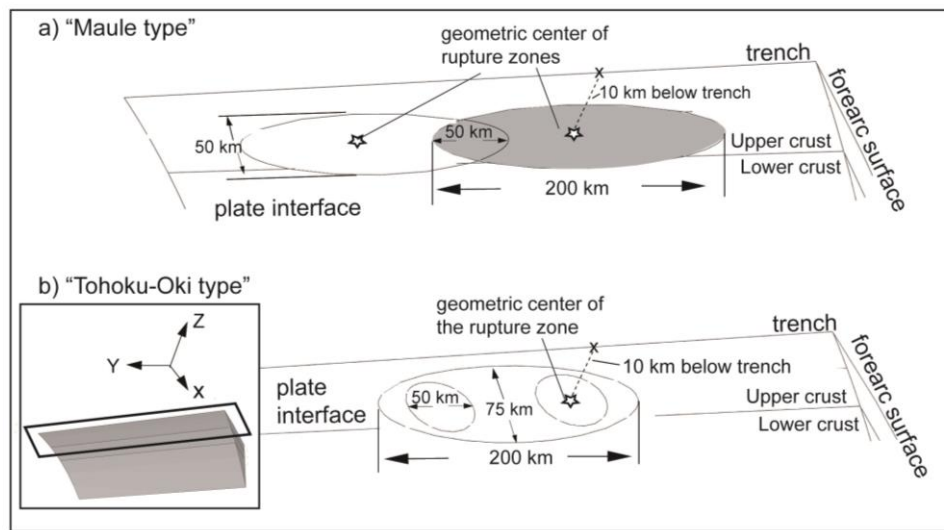
Figure 3.23 Geometries of the seismogenic zones applied in the case studies. View of the plate interface for models of a): "Maule type" with two overlapping seismogenic zones and b): "Tohoku-Oki type" with a sequence of three earthquakes within a large seismogenic zone. See descriptions in text. Other model settings remain same as the 3-D reference model shown in Fig. 3.3.
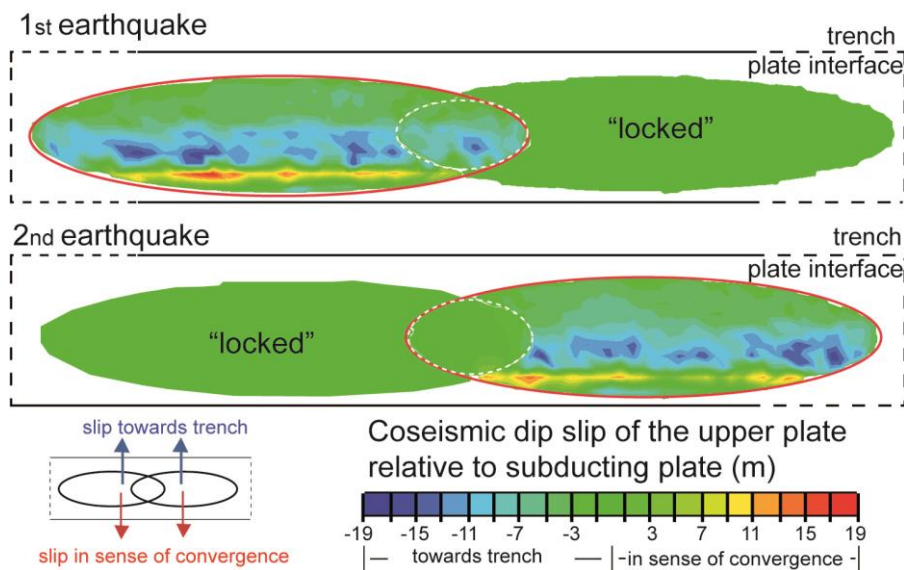

Figure 3.24 Coseismic slip on the plate interface in the "Maule type" model. In the model domain, the activated seismogenic zone in each earthquake is indicated with red line, respectively, and the overlapping area is denoted by white broken line. The direction of slip is indicated by colour coding as well as indicated in the sketch at the bottom.

73

2009). This pattern is also seen in the model results of the surface horizontal displacement shown in Fig. 3.26. The surface displacements from the 2nd earthquake are stopped at the upper rim of its rupture zone, which is the overlapping zone with the 1st earthquake. Similarly, Moreno et al. (2010) observed that the slip of the 1960 M$_w$ 9.5 earthquake tapered out beneath the Arauco peninsula, and they attributed this to 10 m of apparent slip deficit at the southern periphery of the later 2010 rupture area, which reduced the accumulated stresses in this strong coupled area. Therefore, the outcome of the present model may provide a mechanical evidence for the low seismicity of the overlapping zone.
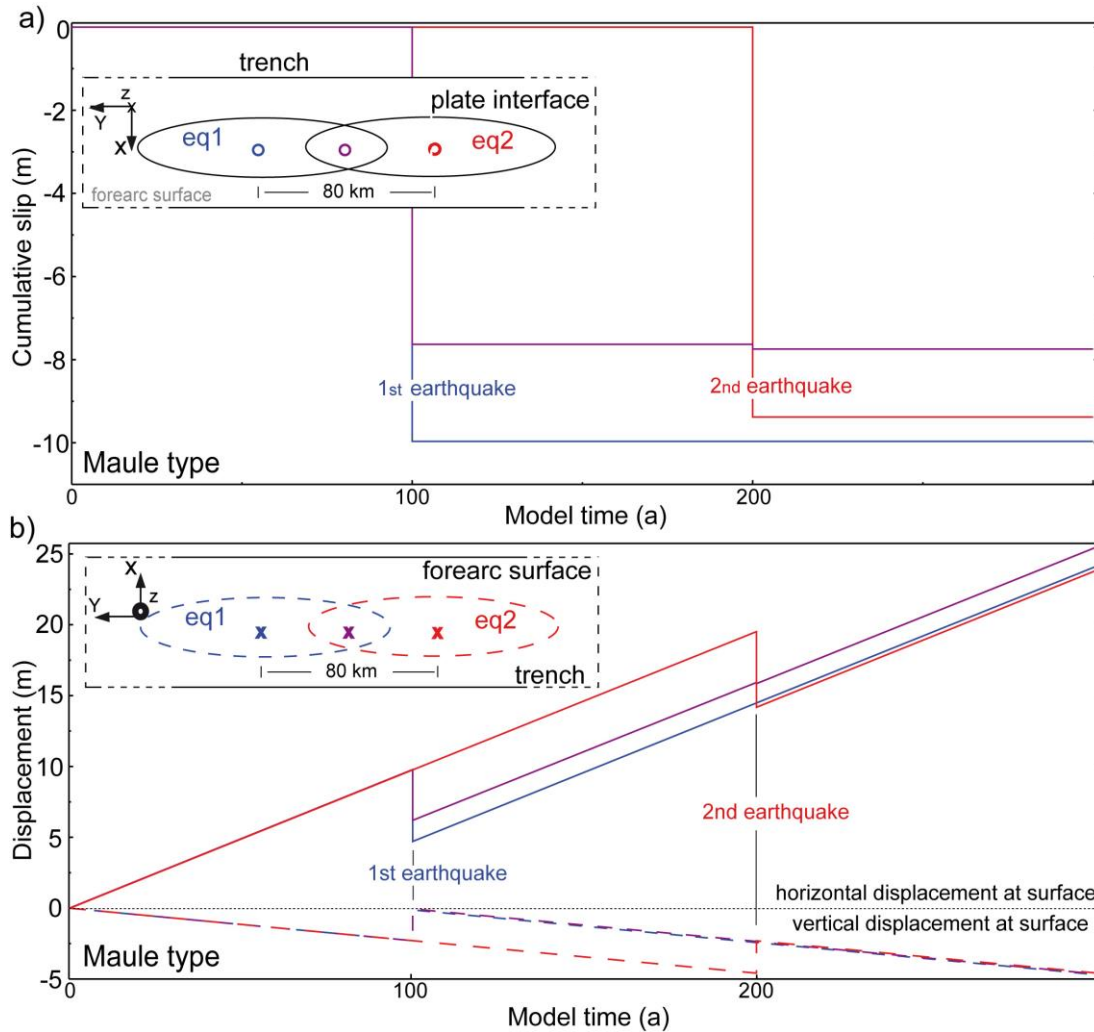
Figure 3.25 a) Time evolution of slip on the plate interface and b) displacements of the forearc surface at selected points of the "Maule type" model. In a): Sketch of map view on plate interface shows positions of the observation points with hollow cycles. Two points (in blue and red) locate at the geometry centres of two seismogenic zones and another (in purple) at the centre of the overlapping zone, and their results are plotted with lines in same colours, respectively. In b): Sketch of map view on forearc surface shows positions of the observation points with crosses. The three selected points locate at the projected geometry centres of two seismogenic zones and of the centre of the overlapping zone on the forearc surface, respectively. Results are plotted with same colour of the observation points, and coseismic displacements are shown with broken lines.

The settings with two trench-paralleled seismogenic zones in the model may somehow represent the observed heterogeneities in plate coupling on along-strike directions at the Chilean margin (e.g. Wallace et al., 2012). However, trench-parallel variations in preseismic surface deformation rates are not obvious as indicated by the model results (see Figs. 3.25b,

3.26b). Further modelling of this type should include other mechanical processes, e.g. afterslip, creeping and aseismic slip at the accretionary wedges. For example, based on GPS
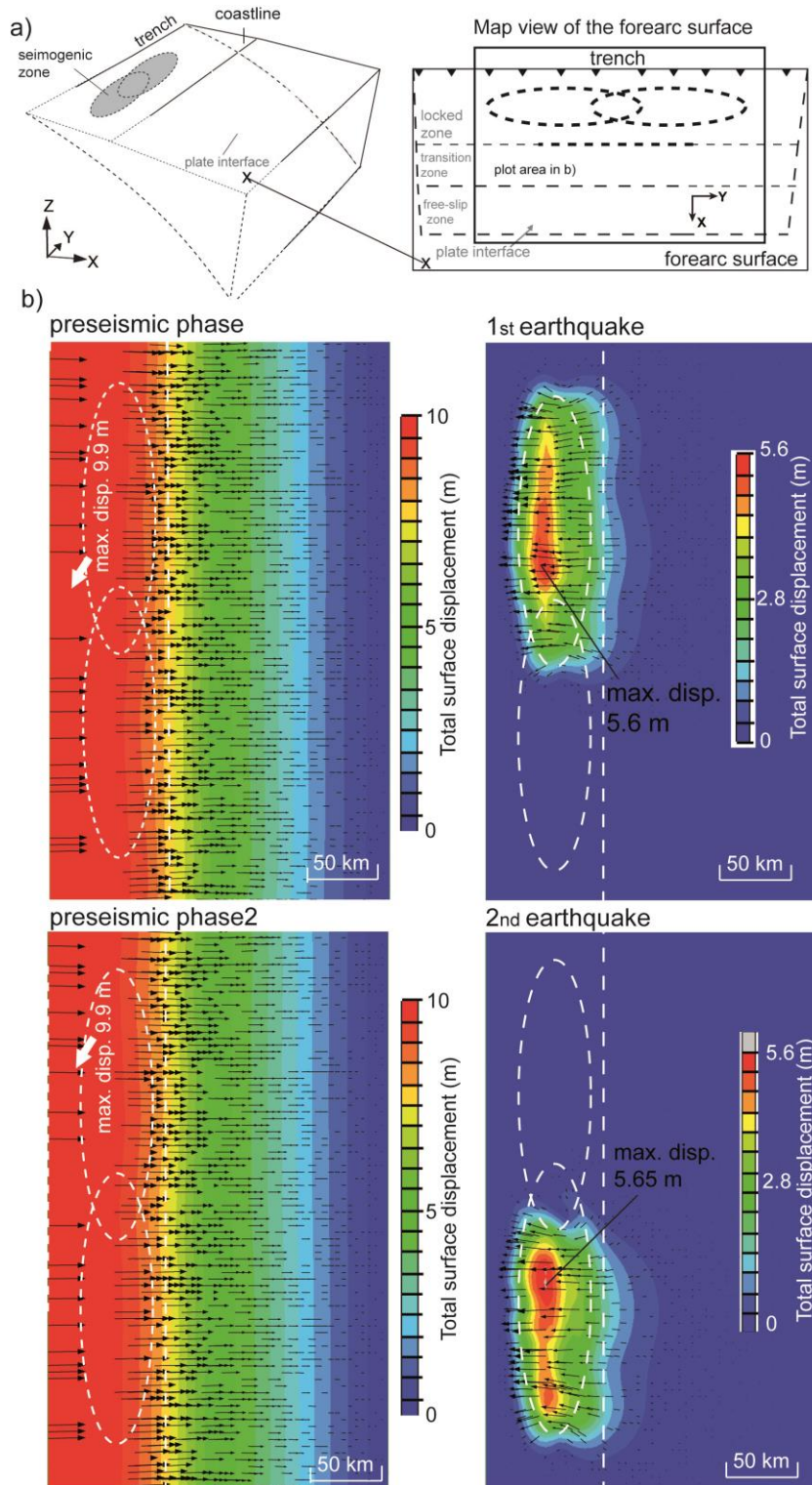

Figure 3.26 Total surface horizontal displacements for the "Maule type" model. The map view of the observed area is illustrated by the sketch in a) and the results in different phases are shown in b). The displacement patterns are shown by colour coding and arrows, which indicate the direction of the displacement vectors. The positions of the seismogenic zones projected on the forearc surface are denoted by white ellipses and the upper limit of the transition zone is indicated by white broken line. Maximum values of coseismic displacement in each earthquake are given as numbers.

data on surface velocity and kinematic finite-element models, Moreno et al. (2011) observed that the rupture zone of the 2010 Maule earthquake is kept fully locked, but a significant amount of creep occurred along the Valdivia segment which ruptured in 1960. They also observed that the central part of the 1960 rupture zone is also fully locked and postulated a potential occurrence of a M8 earthquake, which can be triggered by the static stress changes from the 2010 Maule earthquakes. Also, glacial sedimentation should be considered particularly at the Chilean margin, as the climate-induced variability in sediment supply to the trench plays an important role on this margin tectonics (Borugois et al., 2000; Völker et al., 2006). For example, continuous GPS stations, which have been installed after the Maule 2010 earthquake along the rupture zone and from the Chilean forearc to the backarc thrust front in Argentina, have observed ongoing postseismic seaward motion at the forearc and continuous backarc extension. This can be attributed to the abundant trench sediment fill in the Valdivia and Maule rupture zones, which may reduce the basal friction of the plate interface as being subducted by convergence (Brooks et al., 2011).

"Tohoku-Oki type" earthquake

In Japan, the Pacific plate subducts west-northwestward against Okhotsk plate at a rate of 80-100 mm/a (Sella et al., 2002; Kato et al., 2012). It is one of the seismically most active regions of the world. The subduction of Pacific plate has generated sequences of devastating interplate thrust earthquakes, including the recent devastating Tohoku-Oki earthquake 2011 (Mw = 9) (Fig. 3.22b) that ruptured a wide region (~200 km) of the megathrust (Lay et al., 2012). The recurrences of high-magnitude earthquakes as well as state of crustal deformation have been monitored by a dense network of continuous GPS and seismic stations (Kato et al., 2012; Wang, et al., 2012). In the Sanriku region, northeastern Japan, where the Pacific plate subducts beneath northern Honshu, M8 class earthquakes occurred approximately every 100 a, but the recurrence and the generating mechanisms of great earthquakes like the 2011 Tohoku-Oki earthquake are not yet well understood (Kato, 2008; Kato and Yoshida, 2011). Some proposed that the coseismic slip and afterslip of each earthquakes, the postseismic slip as well as aseismic slip at the plate boundary have influenced the spatial and temporal distributions of earthquakes in this region (Kato et al., 2012; Ozawa et al., 2012; Tajima et al., 2013).

Based on some of the observed features by the abovementioned studies showing that sequences of earthquakes occurred in the rupture area of the later 2011 M_w 9 earthquake (see also Fig. 3.22), the 3-D reference model (Fig. 3.3) was modified by adjusting the geometry as well as the number of seismogenic zones on the plate interface, which is shown in Fig. 3.23b. Two smaller seismogenic zones, each with a radius of 25 km, are located coaxially on the plate interface between the upper and lower crust. Their centres are located ~15 km below the surface and the distance between them is ~100 km. These two zones are located at both sides of the centre of a large ellipse-shape seismogenic zone, which extends 200 km in trench-parallel direction and 75 km in downdip direction, respectively. At first, after the initial phase (see details in Chap. 3.2.2), the model is run for 100 a as the preseismic phase, in which all seismogenic zones are fully locked. Then, the 1st earthquake occurs at one of the small seismogenic zone. Afterward, all the seismogenic zones are locked again for another 100 a,

until the 2nd earthquake occurs at the other small seismogenic zone and all zones are locked again subsequently for another 100 a. At last, the 3rd earthquake occurs in the large elliptical seismogenic zone, in which the whole area is unlocked.

The resulting coseismic slips are shown in Fig. 3.27. The resulting patterns and magnitudes of coseismic slip in the individual seismogenic zone are similar from the 1st and 2nd earthquakes. It can be seen that the coseismic slip (towards trench) from the 2nd earthquake relative to the 1st one is larger by ~2 m and occurs at a limited area close to the boundary of the seismogenic zone, this can be an indication of a longer period of stress accumulation at this area. The 3rd earthquake occurring in the large elliptical seismogenic zone leads to maximum coseismic slip of ~20 m towards trench in the centre of the rupture zone. Note that the rest of areas in the elliptical seismogenic zone outside of the rupture zones from the 1st and 2nd earthquakes stay locked before the occurrence of the 3rd earthquake. In comparisons, coseismic slips at the two
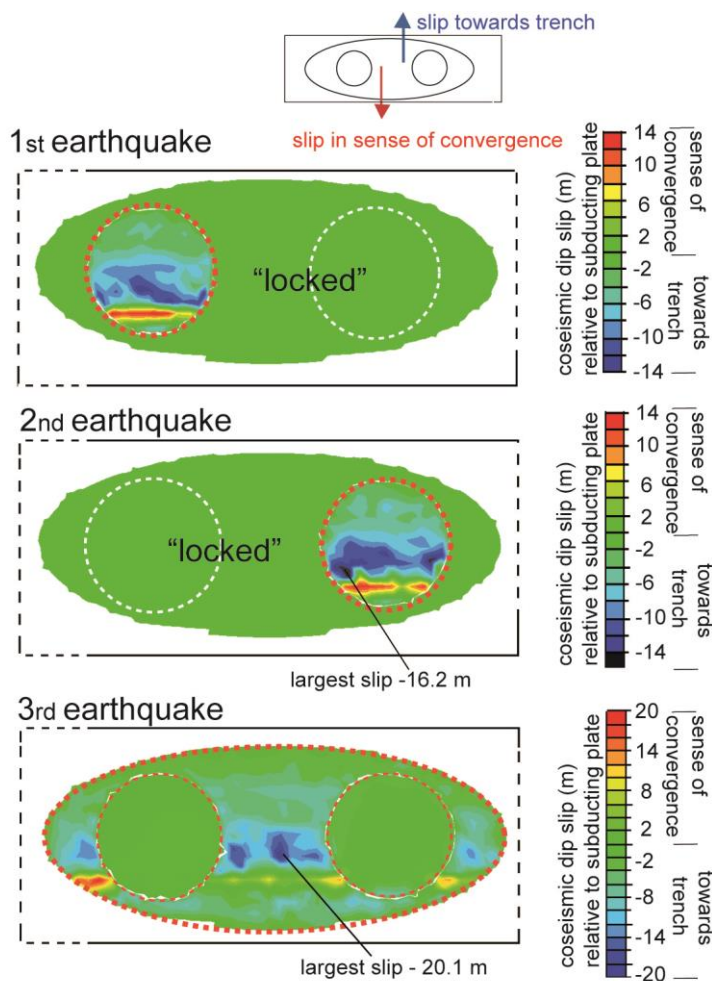

Figure 3.27 Map view on modelled coseismic slip on plate interface for the "Tohoku-Oki type" model. In the model domain, the activated seismogenic zone in each earthquake is indicated with red line, respectively. The direction of slips is indicated by colour coding as well as indicated in the sketch at the top of the figure. Area with coseismic slip that exceeds the scale of the applied colour coding is indicated additionally and the corresponding value is given.

former rupture zones are much smaller than their vicinity. The higher coseismic slip occurred in the 3rd earthquake can be associated with the larger size of the rupture zone that might

determine the magnitude of the earthquake (Kanamori, 1986; Donald et al., 1994). However, this can be also interpreted as release of accumulated stress at a remained locked area. Stress release as function of time is indicated also in Fig. 3.28a, i.e. superimposing the maximum of cumulative slip at the centres of the 1st and 2nd earthquake rupture zones is close to the slip resulted from the 3rd earthquake at the rupture centre. Displacement patterns at the observation points on forearc surface also correspond to the above findings. As shown in Fig. 3.28b, coseismic displacements at the centres of the two small rupture zones are obviously smaller at the 3rd earthquake. Similar to the "Maule type" and the 3-D reference models, slips in opposite senses can be seen in Fig. 3.27. This phenomenon may imply on other mechanisms for coseismic stress release occurring in an environment that the applied models represent.
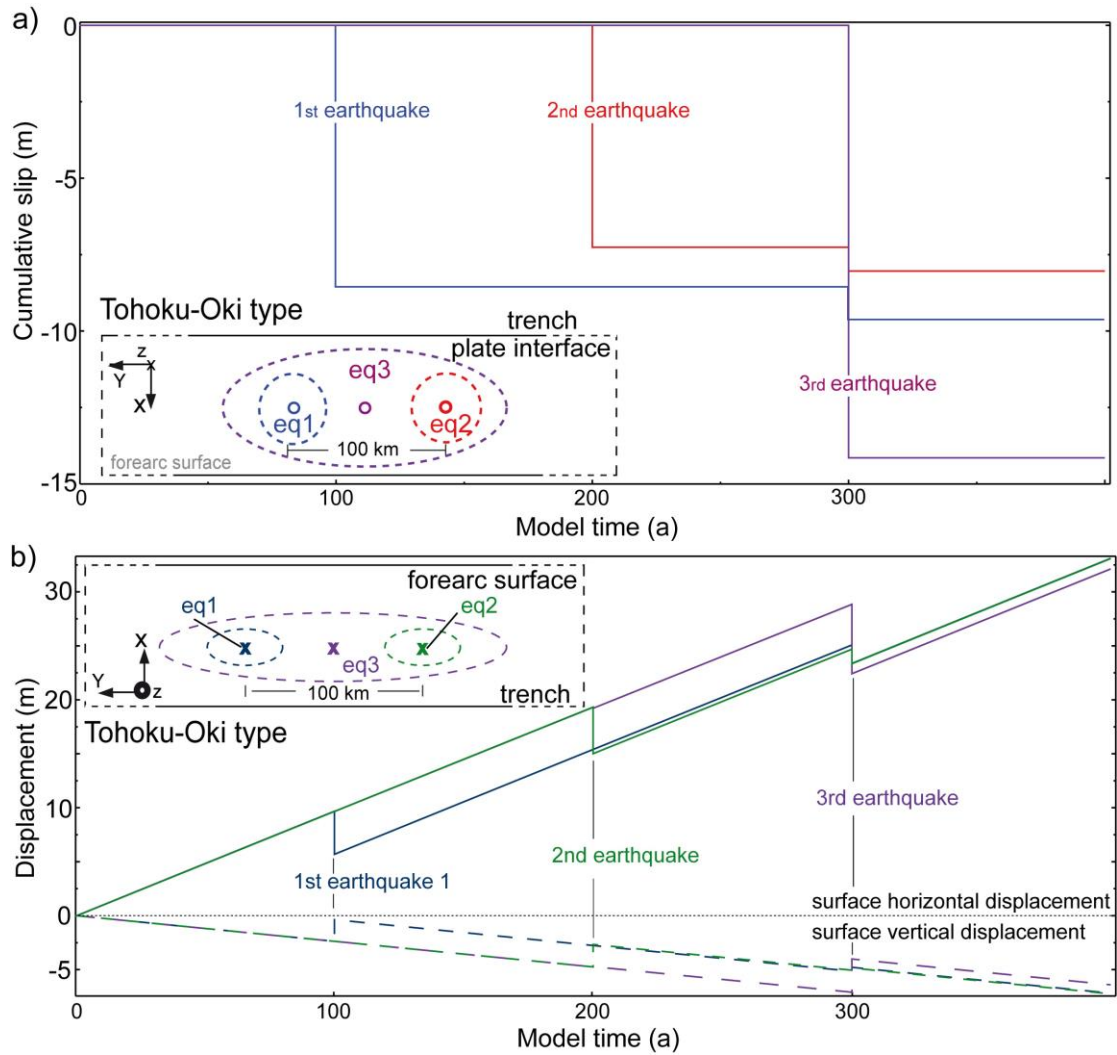

Figure 3.28 Time evolution of a) slip on the plate interface and b) displacements of the forearc surface at selected points of the "Tohoku-Oki type" model. In a): sketch of map view of the plate interface shows positions of the observation points. Each point locates at the geometry centre of each seismogenic zone, of which the results are shown by lines with same colour of the observation points. In b): sketch of map view of forearc surface illustrating positions of the observation points with crosses, which locate at the forearc surface above the projected centre of seismogenic zone for the 1st, 2nd and the 3rd earthquake, respectively. The results are shown by lines with same colour of the observation points, and coseismic displacements are shown with broken lines.

The model results demonstrate mainly elastic strain accumulation and subsequent release in different seismogenic zones within relatively short timescale. This is indicated by the deformation patterns shown in Fig. 3.28b. The 1st and 2nd earthquakes were simulated as foreshocks for the later large earthquake. Occurrences of sequences of foreshock are one of main features for the Tohoku-Oki earthquake. As reported by Tajima et al., (2013), a M_w 7 event occurred on March 9 off the coast of the Miyagi-prefecture, which turned out to be the foreshocks to the March 11 event and initiated the rupture sequence. They observed that the tectonic stress levels became close to the maximum shear strength for these zones and promoted complex rupture propagation through the broad region producing the huge M_w 9 event. Kato et al. (2012) recognized two distinct foreshock sequences migrating in the trench-parallel direction toward the epicentre of the main shock. They pointed out that the first sequence of slow slip in the Tohoku-Oki focal region may have weakened the plate interface of the later ruptured area by the great M_w 9 earthquake, and the subsequent sequence of slow slip may have caused stress loading onto the hypocentre of the main shock (see also Hori and Miyazaki, 2011). Also, repeating rupture of same asperities is also a common feature of the study area (Pollitz et al., 2011), and this was also realized in present model, i.e. both small seismogenic zones are unlocked (ruptured) again in the 3rd earthquakes. It is shown in the total surface horizontal displacement (Fig. 3.29b) that convergence dominates the displacement field in preseismic and subsequent interseismic phases, i.e. the patterns and magnitudes of displacement are similar. In the 1st and 2nd earthquake, coseismic displacements of the forearc surface occur mainly above the individual seismogenic zone. However, in the 3rd earthquake, strong displacements concentrate mainly at the area above the centre of the large seismogenic zone but reduce toward the area above the former rupture zones. This implies that the earthquake magnitude is not fully dependent on the number of asperities that are ruptured consecutively, but rather on the stress state of the asperities. Therefore, attentions should be paid to asperities that have not been ruptured in previous events, when evaluating the seismic hazard of a region.

Due to the limitations of the current model setup, transient processes associated with foreshock events or transient changes in stress state of the plate interface cannot be fully realized in the simulations. After comparing the GPS data from January 2003 to January 2011, Ozawa et al. (2012) suggested that a series of subduction earthquakes and aseismic slip before the March 2011 Tohoku earthquake could decrease the coupling rate off the Tohoku region and became the percussive events for the large M_w 9.0 event. Therefore, including aseismic slip, afterslips and postseismic slip into the modelling studies can be considered as improvements for the future work.

There are other efforts on understanding the generation of Tohoku-Oki earthquake. Wang et al. (2012) determined a 3-D seismic model of the north-eastern Japan forearc region using P- and S-wave arrival times from more than 2000 local earthquakes, from which they observed strong interplate coupling in the main-shock source area of the 2011 Tohoku-Oki earthquake but weak coupling in the surrounding areas. They attributed the generation of this earthquake and subsequent aftershocks to the fluid extrusion into the rupture zone due to the dehydration of the subducting plate, which increased the pore pressure and reduced the frictional strength

in the fault zone (see also Wallace et al., 2012); moreover, a higher Poisson ratio in the main-shock area was also indicated in their study.
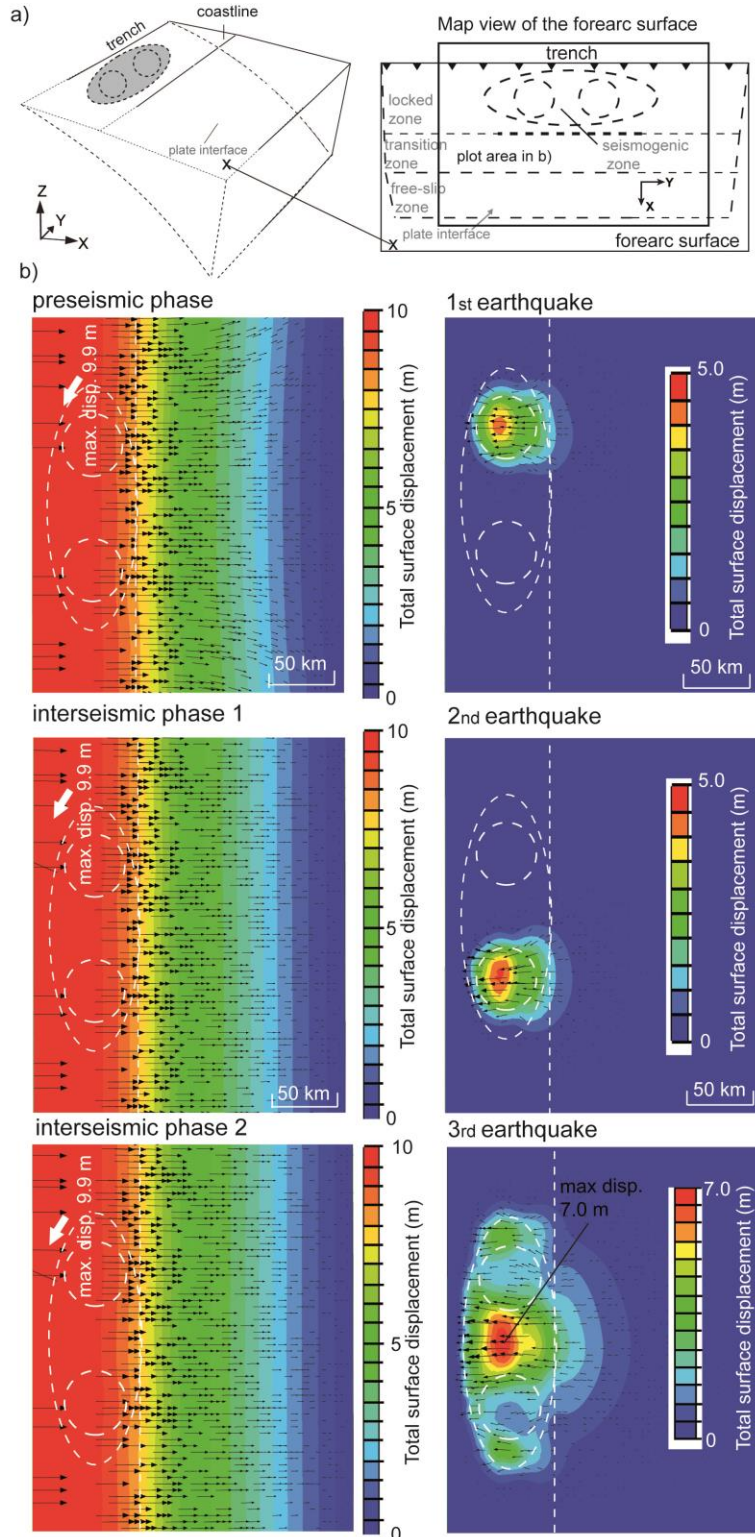

Figure 3.29 Calculated total surface horizontal displacement for the "Tohoku-Oki type" model. The map view of the observed area is illustrated by the sketch in a) and the results in different phases are shown in b). The displacement vectors are shown with colour coding and arrows, which indicates the direction of the vectors. The positions of the seismogenic zones projected on the forearc surface are denoted with white ellipses and the upper limit of the transition zone is indicated with white broken line. Maximum values of coseismic displacement in each earthquake are given.

3.4.4 Conclusions of this study

The following can be concluded from this study:

- Variations in friction coefficient of the seismogenic zone can affect the magnitude of coseismic displacements;

- Variations in down-dip limit can affect both the magnitude and spatial distribution of the upper plate deformation in pre-, co- and interseismic periods;

- Estimations on deformation rates can be different between 2-D and 3-D models by including lateral components of a subduction zone. Therefore, attentions must be given in case the applied models need to be calibrated with observed data;

- The resulting magnitudes and patterns of the slip and displacement of a large subduction earthquake can be affected by the spatiotemporal distributions of previous earthquake events.

4. Discussion

Subduction zone are defined as zones of convergence between two plates. Seismic cycles of the subduction zones, particularly the occurrence of large subduction earthquakes, however, are closely related to their seismic histories and current tectonic stress states (Wang and He, 1999; Heuret et al., 2012; Wallace et al. 2012; Wang et al., 2012). In this thesis, other factors that may provide second-order controls on the deformations of the upper plate (Fig. 4.1), such as climate-induced surface load changes, heterogeneous friction as well as the geometries of the seismogenic plate interface, are examined and the impact are quantified by means of numerical models. Also, the influences of these parameters on the seismic cycle of the subduction zone are discussed in the individual chapters.
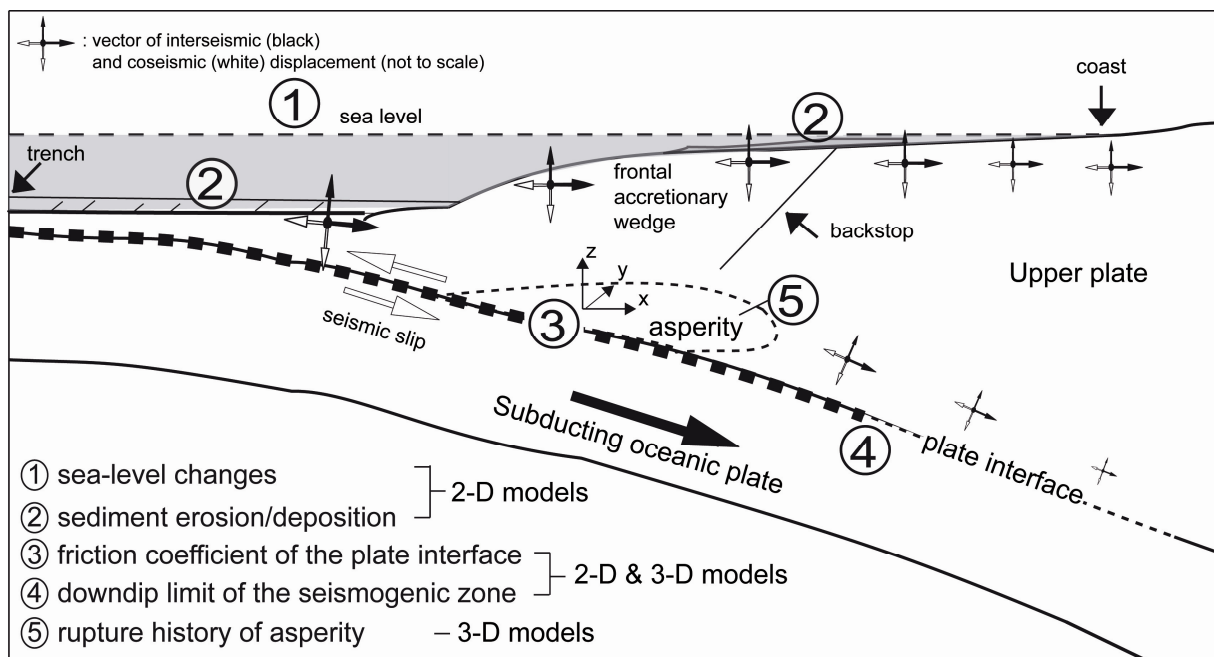

Fig. 4.1 Schematic map showing the main components considered in this thesis (not to scale).

4.1 Effects of glacial-interglacial surface loads on deformation and seismicity of the subduction zones

Glacial isostatic adjustment has been long recognized as one of the processes, which may contribute to crustal deformation (e.g. Cohen et al., 1993; Sauber, et al., 2000). Sauber and Molnia (2004) revealed in Alaska that a thin lithosphere may rapidly respond to short duration of advances and retreat of glaciers with land uplift and subsidence varying over short distances. Glacial fluctuations can also lead to eustatic sea level as well as sediment flux changes at plate boundaries (Imbrie et al., 1983; Peltier and Fairbanks, 2006; Inman et al., 2008). Such variations may modulate the stress field of the plate boundary and therefore the seismicity of subduction thrusts. For example, realising the potential relationship between trench sediments and subduction earthquakes, Heuret et al. (2012) statistically analysed

dataset of trench fill thickness and upper plate strain for 44 segments of the subduction zone worldwide. They found that the spatial patterns of giant earthquakes ($M_w \geq 8.5$) coincide with large trench fill thickness (> 1 km) and neutral upper plain strains, whereas environments with thin trench fills (< 0.5 km) and extensional upper plate strain appear to be unfavoured for high magnitude events. For investigating such impact, the Chilean margin is one of the ideal areas due to its along-strike variability in palaeo-climate and sedimentary histories (Lamy, et al., 1999, 2003; Montgomery et al., 2001; Hebbeln et al., 2007). Based on the sea-level and sedimentation-rate changes (e.g. Imbrie et al., 1984; Covault et al., 2010; Inman, 2008; Blumberg et al., 2008), the modelling in this thesis investigated the capability of climate-induced loading and unloading on perturbing the local stress regime of the upper plate and the influence on the seismic cycle of the subduction thrust.

The 2-D finite element model examined the sea-level variations in 120 ka, which assumes a linear decrease of 120 m in 100 ka and a subsequent increase in 20 ka (Imbrie et al., 1983). The resulting rates of vertical and horizontal displacements at the forearc are in some mm/ka, which appears to underestimate the actual glacial-interglacial deformation. However, taking into account that the observed post-LGM sea level may rise with an average rate of 12 m/ka and even up to 30 m/ka in the late Pleistocene (Bard et al. 1990; Peltier and Fairbanks, 2006), the resulting displacement can be more significant. The model results also show strongest displacement and shear stress changes below the coast. This is consistent with the results from semi-analytical flexural modelling (Luttrell and Sandwell, 2010), which demonstrated that the flexural stresses induced by eustatic sea-level variations are highest near the coast. Furthermore, derived by the large Coulomb stress changes on the fault segment below the coastline, the risk of seismic slip in this area can increase during sea-level fall but decrease during sea-level rise.

Strong variations of sediment flux between the on- and offshore areas may further enhance the deformation of the forearc (Bourgois et al., 2000; Adam, 2004). For example, in south-central Chile, mean sedimentation rate during the last glacial period was estimated to be more than 10 times higher than in Holocene (Blumberg et al., 2008). This glacial-interglacial sediment deposition rates has been converted into linear stress changes and implemented on the modified model based on the study on sea-level changes. Model results show that the enhanced glacial sediment transport from continental shelf to trench by sea-level drop increases uplift in the continental shelf but decreases at the trench. As a consequence, the Coulomb stress increases more significantly at the continental shelf than the trench, and this may indicate higher risk of seismic slip beneath the continental shelf. Note that the examined scenario of high glacial deposition at trench during sea-level fall is only one of the systems for continental-margin deep-see depositions in millennial scale revealed by Covault and Graham (2010). Focusing on the timescale of 10^6-10^7 a, Lamb and Davis (2003) have proposed that the dynamics of subduction and mountain-building in the Andes were controlled by processes of erosion and sediment depositions, because the central Andes can be elevated by high shear stresses at plate boundary due to scarcity of subducted sediments. They also associated the two large M9 earthquakes in Chile (1960) and Alaska (1964) with the subducted trench sediments that may lubricate the plate interface (with their high water content and finer grain

size) and allowed wider propagation of the earthquake, which was also supported by Melnick et al. (2009) based on their study on heterogeneous seismic coupling along the Chilean margin. Subduction of sediment trench fill are beyond the scope of this thesis, however, their mechanical impacts on plate interface friction can be indicated from the impacts of varying frictional properties along the plate interface, which will be discussed in following sections. Although the examined scenarios for glacial-interglacial sea-level change as well as sediment redistributions are simplified in this thesis, the variations of loads are evaluated within a complex model domain and the impacts have been resolved on timescale of $10^{3\text{-}}10^4$ a. The model results provide new insights on the short-term mechanical responses of the subduction zones to the above climate-induced load changes.

4.2 Variations of physical properties along plate interfaces

Investigations were also carried out in this thesis on the heterogeneity of subduction zones. For example, segmentations of the thrust interface occur in both dip and along- strike directions at convergent margins (e.g. Melnick et al., 2009). Distribution and rupture histories of the asperities may strongly influence the coupling of subduction zones over seismic cycles (Scholz and Campos, 2012 and reference therein). These heterogeneities have been parameterized in previous modelling work (e.g. Masterlark et al., 2001; Masterlark, 2003; Hu et al., 2004; Cailleau and Oncken, 2008; Kato and Yoshida, 2011) and evaluated with respect to their influence on seismic plate coupling and seismic cycles. In this thesis, variations in frictional properties were investigated by varying friction coefficients along the plate interface (Fig. 4.1). The models are simulated by prohibiting slip at the seismogenic zone, and stresses are accumulated as the upper plate accommodates the subduction of the rigid plate and then released from subsequent earthquake as slip is allowed at the seismogenic zone. Stable slip is allowed in transition zone by giving a moderate friction coefficient (0.3) and no friction is applied at the free-slip zone. By this mean, variations of displacement and stress fields during this model seismic cycle are subjected to the changes in value of friction coefficient. The model results show high sensitivity to coseismic friction of the seismogenic zone in both stress and displacement, i.e. significant enhancement on coseismic deformations can be seen as coseismic friction decreases. As previously indicated, subducted trench-fill sediment may reduce basal friction of the plate interface and also allow wider propagation of earthquake, which is attributed to the high coseismic fault slips and consequently large earthquakes in Alaska (1964), Valdivia (Chile 1960) and also Tohoku-Oki (Japan 2011) (Lamb and Davis, 2003; Moreno et al., 2009; Lay et al., 2012; Zhao et al., 2011). The described coseismic model responses to varying friction coefficients agree with previous studies. Furthermore, it has been observed a full interseismic coupling prior to the 2010 Maule earthquake in central Chile (Ruegg et al., 2009; Scholz and Campos, 2012). This finding is also derived from the model results, in which higher displacement rates are shown in interseismic phase relative to the preseismic rates. Note that extending the above investigations on the friction coefficient to 3-D models resulted in similar trends on the changes in displacements.

The length of seismogenic zones is also frequently reported as a crucial factor on subduction earthquakes (Hyndman and Wang, 1995; Wang and He, 1999; Hu et al., 2004; Trubienko et al., 2013). This factor was tested in this thesis by fixing the updip of the seismogenic zone to the trench whilst varying the downdip limit of the seismogenic zone in different models (see Fig. 4.1). The model results show the positions of the downdip limit of the seismogenic zone may constrain the locations of the upper plate where strong preseismic and interseismic deformations occur. Interestingly, a shallow seismogenic zone (~5 km deep) can result in similarly magnitude of coseismic deformation in the forearc surface and plate interface as derived by the 2-D model. However, a clearer correlation can be seen in the 3-D models as the coseismic slip reduces as seismogenic zone becomes shallower. This difference implies that the along-strike component of the seismogenic zone is able to attenuate the accumulated stress in lateral directions. However, recent observations after the 2011 Tohoku-Oki earthquake revealed that large coseismic slip extended to the trench axis (Kodaira et al., 2012), which is contradictory to the opinion that the accretionary wedge slip mostly aseismically (Tajima et al., 2013). Therefore, attention should be given on the present 2-D and 3-D model results of the shallow seismogenic zone, as previous models usually assumed no stress accumulation at the toe of the thrust concerning the weak material strength and lateral component of the seismogenic zone is not included (e.g. Wang and Hu, 2006).

The aforementioned parameters are also evaluated with 3-D models by including the along-strike extension of the subduction zones. The 3-D predicted deformation patterns are generally in agreement with the 2-D models, except the magnitude of displacement observed on trench-normal direction of the 3-D models are generally smaller due to the attenuations in lateral directions. The 3-D models also indicate divergent vectors of coseismic surface displacement in the area coincident to the edges of the seismogenic zone. These patterns can be crucial for characterizing the lithospheric properties for the fault zones as suggested by Hampel et al. (2013). Furthermore, coseismic slips in opposite direction are shown in the 3-D reference model, i.e. slip in similar magnitude as the trenchward slip but in sense of convergence occurs at the lower segment of the seismogenic zone. However, this slip is only found in the case of a deepest seismogenic zone and with lowest coseismic friction, which are the setup of the 3-D reference model. This observation is so far not reported in any other studies and this anomaly cannot be solved by refinement of the model domain or using a homogenous model domain. Therefore, open questions arise on the existence of unknown coseismic slip patterns on the plate interface.

Additional 3-D models with more earthquakes in order to study the generations of the 2010 Maule (Chile) and 2011 Tohoku-Oki (Japan) earthquakes (see Fig. 4.1). In the Maule-type earthquakes, similarly strong coseismic slips occur in two separate earthquakes at their individual rupture zone. However, the overlapping zone experiences much less coseismic slip in the second earthquake and acts as a barrier which stops the propagation of seismic slip into the rupture zone of the previous earthquake. This is in agreement with the low seismicity observed beneath the Arauco peninsular locating between the Valdivia and Maule segments, which the former one has been almost thoroughly ruptured in the 1960 Valdivia ($M_w = 9.5$) earthquake. In the Tohoku-Oki type earthquakes, the model results show that the rupture of

two smaller asperities after another in two different earthquakes may not significantly influence the maximum slip of the previous intake area within the large seismogenic zone for the third earthquake. The maximum coseismic slip of the large seismogenic zone is approximately the superposition of the individual maximums from the previous two earthquakes. The applied model may not adequately represent the observed dynamic patterns by Ozawa et al. (2012) that a sequent of M7 earthquakes may instabilize the rupture zone of the later M_w 9 Tohoku-Oki earthquake, which is similar to the finding by Kato et al. (2012) on the propagation of slow slip events towards the epicentre of the main shock. However, the model results provide insights on the behaviour of asperities throughout a few seismic cycles, based on a mechanical point of view. Some similarities are shared with the two different types of earthquake sequences: 1) the large earthquake can be correlated with the size of the rupture area or the number of ruptured asperities but more closely to the stress state of the asperity, i.e. the amount of accumulated stress that has been released in the previous earthquakes and the current state of stress accumulations; 2) the interseismic coupling rate of the asperities may not be affected during the seismic cycles, which is indicated by the unchanged displacement rate at the centre of the asperities before and after the earthquakes. According to Scholz and Campos (2012) based on their reviews on the earthquakes in Japan, Cascadia and south Chile, they found that the strong coupling is a permanent feature of asperities, which controls the slip accumulation rate but does not define the net accumulation of slip deficits. Overall, the above findings may contribute to better understanding on accessing the risks of seismic hazards from large earthquakes.

4.3 Numerical modelling on subduction zones in this thesis

The applied 2-D finite-element model with surface load variations allows resolving the resulting spatial variations in displacement and stress along the convex contact between the bended oceanic plate and the continental plate. This is already more advanced in comparison to previous models that the subduction thrust is approximated with a plane of constant dip (e.g. Luttrell and Sandwell, 2010). Furthermore, including the bending stresses of the subducting plate into the investigations on the influence of surface load changes (Chapter 2) is important, which can improve the estimations on the changes in stress field of the upper plate. Nevertheless, shortcomings of the applied approach in Chapter 2 exist mainly on the application of simplified scenarios of glacial-interglacial variations of sea level and sediment deposition for sake of computational feasibility. Also, transient load changes as well as plate convergent cannot be implemented with the current models, which is mostly owing to the difficulties on combining surface load changes with strong crustal deformation. This problem may be substantially improved by coupling the landscape evolution models to the present models. Viscoelastic behaviour is not considered for the examined scenario on timescale of 10^3-10^4 years, but can be crucial for long-term deformation.

Compared to previous modelling work, the accomplished parameter studies involved the influences of viscoelastic materials by using layered stratified model lithosphere, which avoided the oversimplifications that may happen by using a homogenous elastic half space

(e.g. Masterlark et al., 2001; Masterlark, 2003; Hu et al., 2004). In this thesis, the applied model settings included the main features of subduction zone in terms of geometry and boundary conditions, but they are still simplified in comparison to the natural seismotectonic settings of the subduction zones. As techniques of seismological and geodetical methods advance and provide more detailed insight into the architecture of the plate boundary, more accurate constrains for modelling on specific regions will become available in the future.

5. Conclusions and outlook

In the framework of this thesis, different 2-D and 3-D finite-element models were applied to evaluate the impact of surface load changes and variations on frictional properties as well as the geometry of the seismogenic zone on the seismic cycle of subduction zones. Investigations on the impact of surface load changes are carried out with 2-D finite-element models. The model results show that sea-level changes are able to affect the deformation in the forearc and the state of stress along the seismogenic part of the plate interface. During sea-level fall, seismic slip of the plate interface may be promoted, whereas it may be delayed by a rising sea level. With the pure elastic model domain, additional load variations from the glacial-interglacial surface sediment erosion and sedimentation are superimposed on the effect of the sea-level changes. The model results show that during the phase with strong glacial sediment transportation between the continental shelf and the trench, uplift is enhanced at the continental shelf where seismic slip is further promoted at the plate interface beneath. In contrast, uplift is reduced at the toe of the forearc and the seismic slip of the plate interface between trench and continental shelf can be delayed. However, when the sediment flux is significantly reduced during the interglacial period, the influences from sediment are overwhelmed by the impacts from the rapid rising sea level.

Systematic parameter studies show that variations in friction coefficient of the seismogenic zone mainly affect the magnitude of coseismic displacements, whereas variations in down-dip limit can affect both the magnitude and spatial distribution of the deformations in pre-, co- and interseismic period. Same parameters are examined by applying 3-D models, in which lateral components of a subduction zone are included. The estimated trends in changing on deformation rates and patterns from the varying parameters are similar between the 2-D and 3-D models, whereas notable differences appear mainly in the magnitudes of coseismic deformations. Therefore, attentions must be given if the models are meant to work with observed data. Moreover, case studies on two different types of earthquake sequences before the main shocks of Maule 2010 (Chile) and Tohoku-Oki 2011 (Japan) reveal that the generations of large subduction earthquake ($M_w > 8.5$) are not only closely related to the seismotectonic settings of the subduction zones, but also to their seismic histories with respect to the magnitudes as well as the spatiotemporal distributions of previous earthquake events.

Future modelling for studying on the impacts of surface load changes should concern also the viscoelastic deformations from surface load changes on longer timescales (10^5-10^6). Moreover, plate convergences should be included in a future model. Furthermore, in order to implement transient changes of erosion and sedimentation rates in the models, coupled landscape evolution models (e.g. with CASQUS, see Kurfeß and Heidbach, 2009) are needed. Also, the lateral variations on surface loads should be also included in 3-D models. With respect to the studying on the deformation and seismic cycles at subduction zones, further constrains with observed data on geometries, rheologies and boundary conditions of the models are necessary. Also, spherical subduction zone models could be applied as suggested from more recent studies (e.g. Hu and Wang, 2012; Trubienko, et al. 2013). Moreover,

surface processes should be included in the models that investigate subduction earthquakes. Further efforts are needed on developing geochemical-thermo-mechanical subduction zone models, in order to continuously improve our knowledge on subduction earthquakes and seismic risk assessment.

Acknowledgement

References

Adam, J., Kläschen, D., Kukowski, N., Flüh, E., 2004. Upward delamination of Cascadia Basin sediment infill with landward frontal accretion thrusting caused by rapid glacial age material flux. Tectonics 23, TC3009. doi:10.1029/2002TC001475.

Aron, F., Allmendinger, R.W., Cembrano, J., González, G., Yáñez, G., 2013. Permanent fore-arc extension and seismic segmentation: Insights from the 2010 Maule earthquake, Chile. J. Geophys. Res. 118, 724-739. doi:10.1029/2012JB009339.

Bangs, N., Cande, S.C., 1997. Episodic development of a convergent margin inferred from structures and processes along the southern Chile margin. Tectonics 16, 489-503.

Bard, E., Hamelin, B., Fairbanks, R.G., Zindler, A., 1990. U-Th ages from mass spectrometry in corals from Barbados: sea level during the past 130,000 years. Nature 346, 456-458.

Barrientos, S.E., Plafker, G., 1992. Postseismic coastal uplift in southern Chile. Geophys. Res. Lett. 19, 701-704.

Beaumont, C., Fullsack, P., Hamilton, J., 1992. Erosional control of active compressional orogens. In: McClay, K.R. (Ed.), Thrust Tectonics, Chapman and Hall, London, pp. 1-18.

Becerra, J., Contreras-Reyes, E., Arriagada, C., 2013. Seismic structure and tectonics of the southern Arauco Basin, south-central Chile (~38°S). Tectonophysics 592, 53-66. doi:dx.doi.org/10.1016/j.tecto.2013.02.012

Bilek, S.L., Lay, T., 1998. Variation of interplate fault zone properties with depth in the Japan subduction zone. Science 281(5380), 1175-1178.

Blumberg, S., Lamy, F., Arz, H.W., Echtler, H.P., Wiedicke, M., Haug, G.H., Oncken, O., 2008. Turbiditic trench deposits at the South-Chilean active margin: A Pleistocene–Holocene record of climate and tectonics. Earth Planet. Sci. Lett. 268, 526-539. doi:10.1016/j.epsl.2008.02.007.

Bourgois, J., Guivel, C., Lagabrielle, Y., Calmus, T., Boulegue, J., Daux, V., 2000. Glacial-interglacial trench supply variation, spreading-ridge subduction, and feedback controls on the Andean margin development at the Chile triple junction area (45-48°S). J. Geophys. Res. 105, 8355-8386.

Brooks, B.A., Bevis, M., Smalley, R.Jr., Kendrick, E., Manceda, R., Lauría, E., Maturana, R., Araujo, M., 2003. Crustal motion in the southern Andes (26–36 S): Do the Andes behave like a microplate?. Geochem. Geophys. Geosyst. 4(10), 1085. doi:10.1029/2003GC000505.

Buiter, S.J.H., Govers, R., Wortel, M.J.R., 2001. A modelling study of vertical surface displacements at convergent plate margins. Geophys. J. Int. 147, 415-427.

Burov, E., Toussaint, G., 2007. Surface processes and tectonics: forcing of continental subduction and deep processes. Global and Planetary Change 58, 141-164.

Bürgmann, R., Kogan, M.G., Steblov, G.M., Hilley, G., Levin, V.E., Apel, E., 2005. Interseismic coupling and asperity distribution along the Kamchatka subduction zone. J. Geophys. Res. 110, B07405. doi: 10.1029/2005JB003648.

REFERENCES

Cailleau, B., Oncken, O., 2008. Past forearc deformation in Nicaragua and coupling at the megathrust interface: Evidence for subduction retreat?. Geochem. Geophy. Geosy. 9, Q03016. doi:10.1029/2007GC001754.

Chappell, J., Shackleton, N.J., 1986. Oxygen isotopes and sea level. Nature 324, 137-140.

Chlieh, M., Avouac, J.P., Hjorleifsdottir, V., Song, T.A., Ji, C., Sieh, K., Sladen, A., Hebert, H., Prawirodirdjo, L., Bock, Y., Galetzka, J., 2007. Coseismic slip and afterslip of the great (Mw 9.15) Sumatra-Andaman earthquake of 2004. Bull. Seismol. Soc. Am. 97, 152-173.

Chlieh, M., Avouac, J.P., Sieh, K., Natawidjaja, D.H., Galetzka, J., 2008. Heterogeneous coupling of the Sumatran megathrust constrained by geodetic and paleogeodetic measurements. J. Geophys. Res. 113, B05305. doi: 10.1029/2007JB004981.

Church, M., Slaymaker, O., 1989. Disequilibrium of Holocene sediment yield in glaciated British Columbia, Nature 337, 452-454.

Clift, P.D., 2006. Controls on the erosion of Cenozoic Asia and the flux of clastic sediment to the ocean. Earth Planet. Sci. Lett. 241, 571-580.

Cochran, E.S., Vidale, J.E., Tanaka, S., 2004. Earth tides can trigger shallow thrust fault earthquakes. Science 306, 1164-1166.

Cohen, S.C., 1993. Does rapid change in ice loading modulate strain accumulation and release in glaciated, tectonically active regions?. Geophys. Res. Lett. 20, 2123-2126.

Cohen, S.C., 1999. Numerical models of crustal deformation in seismic zones. Adv. Geophys. 41, 133-231.

Contardo, X.J., Kukowski, N., Cembrano, J.M., 2011. Material transfer and its influence on the formation of slope basins along the South Central Chilean convergent margin: Insights from scaled sandbox experiments. Tectonophysics 513(1-4), 20-36.

Contreras-Reyes, E., Flueh, E.R., Grevemeyer, I., 2010. Tectonic control on sediment accretion and subduction off south central Chile: Implications for coseismic rupture processes of the 1960 and 2010 megathrust earthquakes. Tectonics 29, TC6018. doi: 10.1029/2010TC002734.

Covault, J.A., Graham, S.A., 2010. Submarine fans at all sea-level stands; tectono-morphologic and climatic controls on coarse-grained sediment delivery to the deep sea. Geology 38, 939-942.

Covault, J.A., Romans, B.W., Graham, S.A., Fildani, A., Hilley, G.E., 2011. Terrestrial source to deep-sea sink sediment budgets at high and low sea levels: Insights from tectonically active Southern California. Geology 39, 619-622. doi:10.1130/G31801.1.

Darwin, C., 1851. Geological Observation on Coral Reefs, Volcanic Islands and on South America, Smith Elder, London.

Denton, G.H., Heusser, C.J., Lowell, T.V., Moreno, P.I., Andersen, B.G., Heusser, L.E., Schlüchter, C., Marchant, D.R., 1999. Interhemispheric linkage of paleoclimate during the last glaciation. Geografiska. Annaler. 81A(2), 107-153.

Dragert, H., Hyndman, R.D., Rogers, G.C., Wang, K., 1994. Current deformation and the width of the seismogenic zone of the norther cascadia subduction thrust. J. Geophys. Res. 99(B1), 653-668.

Dragert, H., Hyndman, R.D., 1995. Continuous GPS monitoring of elastic strain in the northern Cascadia subduction zone. Geophys. Res. Lett. 22, 755-758.

REFERENCES

Gery, T.V., Meilick, F.I., 2011. Geodynamic regimes of subduction under an active margin: effects of rheological weakening by fluids and melts. J. Metamorph. Geol. 29, 7–31. doi: 10.1111/j.1525-1314.2010.00904.x.

Gerya, T., 2011, Future directions in subduction modeling. J. Geodyn. 52, 344–378. doi:10.1016/j.jog.2011.06.005.

Gerya, T.V., Stöckhert, B., 2005. Two-dimensional numerical modeling of tectonic and metamorphic histories at active continental margins. Int. J. Earth Sci. 95, 250-274. doi: 10.1007/s00531-005-0035-9.

Gray, R., Pysklywec, R.N., 2012. Influence of sediment deposition on deep lithospheric tectonics, Geophys. Res. Lett. 39, L11312. doi:10.1029/2012GL051947.

Hallet, B., Hunter, L., Bogen, J., 1996. Rates of erosion and sediment evacuation by glaciers: A review of field data and their implications. Global Planet. Change 12, 213-235.

Hampel, A., Li, T., Maniatis, G., 2013. Contrasting strike-slip motions on thrust and normal faults: Implications for space-geodetic monitoring of surface deformation. Geology 41, 299-302. doi: 10.1130/G33927.1.

Hampel, A., Pfiffner, A., 2006. Relative importance of trenchward upper plate motion and friction along the plate interface for the topographic evolution of mountain belts, in: Analogue and Numerical Modelling of Crustal-Scale Processes. In: Buiter, S. J. H., Schreurs, G. (Eds.), Geol. Soc. London Spec. Publ. 253, 105-115.

Hanks, T.C., 1977. Earthquake stress drops, ambient tectonic stresses and stresses that drive plate motions. Pure Appl. Geophys. 115, 441-458.

Hebbeln, D., Lamy, F., Mohtadi, M., Echtler, H., 2007. Tracing the impact of glacial-interglacial climate variability on erosion of the southern Andes. Geology 35(2), 131-134.

Heuret, A., Conrad, C.P., Funiciello, F., Lallemand, S., Sandri, L., 2012. Relation between subduction megathrust earthquakes, trench sediment thickness and upper plate strain. Geophys. Res. Lett. 39, L05304. doi:10.1029/2011GL050712.

Hippchen, S., Hyndman, R.D., 2008. Thermal and structural models of the Sumatra subduction zone: Implications for the megathrust seismogenic zone. J. Geophys. Res. 113, B12103.

Hori, T., Miyazaki, S., 2011. A possible mechanism of M 9 earthquake generation cycles in the area of repeating M 7~8 earthquakes surrounded by aseismic sliding. Earth Planets Space 63, 773-777.

Hu, Y., Wang, K.L., 2012. Spherical-Earth finite element model of short-term postseismic deformation following the 2004 Sumatra earthquake, J. Geophys. Res. 117. doi:10.1029/2012JB009153

Hu, Y., Wang, K.L., He, J., Klotz, J., Khazaradze, G., 2004. Three-dimensional viscoelastic finite element model for post-seismic deformation of the great 1960 Chile earthquake. J. Geophys. Res. 109, B12403.

Hyndman, R.D., Wang, K.L., 1995. The rupture zone of Cascadia great earthquakes from current deformation and the thermal regime. J. Geophys. Res. 100, B11, 22133-22154.

Hyndman, R.D., Wang, K.L., Yamano, M., 1995. Thermal constraints on the seismogenic portion of the southwestern Japan subduction thrust, J. Geophys. Res. 100(B8), 15373-15392. doi:10.1029/95JB00153.

Imbrie, J., Hays, J.D., Martinson, D.G., Mcintyre, A., Mix, A. C., Morley, J.J., Pisias, N.G.,

Prell, W.L., Shackleton, N.J., 1984. The orbital theory of Pleistocene climate: Support from a revised chronology of the marine record. In: Berger, A. L., Imbrie, J., Hays, J., Kukla, G., Saltzman, B. (Eds.), Milankovitch and Climate, Part 1, Reidel, Boston, pp. 269-305.

Inman, D.L., 2008. Highstand fans in the California borderland: COMMENT and REPLY: COMMET. Geology 36, e166. doi: 10.1130/G24626C.1.

Ivins, E.R., James, T.S., 2004. Bedrock response to Llanquihue Holocene and present-day glaciation in southernmost South America. Geophys. Res. Lett. 31, L-24613. doi:10.1029/2004GL021500.

Kanamori, H., 1986, Rupture process of subduction-zone earthquakes. Annu. Rev. Earth Pl. Sc. 14, 293-322.

Kanamori, H., Anderson, D.L., 1975. Theoretical basis of some empirical relations in seismology. Bull. Seismol. Soc. Am. 65, 1073-1095.

Kanamori, H., Miyazawa, M., Mori, J., 2006. Investigation of the earthquake sequence off Miyagi prefecture with historical seismograms. Earth Planets Space 58, 1533-1541.

Kanda, R.V.S., Simons, M., 2010. An elastic plate model for interseismic deformation in subduction zones. J. Geophys. Res. 115, B03405. doi:10.1029/2009JB006611.

Kasahara, J., 2002. Tides, earthquakes and volcanoes. Science 297, 348-349.

Kato, N., 2008. Numerical simulation of recurrence of asperity rupture in the Sanriku region, northeastern Japan. J. Geophys. Res. 113, B06302. doi:10.1029/2007JB005515.

Kato, A., Obara, K., Igarashi, T., Tsuruoka, L., Nakagawa, S., Hirata, N., 2012. Propagation of slow slip leading up to the 2011 M_w 9.0 Tohoku-Oki earthquake. Science 335(6069), 705-708.

Kato, N., Yoshida, S., 2011. A shallow strong patch model for the 2011 great Tohoku-oki earthquake: A numerical simulation. Geophys. Res. Lett. 38, L00G04. doi:10.1029/2011GL048565.

Klotz, J., Angermann, D., Michel, G.W., Porth, R., Reigber, C., Reinking, J., Viramonte, J., Perdomo, R., Rios, V.H., Barrientos, S., Barriga, R., Cifuentes, O., 1999. GPS-derived deformation of the central Andes including the 1995 Antofagasta $M_w = 8.0$ earthquake. Pure Appl. Geophys. 154(3-4), 709-730.

Kodaira, S., No, T., Nakamura, Y., Fujiwara, T., Kaiho, Y., Takahashi, N., Kaneda, Y., and Taira, A., 2012. Coseismic fault rupture at the trench axis during the 2011 Tohoku-oki earthquake. Nature Geoscience 5, 646–650. doi:10.1038/ngeo1547.

Kurfeß, D., Heidbach, O., 2009. CASQUS - A new simulation tool for coupled 3D finite element modeling of tectonic and surface processes based on ABAQUSTM and CASCADE. Computers and Geosciences 35(10), 1959-1967.

Lamb, S., Davis, P., 2003. Cenozoic climate change as a possible cause for the rise of the Andes. Nature 425, 792.

Lamy, F., Hebbeln, D., Rohl, U., Wefer, G., 2001. Holocene rainfall variability in southern Chile: a marine record of latitudinal shifts of the Southern Westerlies. Earth Planet. Sci. Lett. 185(3-4), 369.

Lamy, F., Hebbeln, D., Wefer, G., 1999. High-resolution marine record of climatic change in mid-latitude Chile during the last 28,000 years based on terrigenous sediment parameters. Quaternary Res. 51(1), 83.

Lay, T., Ammon, C.J., Kanamori, H., Xue, L., Kim, M., 2011. Possible large near-trench slip

during the 2011 M_w 9.0 off the Pacific coast of Tohoku earthquake. Earth Planets Space, 63, 687-692.

Lay, T., Kanamori, H., Ammon, C.J., Koper, K.D., Hutko, A.R., Ye, L., Yue, H., Rushing, T. M., 2012. Depth-varying rupture properties of subduction zone megathrust faults. J. Geophys. Res. 117, B04311. doi:10.1029/2011JB009133.

Lay, T., Kanamori, H., Ruff, L., 1982. The asperity model and the nature of large subduction zone earthquakes. Earthquake Prediction Research 1. Terrapub, 3-71.

Li, T., Hampel, A., 2012. Effect of glacial-interglacial sea-level changes on the displacement and stress field in the forearc and along the plate interface of subduction zones. Solid Earth 3, 63-70. doi:10.5194/se-3-63-2012.

Lin, W., Conin, M., Moore, J., Chester, F., Nakamura, Y., Mori, J.J., Anderson, L., Brodsky, E., Eguchi, N., Expedition 343 scientists, 2013. Stress State in the Largest Displacement Area of the 2011 Tohoku-Oki Earthquake. Science 339 (6120), 687-690. doi: 10.1126/science.1229379.

Luttrell, K., Sandwell, D., 2010. Ocean loading effects on stress at near shore plate boundary fault systems. J. Geophys. Res. 115, B08411. doi:10.1029/2009JB006541.

Masterlark, T., 2003. Finite element model predictions of static deformation from dislocation sources in a subduction zone: Sensitivities to homogeneous, isotropic, Poisson-solid, and half-space assumptions. J. Geophys. Res. 108(B11), 2540. doi: 10.1029/2002JB002296.

Masterlark, T., DeMets, D., Wang, H.F., Sánchez, O., Stock, J., 2001. Homogeneous vs heterogeneous subduction zone models: Coseismic and postseismic deformation. Geophys. Res. Lett. 28(21), 4047-4050.

Matsuura, M., Sato, T., 1989. A dislocation model for the earthquake cycle at convergent plate boundaries. Geophys. J. Oxford 96(1), 23-32.

McCaffrey, R., 2008. Global frequency of magnitude 9 earthquakes. Geology 36, 263-266.

Melnick, D., Bookhagen, B., Strecker, M.R., Echtler, H.P., 2009. Segmentation of megathrust rupture zones from fore-arc deformation patterns over hundreds to millions of years, Arauco peninsula, Chile. J. Geophys. Res. 114, B01407. doi:10.1029/2008JB005788.

Melnick, D., Echtler, H.P., 2006. Inversion of forearc basins in south-central Chile caused by rapid glacial age trench fill. Geology 34, 709-712.

Métois, M., Socquet, A., Vigny, C., 2012. Interseismic coupling, segmentation and mechanical behavior of the central Chile subduction zone. J. Geophys. Res. 117, B03406. doi:10.1029/2011JB008736.

Montgomery, D.R., Balco, G., Willett, S.D., 2001. Climate, tectonics, and the morphology of the Andes. Geology 29, 579-582.

Moreno, M.S., Bolte, J., Klotz, J., Melnick, D., 2009. Impact of megathrust geometry on inversion of coseismic slip from geodetic data: Application to the 1960 Chile earthquake. Geophys. Res. Lett. 36, L16310.

Moreno, M., Melnick, D., Rosenau, M., Baez, J., Klotz, J., Oncken, O., Tassara, A., Chen, J., Bataille, K., Bevis, M., Socquet, A., Bolte, J., Vigny, C., Brooks, B., Rider, I., Grund, V., Smalley, B., Carrizo, D., Bartsch, M., Hase, H., 2012. Toward understanding tectonic control on the M_w 8.8 2010 Maule Chile earthquake. Earth Planet. Sc. Lett. 321-322, 152-165.

REFERENCES

Moreno, M., Melnick, D., Rosenau, M., Bolte, J., Klotz, J., Echtler, H., Baez, J., Bataille, K., Chen, J., Bevis, M., Hase, H., Oncken, O., 2011. Heterogeneous plate locking in the South-Central Chile subduction zone: Building up the next great earthquake. Earth and Planetary Science Letters 305(3-4), 413-424.

Moreno, M., Rosenau, M., Oncken, O., 2010. 2010 Maule earthquake slip correlates with pre-seismic locking of Andean subduction zone. Nature 467(7312), 198-202.

Nasu, N., Kishinouye, F., Kodaira, T., 1931. Recent seismic activities in the Idu Peninsula (Part I), Bull. Earthquake Res. Inst., Tokyo Imperial Univ. 9, 22-35.

Ozawa, S., Nishimura, T., Munekane, H., Suito, H., Kobayashi, T., Tobita, M., Imakiire, T., 2012. Preceding, coseismic, and postseismic slips of the 2011 Tohoku earthquake, Japan. J. Geophys. Res. 117, B07404. doi:10.1029/2011JB009120.

Ozawa, S., Nishimura, T., Suito, H., Kobayashi, T., Tobita, M., Imakiire, T., 2011. Coseismic and postseismic slip of the 2011 magnitude-nine Tohoku-Oki earthquake. Nature 475, 373–376. doi:10.1038/nature10227.

Peltier, W.R., Fairbanks, R.G., 2006. Global glacial ice volume and Last Glacial Maximum duration from an extended Barbados sea level record, Quat. Sci. Rev. 25, 3322-3337.

Pollitz, F., Brooks, B., Tong, X., Bevis, M., Foster, J., Bürgmann, R., Smalley, R., Vigny, C., Socquet, A., Ruegg, J.C., Campos, J., Barrientos, S., Parra, H., Soto, J., Baez, Cimbaro, S., Blanco, M., 2011. Coseismic slip distribution of the February 27, 2010 Mw 8.8 Maule, Chile earthquake. Geophys. Res. Lett. 38 (9). doi:10.1029/2011GL047065.

Posamentier, H.W., Erskine, R.D., Mutchum, R.M.Jr., 1991. Submarine fan deposition in a sequence stratigraphic framework. In: Weimer, P., Link, M.H. (Eds.), Seismic facies and sedimentary processes of submarine fans and turbidite systems, Springer-Verlag, New York, 127-136.

Ruegg, J.C., Rudloff, A., Vigny, C., Madariaga, R., Dechabalier, J., Campos, J., Kausel, E., Barrientos, S., Dimitrov, D., 2009. Interseismic strain accumulation measured by GPS in south central Chile seismic gap. Phys. Earth Planet. Inter. 175 (1-2), 78-85. doi:10.1016/j.pepi.2008.02.015.

Ruff, L.J., 1989. Do trench sediments affect great earthquake occurrence in subduction zones? Pageoph. 129 (1/2), 263-282.

Sauber, J., Molnia, B.F., 2004. Glacier ice mass fluctuations and fault instability in tectonically active Southern Alaska. Global Planet. Change 42, 279-293.

Sauber, J., Plafker, G., Molnia, B.F., Bryant, M.A., 2000. Crustal deformation associated with glacial fluctuations in the eastern Chugach Mountains, Alaska. J. Geophys. Res. 105, 8055-8077.

Sauber, J.M., Ruppert, N.A., 2008. Rapid ice mass loss: Does it have an influence on earthquake occurrence in southern Alaska?. In: Freymueller J.T., Haeussler, P.J., Wesson, R.L., Ekström, G. (Eds.), Active Tectonics and Seismic Potential of Alaska, Geophys. Monogr. Ser. 179, AGU, Washington, D.C., pp. 369-384. doi:10.1029/179GM21.

Savage, J.C., Plafker, G., 1991. Tide gage measurements of uplift along the south coast of Alaska. J. Geophys. Res. 96, 4325-4335.

Savage, J.C., Thatcher, W., 1992. Interseismic deformation at the Nankai Trough, Japan,

subduction zone. J. Geophys. Res. 97(B7), 11117–11135. doi:10.1029/92JB00810.

Sella, G.F., Dixon, T.H., Mao, A., 2002. REVEL: A model for recent plate velocities from space geodesy. J. Geophys. Res. 107(B4). doi:10.1029/2000JB000033.

Seno, T., 2005. Variation of downdip limit of the seismogenic zone near the Japanese islands: Implications for the serpentinization mechanism of the forearc mantle wedge. Earth Planet. Sci. Lett. 231, 249-262.

Shimazaki, K., Nakata, T., 1980. Time-predictable recurrence model for large earthquakes. Geophys. Res. Lett., 7, 279-282.

Scholz, C.H., 2002. The mechanics of earthquakes and faulting. Cambridge University Press, second edition, New York, 496.

Scholz, C.H., Campos, J., 2012. The seismic coupling of subduction zones revisited. J. Geophys. Res. 117, B05310. doi:10.1029/2011JB009003.

Shennan, I., 2009. Late Quaternary sea-level changes and palaeoseismology of the Bering Glacier region, Alaska. Quaternary Sci. Rev. 28, 1762-1773.

Shlien, S., 1972. Earthquake-tide correlation. Geophys. J. R. Astr. Soc. 28, 27-34.

Stern, R.J., 2002. Subduction zones. Rev. Gephys. 40(4), 1012. doi:10.1029/2001RG000108.

Swan, F.H., 1988. Temporal clustering of paleoseismic events on the Oued Fodda Fault, Algeria. Geology 16, 1092-1095.

Tajima, F., Mori, J., Kennett, B., 2012. A review of the 2011 Tohoku-Oki earthquake (M_w 9.0): Large-scale rupture across heterogeneous plate coupling. Tectonophysics 586, 15-34. doi:10.1016/j.tecto.2012.09.014.

Thatcher, W., 1984a. The earthquake deformation cycle at the Nankai Trough, southwst Japan. J. Geophys. Res. 89(B5), 2987-3101.

Thatcher, W., 1984b. The earthquake deformation cycle, recurrence, and the time-predictable model. J. Geophys. Res. 89(B7), 5674-5680.

Thatcher, W., Rundle, J.B., 1984. A viscoelastic coupling model for the cyclic deformation due to periodically repeated Earthquakes at subduction zones. J. Geophys. Res. 89(B9), 7631–7640. doi:10.1029/JB089iB09p07631.

Tsuruoka, H., Ohtake, M., Sato, H., 1995. Statistical test of the tidal triggering of earthquakes: contribution of the ocean tide loading effect. Geophys. J. Int. 122, 183-194.

Trubienko, O., Fleitout, L., Garaud, J.D., Vigny, C., 2013. Interpretation of interseismic deformations and the seismic cycle associated with large subduction earthquakes. Tectonophysics 589, 126-141.

Turcotte, D.L., Schubert, G., 2002. Geodynamics, 2nd ed, Cambridge University Press, New York, USA, 456 pp.

Vail, P.R., Mitchum, R.M. Thompson, S., 1977. Seismic stratigraphy and global changes of sea-level, Part 4: Global cycles of relative changes of sea-level. AAPG Memoir 26, 83-97.

Vigny, C., Socquet, A., Peyrat, S., Ruegg, J.C., Métois, M.., Madariaga, R., Morvan, S., Lancieri, M., Lacassin, R., Campos, J., Carrizo, D., Bejar-Pizarro, M., Barrientos, S., Armijo, R., Aranda, C., Valderas-Bermejo, M.C., Ortega, I., Bondoux, F., Baize, S., Lyon-Caen, H., Pavez, A., Vilotte, J. P., Bevis, M., Brooks, B., Smalley, R., Parra, H., Baez, J.C., Blanco, M., Cimbaro, S., Kendrick, E., 2011. The 2010 M_w 8.8 Maule mega-thrust earthquake of Central Chile, monitored by GPS. Science 332, 1417–1421.

REFERENCES

Völker, D., Wiedicke, M., Ladage, S., Gaedicke, C., Reichert, C., Rauch, K., Kramer, W., Heubeck, C., 2006. Latitudinal variations in sedimentary processes in the Peru-Chile trench off Central Chile. In: Oncken, G.C.O., Franz, G., Giese, P., Götze, H.J., Ramos, V.A., Strecker, M.R., Wigger, P. (Eds.), The Andes—Active Subduction Orogeny, Springer-Verlag, pp. 193-216.

Wallace, L.M, Fagereng, A., Ellis, S., 2012. Upper plate tectonic stress state may influence interseismic coupling on subduction megathrusts. Geology 40(10), 895-898.

Wang, K.L., He, J.H., 1999. Mechanics of low-stress forearcs: Nankai and Cascadia. J. Geophys. Res. 104(B7), 15191-15205.

Wang, K.L., Hu, Y., 2006. Accretionary prisms in subduction earthquake cycles: The theory of dynamic Coulomb wedge. J. Geophys. Res. 111, B06410.

Wang, K.L., Hu, Y., He, J., 2012. Deformation cycles of subduction earthquakes in a viscoelastic Earth. Nature 484(7394), 327-332.

Wang, K.L., Hyndman, R.D., Yamano, M., 1995. Thermal regime of the Southwest Japan subduction zone: effects of age history of the subducting plate. Tectonophysics 248(1-2), 53-69.

Wang, Z., Huang, W.L., Zhao, D.P., Pei, S.P., 2012. Mapping the Tohoku forearc: Implications for the mechanism of the 2011 East Japan earthquake (Mw 9.0). Tectonophysics 524, 147-154.

Wells, D.L., Coppersmith, K.J., 1994. New empirical relationships among magnitude, rupture length, rupture width, rupture Area, and surface displacement. B. Seismol. Soc. Am. 84(4), 974-1002.

Willett, S.D., 1999. Orogeny and orography: The effects of erosion on the structure of mountain belts. J. Geophys. Res. 104(B12), 28957-28981.doi:10.1029/1999JB900248.

Zachos, J., Pagani, M., Sloan, L., Thomas, E., Billups, K., 2011. Trends, rhythms, and aberrations in global climate 65 Ma to present. Science 292, 686-693.

Zhao, D., Huang, Z., Umino, N., Hasegawa, A., Kanamori, H., 2011. Structural heterogeneity in the megathrust zone and mechanism of the 2011 Tohoku-Oki earthquake (M_w 9.0). Geophys. Res. Lett. 38, L17308.

Zhao, S.R., Takemoto, S., 2000. Deformation and stress change associated with plate interaction at subduction zones: a kinematic modelling. Geophys. J. Int. 142(2), 300-318.

Lebenslauf

01.09.1989 – 01.07.1998	Absolvierung der Grundschulausbildung mit verschiedenen Stufen in Shenzhen (Guangdong, V.R. China)
01.09.1998 – 01.07.2001	Absolvierung des zehnten bis zwölften Schuljahres einschließlich Abitur im Juli 2001 in Shenzhen
01.09.2001 – 01.09.2003	Studium des Umweltingenieurwesens am Beijing Institute of Technology, Peking, V.R. China
01.10.2003 – 30.09.2004	Zwei Austauschsemester in Deutschland. Studium im Bachelor-Programm „Environmental and Resource Management (ERM)" an der Brandenburgischen Technischen Universität Cottbus (BTU-Cottbus)
01.10.2004 – 01.09.2006	weiteres Studim bis zum Abschluss mit Bachelor of Science (B.Sc.) an BTU-Cottbus
01.10.2006 – 30.09.2008	Studium im Master-Programm „Applied Environmental Geosciences (AEG)" mit Abschluss Master of Science (M.Sc.) an der Eberhard-Karls Universität Tübingen.
01.11.2008 – 30.07.2010	Wissenschaftliche Hilfskraft und wissenschaftlicher Mitarbeiter am Zentrum für angewandte Geowissenschaften (ZAG) der Universität Tübingen
01.08.2010 – 31.07.2013	Wissenschaftlicher Mitarbeiter und Doktorand am Institut für Geologie der Leibniz-Universität Hannover